Correlating Microstructure and Optoelectronic Performance of Carbon-Based Nanomaterials

By

Caitlin Rochford

Submitted to the graduate degree program in Department of Physics and Astronomy and the Graduate Faculty of the University of Kansas in partial fulfillment of the requirements for the degree of Doctor of Philosophy.

_____

Dr. Judy Wu, Chairperson

_____

Dr. Hsin-Ying Chiu

_____

Dr. Siyuan Han

_____

Dr. Hui Zhao

_____

Dr. Cindy Berrie

Date Defended: June 8, 2012

The Dissertation Committee for Caitlin Rochford
certifies that this is the approved version of the following dissertation:

Correlating Microstructure and Optoelectronic Performance of Carbon-Based Nanomaterials

_____
Dr. Judy Wu, Chairperson

Date approved: June 8, 2012

Abstract

There is a great deal of interest in carbon nanostructures such as graphene and various forms of carbon nanotubes due to their exceptional physical, electronic, and optical properties. Many technological applications have been proposed for these nanostructures, but despite the promise many carbon nanostructure-based optoelectronic devices fail to compete with their conventional counterparts. This is often due in large part to a non-optimized material or device microstructure. Factors such as crystallinity, contact quality, defect structure, and device configuration can critically affect device performance due to the high sensitivity and extreme surface to volume ratio of carbon nanostructures. In order for the exceptional intrinsic properties of the nanostructures to be exploited, a clear understanding of the microstructure and its correlation with device-relevant optoelectronic properties is needed. This dissertation presents four projects which demonstrate this principle. First, a TiO_2-coated carbon nanofiber is studied in order to optimize its structure for use in a novel dye-sensitized solar cell. Second, the electrode configuration of an individual multiwall carbon nanotube infrared sensor is investigated in order to surpass the limitations of disordered nanotube film-based infrared sensors. Third, the properties of defect structures in large area transferred graphene films grown by chemical vapor deposition are correlated with carrier diffusion in order to understand the film's low mobility compared to exfoliated graphene. Fourth, the effect of deposition conditions on graphene-metal contact was studied with the goal of achieving sufficiently transparent contacts for investigation of the superconducting proximity effect. All four projects highlight the unique properties of carbon nanostructures as well as the need to correlate their optoelectronic properties with microstructural details in order to achieve the desired device performance.

Dedicated to Russell Bryant Friedman

“There is no end to education. It is not that you read a book, pass an examination, and finish with education. The whole of life, from the moment you are born to the moment you die, is a process of learning.”

Jiddu Krishnamurti

Acknowledgements

Over the past five years at the University of Kansas I have been fortunate to have the support of many faculty, staff, and fellow students. This is truly a supportive and collaborative environment, and I had a great time here. First and foremost, I must thank my advisor, Professor Judy Wu, who taught me so much about how to be a scientist. No matter how busy she was, she always made time to discuss both research and life with me, give me sound advice, and provide me with whatever support I needed. Her work ethic and dedication to the success of her students are amazing. I would also like to thank Professor Hsin-Ying Chiu, who breathed new life into my projects and was extremely generous with her time and resources. Her current and future students are very lucky.

In addition to Judy and Hsin-Ying, I had the great pleasure of working with many people on a lot of different projects, and I would like to thank all of them for their expertise and support, especially Professor Siyuan Han, Dr. Rongtao Lu, and Dr. Bo Mao on the graphene-Nb project; Professor Hui Zhao and Nardeep Kumar on the CVD graphene defect and diffusion project; and Dr. Zhuang-Zhi Li, Dr. Javier Baca, Dr. Jianwei Liu, and Professor Jun Li on the TiO_2/CNF nanowire project. In addition to the scientists mentioned for these projects, I would like to thank many other people for their training, experimental support, or helpful discussions, especially Professor Cindy Berrie, Professor Ron Hui, Guowei Xu, Gary Malek, Alan Elliot, Dr. Brian Ruzicka, Dr. Lalani Werake, Caleb Christianson, Dr. Hui-Chun Chien, Dr. Rose Emergo, Dr. Jonathan Dizon, and Dr. Xiang Wang.

I would also like to thank the current and former staff members of the Department of Physics and Astronomy who keep the department running, especially Tess Gratton, Teri Leahy,

Doug Fay, Kim Hubbel, Don Nieto, and John Clune. A special thanks goes out to Jeff Worth, the person we go to for anything and everything instrument related, and Allen Hase, Zach Kessler, and Steve Davies of the Physics Machine Shop, who can build just about anything.

I am not sure who in particular to thank for this, but I want to express an appreciation for the opportunity to teach several Duke T.I.P. physics courses for middle and high school kids and more recently a Nanotechnology course for senior citizens at the Osher Lifelong Learning Institute. There are few things more rewarding than teaching people who show up voluntarily with nothing to gain but knowledge. As scientists I believe we have a great responsibility to reach out to non-scientists of all ages. I was delighted to be able to do that through these classes, and I was surprised by how much fun I had.

Finally, I owe a great deal of thanks to my friends and family who helped me through a lot of difficult times over the past several years. It would be impossible to say everything I want to say in this short preface, so I will just say that I am incredibly lucky to have the love and support of so many wonderful people. I would, however, especially like to thank my Dad, who has never been one to give much advice but has taught me so much by example.

Contents

List of Figures

Chapter 1

Introduction

1.1 Introduction to Carbon Nanomaterials

Carbon, the sixth element of the periodic table, forms the basis of all known life on earth. Despite its familiarity and ubiquity however, carbon truly is a wonder. In the form of a diamond, carbon disperses light, conducts electricity very poorly, and has the highest hardness and thermal conductivity of any naturally occurring bulk material on earth. In the form of graphite, carbon is black, conducts electricity very well, and is extremely soft. Whether carbon is best suited for industrial drilling applications or for use in a writing utensil depends on the arrangement of the atoms.

A neutral carbon atom has six protons balanced by six electrons in the configuration $1s^2 2s^2 2p^2$. Because the s-orbital and p-orbitals of carbon's second electronic shell have very similar energies, they can hybridize to form bonds with different geometries. In a diamond, each carbon atom forms four covalent bonds in a sp^3 hybridized tetrahedral orbital. All of the p-orbitals are used for bonding so there are no free electrons and the resistivity, typically on the order of 100 GΩ·m, is very high. The crystal structure of diamond is face-centered cubic, which is very stable and rigid. This leads to the high hardness and melting point. These strong covalent bonds also give diamond its high thermal conductivity at room temperature, about 2200 W/m·K, which is roughly five times higher than copper. Graphite on the other hand consists of many stacked sheets of hexagonally arranged carbon atoms. Each atom forms three covalent bonds in a sp^2 hybridized planar orbital. The unhybridized p-orbital is oriented perpendicularly to the

hybridized orbital's plane. This orbital overlaps with those of neighboring carbon atoms and allows for good electrical conduction along the individual sheets. The resistivity is typically reported in on the order of a few to a few tens of μΩ·m, up to 17 orders of magnitude lower than diamond! Only weak Van der Waals forces exist between the carbon sheets, leading to its soft and lubricating nature[1].

The emergence of nanoscience in the past few decades has shown us even more tricks that carbon can play. New zero- and one-dimensional carbon allotropes were discovered throughout the 1980's and 1990's. The first was the Buckminsterfullerene, a hollow sphere consisting of 60 carbon atoms resembling a soccer ball, which discovered in 1985 by Richard Smalley and coworkers[2]. This work sparked intense research into the possibility of other carbon-based nanostructures. In 1991, Iijima was the first to report carbon nanotubes, coaxial tubes of graphitic sheets in which the carbon atom hexagons trace a helical path around the tube axis[3]. Interestingly, carbon nanotubes can be either semiconducting or metallic depending on their chirality, and in the semiconducting case the size of the bandgap depends on the tube diameter. Chirality is the "twist" in the nanotube, and is represented by a vector which connects two equivalent sites on an unrolled nanotube sheet. Among carbon nanotubes' remarkable properties is an ultrahigh room temperature thermal conductivity of about 3500 W/m·K along the axis of single wall carbon nanotubes[4], which is even higher than natural diamonds. This is juxtaposed to a relatively poor thermal conductivity of just a few W/m·K in the radial direction[5]. Carbon nanotubes also have the highest tensile strength and Young's modulus of any known material, given by a reported 63 GPa for a multiwall carbon nanotube[6] and about ~ 1 – 4 TPa in the axial direction of nanotubes with varying diameters[7], respectively. Following these groundbreaking discoveries, many forms of carbon based spheres and tubes were later reported and have since

been the subject of intense research because of their unique properties and possibilities for technological applications.

In 2004, carbon surprised us yet again in the experimental discovery of graphene, a one atom thick sheet of sp^2-bonded carbon atoms arranged in a hexagonal crystal lattice[8]. These sheets are in fact the building blocks of other graphitic structures. They can be wrapped into a sphere to form Bucky balls, rolled up to form carbon nanotubes, or stacked by the millions to form graphite. Graphene boasts many exceptional and incomparable properties which will be discussed in more detail in later chapters. To give the reader a flavor of these properties, consider the following. It is the thinnest (one atomic sheet) and strongest (~ 130 GPa ultimate strength[9]) known material on earth, it is able to sustain current densities (~ 10^8 A/cm^2 for few layer graphene nanoribbons[10]) six orders of magnitude higher than copper, it has zero effective mass charge carriers with huge mobilities (up to 2×10^5 cm^2/V·s[11]) , it is impermeable to gases[12], and more. After many failed chemical attempts, the isolation of an individual layer of graphene for the first time was achieved by an incredibly simple technique of repeated peeling of graphite using Scotch tape[8]. The excitement surrounding graphene within the scientific community was recently echoed by the 2010 Nobel Prize in Physics which was awarded to Andre Geim and Konstantin Novoselov "for groundbreaking experiments regarding the two-dimensional material graphene"[13].

Both graphene and many forms of carbon nanotubes, including as grown and functionalized single wall nanotubes, multiwall nanotubes, and carbon nanofibers, are being explored in myriad optical and electronic applications, some of which will be mentioned here. One of the most important features of carbon nanotubes for electronic applications is their quasi-one dimensional geometry. Because electrical and thermal transport is much more efficient

axially than radially, carbon nanotubes are often used in devices to provide directional charge or thermal transport. One major area of research utilizing this effect is in solar cells[14,15] in which the carbon nanotube provides a direct route for electrons to the anode. Additionally, due to their potentially high aspect and surface to volume ratios, carbon nanotubes are being studied as highly sensitive gas[16] and infrared sensors[17]. Graphene is considered to be an extremely attractive alternative for transparent conductors in a variety of devices because of its flexibility, optical transparency, and low sheet resistance. The biggest issue at hand is how to create high quality large scale graphene films which can be patterned lithographically or utilized in large area applications such as touch screens. As will be discussed later in this document, large area graphene suffers from a variety of structural defects which degrade its electronic performance. An understanding of the effect of these defects on graphene's electronic properties and improved growth and device fabrication techniques are keenly needed. Primarily because of its high mobility, graphene is also being considered as the active element in many electronic devices such as ultrafast photodetectors[18], high frequency transistors[19], single electron transistors[20], or as a qubit for quantum technologies[20,21]. Because graphene's electronic device performance is so sensitive to the fabrication procedures and device structure, one of the biggest challenges with these types of devices is to avoid destroying or masking graphene's intrinsic properties through inappropriate device structure or non-optimized fabrication.

This dissertation contains work regarding four different carbon nanostructures: carbon nanofibers coated with titanium dioxide, multiwall carbon nanotubes, graphene grown by chemical vapor deposition, and micromechanically exfoliated graphene flakes. Each of the carbon nanostructures studied in this body of work will be introduced in further detail in the following chapters. The breadth and depth of research conducted by the physics, chemistry, and

materials science communities on these materials is huge, and so the introduction to each material will focus only on the most relevant properties.

1.2 Importance of Studying Microstructure in Nanoscience

Based purely on the construction of the word, the term *microstructure* refers to the small characteristics of an object which is built out of other things. More quantitatively, one might suggest that it refers to an object's structure on the 10^{-6} meter scale, or as viewed under an optical microscope above a certain magnification. In this dissertation we will take *microstructure* to refer generally to the details of the construction of a material or device relevant to nanoscience. That is, for example, how the atoms or grains are arranged, the nature of the surfaces and interfaces, how the material interacts with the environment, the presence of defect structures, and the geometry of a nanoscale device, to name a few. Nanoscience cannot be done, or at least cannot be done well, without an understanding of microstructure and an appreciation for its effect on experimental outcomes and device performance.

The biggest reason for this is the scale of the materials and devices in question. As objects get smaller and smaller their surfaces become more and more important. In some cases, such as monolayer graphene and single wall carbon nanotubes, the material may consist entirely of surface and no "insides". The nature of the surface and how it interacts with gases in the environment, the substrate, and materials it is in contact with may then dominate the behavior of that material. If the microstructure is not well understood, experiments are very difficult to interpret, and desired effects may be elusive.

Additionally, important processes for material and device physics such as charge transport, metal contact, and photon absorption are extremely sensitive to microstructure. This is

especially relevant for devices made of arrays or composites of nanostructures. Often times complex macroscopic devices such as solar cells, thermoelectric arrays, or detectors are constructed out of as grown nanostructures without careful characterization of the constituent parts. When the device performance is inevitably poorer than hoped it is difficult to know precisely why. The key to overcoming this hurdle is to correlate the microstructure with the optical and electronic properties relevant to device performance and use that information to optimize material growth, device fabrication, and experimental conditions. This encompasses the theme of this dissertation, which will be elaborated on in the following section.

1.3 Overview and Theme of Following Chapters

As evidenced by the previous section, nanoscale sample fabrication involves a substantial learning curve. Additionally, the fabrication is not entirely transferrable to different materials. Over the years I fabricated nano- and microscale devices on various inorganic nanowires, carbon nanotubes, and graphene. Each material has its own set of considerations, and the fabrication must be optimized according to that material's and device's demands. For example, something as simple as how to deposit niobium metal onto graphene has taken many months to optimize.

Because of the nature of nano- and microscale device research, a great deal of time must be spent on device fabrication. Through this journey I developed an appreciation for the importance of the microstructure of a device, including that of the material itself; the nature of its interfaces with the substrate, metal, and environment; and the details of the fabrication procedure. All of these things can have tremendous effects on what is measured in an experiment. Without careful control and consideration of these factors and more, meaningful results are difficult to obtain, and device optimization is hindered. I believe that this mindset is

the most important thing that I take with me as I move forward in my research career. It is also the theme of this dissertation.

During my time at the University of Kansas, I was able to work on many different projects, four of which are presented here. The second chapter discusses studies on individual titanium dioxide coated carbon nanofibers (CNFs). These core-shell nanowires were grown by collaborators at Kansas State University for use in a novel dye-sensitized solar cell architecture. Despite the many expected advantages of this novel design, the power conversion efficiency of the solar cell was only 1.09%, significantly lower than the >10% efficiencies of the design it set out to replace. The goal of the individual nanowire work was to extract a single nanowire from the solar cell, study its properties, determine the reason for the low efficiency, and develop a way to improve it. Through this work, the role of the microstructure on device performance was elucidated, and a method to greatly improve the efficiency was presented.

The third chapter deals with an individual multiwall carbon nanotube infrared sensor. This work was a follow up to a series of papers by Dr. Rongtao Lu and coworkers on the topic of single wall and multiwall carbon nanotube film infrared detectors. Through that work it was determined intertube junctions were a major limiting factor for sensor performance. This motivated work on an individual nanotube sensor, which completely eliminates intertube junctions. By paying careful attention to the electrode configuration and the nature of the contact, a responsivity two orders of magnitude higher than the best previously reported on carbon nanotube infrared detectors was achieved.

The fourth chapter discusses a very recent work done in collaboration with Nardeep Sharma and Professor Hui Zhao at University of Kansas on graphene grown by chemical vapor deposition. Many technological applications have been proposed for graphene because of its

exceptional electronic and optical properties, which are typically measured on single crystal graphene flakes. Large area films suitable for lithographic patterning, however, are desired if graphene is to be used commercially. While a variety of techniques to grow these films exists, the resulting graphene film quality is much lower than the exfoliated flakes due to grain boundaries, wrinkles formed during growth, and large defects due to the process of transferring the film to the desired substrate. By characterizing the film defect structures with Raman spectroscopy and correlating it with optical measurements of carrier diffusion, the relationship between the microstructure of the film and its carrier dynamics can be studied. This is important in order to understand the mechanisms behind the poor electronic quality of large area graphene.

The fifth chapter is unique. It reviews work done over the past year and a half which in a sense is just getting started. We initially set out to study the superconducting proximity effect in graphene flakes with niobium electrodes. In addition to equipment challenges and unforeseen delays, we found that deposition of the metal on graphene for this experiment was not straightforward. The required fast, high energy sputtering deposition of niobium was found to cause damage to graphene, leading to a huge contact resistance. Before the intended experiment could be completed, the graphene-metal junction needed to be optimized. Without ensuring good quality, highly transparent contact the superconducting proximity effect will certainly be diminished if not destroyed. This chapter contains the work done toward this end.

Chapter 2

Individual TiO_2/Carbon Nanofiber Core-Shell Nanowire Studies for Dye-Sensitized Solar Cell Applications

2.1 Introduction to Photovoltaics and the Dye-Sensitized Solar Cell

Between the years 2000 and 2050, the world energy demand is expected to double from 14 terawatts (TW) to 28 TW, due mainly to an increase in population concentrated in the developing world[22]. Since access to a stable energy supply has been observed to couple to quality of life, economic prosperity, and global stability, finding sustainable energy sources to meet this demand is an area of utmost interest. Sustainable energy sources are those which meet present needs without compromising the ability of future generation to meet their own needs, to borrow from an often used definition of sustainability. By this definition, it can be inferred that the desired energy sources must be ones which will not be depleted on a time scale which is relevant for humans. Fossil fuels, which currently provide the vast majority of humans' energy, do not meet the above criterion due to their insufficient reserves and the deleterious effects of their use such as pollution which is harmful to human health and greenhouse gases which contribute to climate change. Candidates for a sustainable energy source include but are not limited to sunlight, wind, tides, and heat stored in the earth. Of these, sunlight is arguably the most powerful.

The earth itself is an excellent example of how sunlight can be used as an energy source. The surface of the earth receives approximately 120,000 TW of energy from the sun. The earth uses this energy to drive circulation of wind and ocean currents, water evaporation and condensation

cycles which create fresh water reserves in the form of rivers and lakes, and photosynthesis which sustains the plant life that produces oxygen and feeds both humans and animals. In addition, humans have the technology to use solar energy to help power society in several ways including creating electricity through photovoltaic devices, growing biomass for fuel, and concentrating sunlight for the high temperature creation of fuels. Despite the fact that more energy from the sun strikes the earth in one hour than humans use in an entire year, the above methods only provide a small fraction of the total energy demand. Fuels from biomass are the primary energy source for over 10^9 humans, yet sustainable biomass only provides 1.5% of total energy consumed worldwide. Further, photovoltaics provide less than 0.1% of the world's electricity[22]. This disproportion presents a huge research challenge with technological needs including new materials that more efficiently absorb sunlight and a means to utilize the full solar spectrum. More generally speaking, the most important advances required for large scale utilization of solar energy are a decrease in cost per watt and an improvement in energy balance. That is, the technologies need to be able to create more energy for less money using less energy intensive starting materials and processes.

Research in photovoltaics is especially interesting for condensed matter physicists due to the potential contributions of advancements in thin film processes, nanoscience, and nanoscale characterization. Photovoltaic devices come in many forms, but in general all employ the photovoltaic effect, discovered by physicist Edmund Becquerel in 1839. As the name suggests, the photovoltaic effect involves the creation of a voltage when a material is exposed to light. When an electron in an inorganic semiconductor absorbs a photon with energy greater than or equal to the bandgap, it is promoted from its localized position in the valence band to the conduction band, where it is free to move around or be transferred to another material. This leaves a hole in the valence band. In a photovoltaic cell, or solar cell, there is a mechanism present such that the electrons and holes travel preferentially in opposite directions so that one

side of the cell acquires a negative bias with respect to the other. The specific materials and mechanism that separates the electrons and holes vary depending on the particular solar cell in question. Historically and physically solar cells can be grouped into three generations.

First generation solar cells are based on a single crystal inorganic semiconductor, namely silicon, which forms a p-n junction in a planar geometry. The p-n junction, which is critical to the operation of this solar cell, begins with an n-type material and a p-type material. N-type (p-type) materials are doped with donor (acceptor) impurities. For silicon, which has four valence electrons, the most common donor (acceptor) is phosphorus (boron) which has five (three) valence electrons. These dopants are shallow, meaning that the donor energy level is close to the conduction band minimum, and the acceptor energy level is close to the valence band maximum. This way the electron (hole) density in the n-type (p-type) semiconductor is approximately equal to the donor (acceptor) density due to thermal excitations. When the n-type and p-type regions are in contact, free electrons (holes) in the n-type (p-type) region are able to cross the junction into the p-type (n-type) region and recombine with the holes (electrons). This leaves the ionized donors (acceptors) behind so that the n-type (p-type) region obtains a net positive (negative) charge. This process also results in a region surrounding the interface that is free of mobile charges, called the depletion layer. The charge due to the ionized donors and acceptors creates an electric field across the depletion layer directed from n-type to p-type. Thermal equilibrium is reached when the drift current due to the electric field matches the diffusion current in the opposite direction. At this point the Fermi energy is constant throughout what is now a p-n diode. In order to use this structure in a solar cell, one only needs to add a front and back electrical contact. If photo-generated electrons or holes diffuse to the depletion layer before they recombine, the minority carrier will drift across the junction due to the built in electric field and

become a majority carrier. The electrons then travel through the n-type region and through the external load before recombining with holes in the p-type region, generating the current.

Before discussing other types of solar cells, it is advantageous to now introduce the solar cell figures of merit[23]. The terms from the following discussion will be used throughout the rest of the chapter. An ideal solar cell can most simply be modeled as a diode in parallel with a current source as seen here in Figure 2.1.

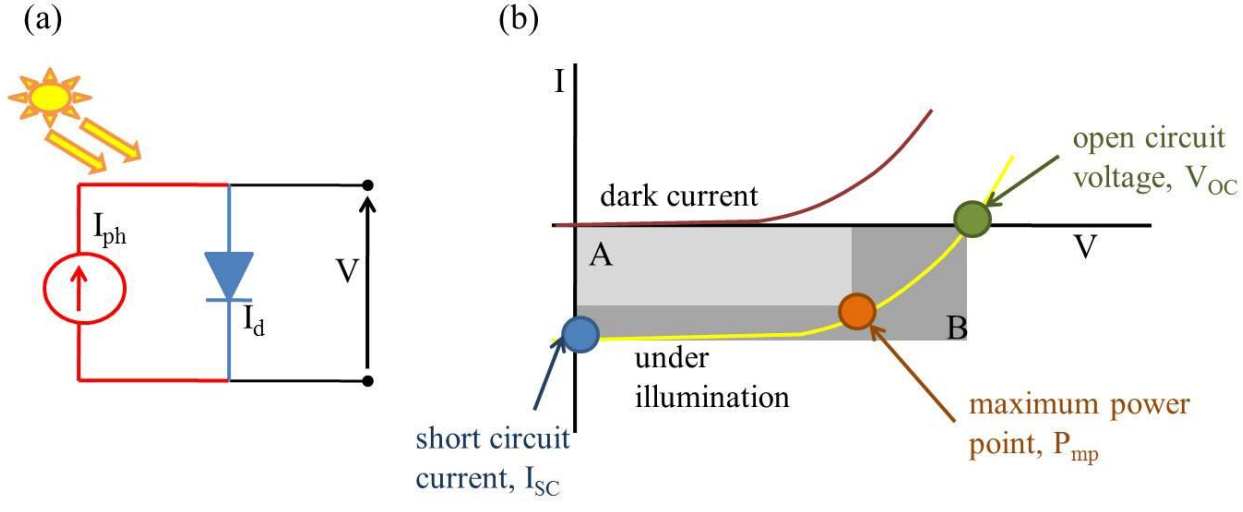

Figure 2.1: Left: Simple solar cell equivalent circuit diagram consisting of a diode in parallel with a current source. Right: typical solar cell I-V curve in dark and under illumination. Important figures of merit are marked.

The current is then given by

$$I = I_d - I_{ph} = I_0\left(e^{\frac{qV}{nk_BT}} - 1\right) - I_{ph} \tag{2.1}$$

where I_d is the diode current, I_{ph} is the current due to light generated carriers, I_0 is the diode saturation current, q is the electronic charge, V is the voltage, n is the ideality factor between 1 and 2, k_B is Boltzmann's constant, and T is the temperature. The ideality factor describes the recombination behavior of the cell and measures how closely the cell follows the ideal diode

equation. Ideally $n = 1$, which means that the cell is dominated by diffusion. Values of n closer to 2 mean that recombination is dominant. The saturation current, I_0, is the diode leakage current in the absence of light. Even though the built in field inhibits the diffusion of carriers across the junction, some majority carriers will still be able to cross the junction and become minority carriers. They then diffuse farther away from the junction, on average a distance equal to the minority carrier diffusion length, and recombine. In the absence of recombination, the minority carriers would continue to diffuse until a uniform concentration is reached, ending net diffusion. However, since the carriers do recombine, more carriers can diffuse across the junction. This means that the diffusion current is a recombination current. Therefore I_0 is a measure of recombination, and there is an effort to minimize this value.

When there is no light incident on the cell, it behaves like a diode, as shown by the red curve on the right in Figure 2.1. When light is incident on the cell, the I curve shifts downward. The current at zero bias is the short circuit current (I_{SC}). This is the maximum current that can be extracted from the cell. From Equation 2.1, setting $V = 0$ clearly gives $I_{SC} = - I_{ph}$. For a given incident spectrum and intensity, I_{SC} depends on the absorption of the material, the reflection at the surface, and the carrier collection probability, which depends chiefly on surface passivation and minority carrier diffusion length. The voltage which occurs at zero current is the open circuit voltage (V_{OC}). This is the maximum voltage available from the cell and is equivalent to the situation where the diode current and the photo-generated current exactly cancel out. This can be clearly seen by setting Equation 2.1 equal to zero and solving for V:

$$V_{OC} = \frac{nk_B T}{q} \ln\left(\frac{I_{ph}}{I_0} + 1\right). \tag{2.2}$$

Typically, V_{OC} is equal to the difference between the quasi Fermi levels of the minority carriers, i.e. the electrons in the p-type region and the holes in the n-type region. The term quasi Fermi level is used since the electron and hole populations have been displaced from equilibrium due to the incident light so that the electrons and holes are in thermal equilibrium with themselves but not with each other.

Since power $P = I \cdot V$, the power is zero at both short circuit and open circuit conditions, and in between exists a point of maximum power, labeled P_{mp}. The fill factor (*FF*) is defined as the ratio of P_{mp} to the product of V_{OC} and I_{SC}. In Figure 2.1, the *FF* is equal to the ratio of the areas of rectangles A and B and is a measure of the "squared-ness" of the *I-V* curve. This is primarily affected by the cell's series and shunt resistance, R_S and R_{SH}, which can be represented in the equivalent circuit diagram as shown in Figure 2.2.

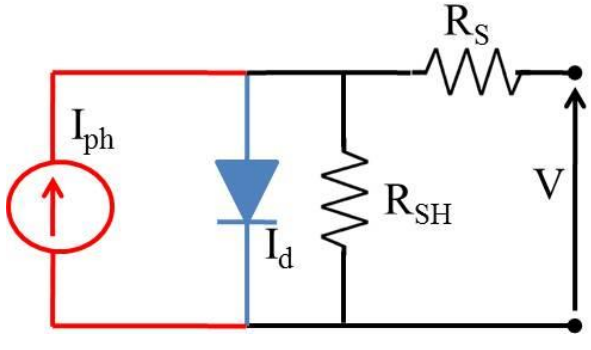

Figure 2.2: Equivalent circuit diagram for a solar cell including series and shunt resistances.

These parasitic resistances dissipate power from the solar cell. The series resistance is mainly caused by the current through the cell and the contact resistance to the electrodes. A low shunt resistance occurs when the light generated current finds an alternate current path. This is usually caused by fabrication defects. The solar cell's efficiency is defined as the ratio of the maximum power out from the cell to the incident power from the sun.

$$\eta = \frac{P_{mp}}{P_{in}} = \frac{FF \cdot V_{OC} \cdot I_{SC}}{E \cdot A_C} \tag{2.3}$$

Here E is the irradiance of the incident light in W/m^2, and A_c is the cell area. Efficiency is the most common and most recognizable figure of merit used to compare solar cells to each other. Silicon is attractive as a solar cell material for several reasons. It is abundant in the earth's crust (second only to oxygen), non-toxic, and is backed by years of experience in the electronics industry. Its detriments however, largely based on its material properties, have begun to outweigh its benefits in solar cell applications. Silicon is an indirect bandgap semiconductor. This means that the minimum of the conduction band and the maximum of the valence band correspond to different wave vectors, as opposed to a direct bandgap semiconductor in which they reside at the same wave vector, as shown in Figure 2.3.

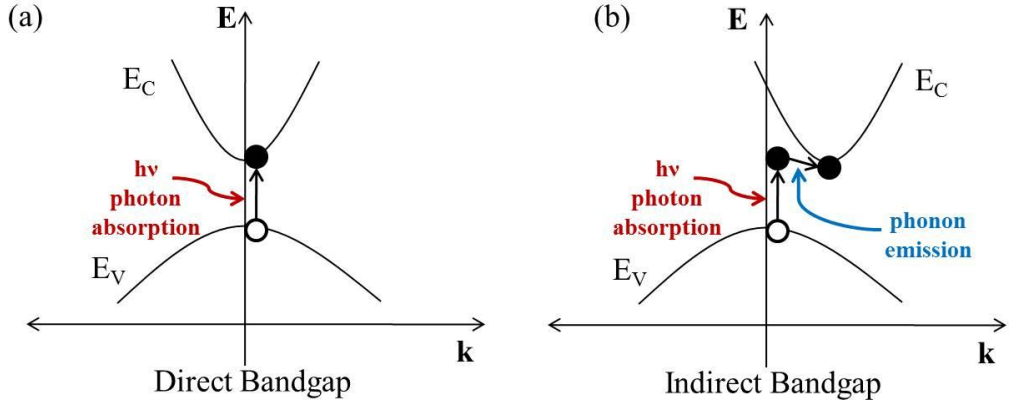

Figure 2.3: E-k diagram showing the difference between a (a) direct and (b) indirect transition upon photon absorption in a semiconductor.

Photons have very little momentum, with magnitude given by

$$p = \hbar k = \frac{h\nu}{c} = \frac{h}{\lambda} \tag{2.4}$$

where $\hbar = h/2\pi$, h is Planck's constant, v is velocity, c is the speed of light, and λ is wavelength. Because of this small momentum, they cause electrons to make a nearly vertical transition in the E-k diagram. In the case of a direct bandgap, shown on the left, an electron which absorbs a photon with energy greater than or equal to the bandgap is easily able to find a state in the conduction band with energy and momentum equal to that of the electron plus photon. In the case of an indirect bandgap, the electron requires the assistance of a phonon to conserve both energy and momentum, which has large momentum compared to its energy, in order to find an empty state in the conduction band while still conserving energy and momentum. In order for this to occur, the electron can either absorb both a photon and a phonon, or it can absorb a photon with slightly higher energy and emit a phonon. Since these processes involve an electron, photon, and phonon, the probability for occurrence will be lower than that involving just the electron and photon. This is the cause of silicon's low absorption coefficient.

The absorption coefficient, α, which varies with wavelength for a given material, determines how much light the material will absorb. The inverse, α^{-1}, is the average distance a photon will travel through a material before being absorbed. In equation form, this looks like

$$I(z) = I(0)e^{-\alpha z} \tag{2.5}$$

where *I(z)* is the light intensity, z is the distance into the material, *I(0)* is the intensity at $z = 0$, and the absorption coefficient α depends on the photon energy. Therefore solar cells made from materials with a low absorption coefficient will require a greater thickness than those with a high absorption coefficient. A thicker absorber layer translates to a lower acceptable density of defects and impurities in the crystal, which act as recombination centers via Shockley-Read-Hall recombination (SRH)[24], which is thought to dominate bulk recombination in solar cells. SRH is a non-radiative process which takes place at a localized trap within the bandgap. An electron

(hole) is captured by the trap and then recombines with a hole (electron) in the valence band (conduction band) in a second step. The energy is released via phonon emission instead of photon emission, hence the description "nonradiative". The traps may be created by deep level impurities or defects such as vacancies, interstitials, dislocations, grain boundaries, or anti-site defects. With a higher trap density come lower minority carrier lifetime and diffusion length. Since minority carriers must diffuse to the depletion layer before they can be swept across the junction, the thickness should be selected such that no site in the semiconductor is farther than a minority carrier diffusion length away from the depletion layer. In order for this thickness requirement to be reconciled with that for maximum photon absorption, the level of impurities and defect density must be very low so that recombination does not severely limit the collected current. The required thickness for absorption also exacerbates the problem of the high cost of 1st generation solar cells due to high vacuum and high temperature processing and low tolerance for impurities and defects.

In the early days of solar cell development the primary application was space and satellite use, so high cost was not a dominant concern. After the oil embargo in 1973, people became more concerned with energy supply and renewable energy, leading to the birth of the Department of Energy. Soon the terrestrial photovoltaics industry began benefiting from increased interest and funding with the hope of decreasing the cost per watt ratio. First generation solar cells, however, suffer from not only a high lower limit on cost but also a low upper limit on efficiency. The maximum energy conversion efficiency of a single p-n junction solar cell under solar illumination was determined to be 31% by what is known as the Shockley-Queisser Limit[25], so named after a paper published in 1961 by Shockley and Queisser. In order to decrease the cost per watt, new solar cells had to be developed that decreased the cost or increased the efficiency

over first generation solar cells, which generally represent the goals of the second and third generations of solar cells, respectively.

Third generation solar cells attempt to improve the efficiency above the Shockley-Queisser Limit by circumventing some of the assumptions in the calculation[26]. Examples include increasing the number of p-n junctions by employing a stacked geometry in which solar cells with different bandgaps form a tandem device, obtaining more than one electron-hole pair per photon via impact ionization, and transforming the solar spectrum to one with the same total energy but a smaller wavelength range with up or down converters. With the exception of tandem solar cells, none of these ideas have met much success. While the third generation solar cells involve very interesting physics, they are outside of the scope of this work.

Second generation solar cells attempt to maintain an acceptable efficiency while drastically lowering the cost. These solar cells go beyond inorganic single crystalline semiconductors, introducing both new advantages and new difficulties which need to be addressed. Second generation solar cells are often referred to as thin film solar cells. They are allowed to be much thinner due to greater absorption coefficients and can be fabricated by growing layers on a large substrate instead of cutting a wafer from a crystal. The reduced material quantity and ease of fabrication both help reduce cost. Second generation solar cells can generally be grouped into four categories: inorganic, organic, hybrid, and photoelectrochemical cells. As will be shown below, the photoelectrochemical cell, specifically the dye-sensitized solar cell (DSSC), is especially promising and does not suffer from the same detrimental drawbacks of the other three categories.

Many traditional thin film solar cells are made of inorganic semiconductors with planar p-n junction geometry similar to 1st generation solar cells. These can be one semiconductor

doped both n-type and p-type to form a homojunction or they can be two semiconductors that form a heterojunction. The latter offers a greater degree of flexibility compared to the former since there is no restriction to materials that can be doped both n-type and p-type, and two different bandgaps can be used to harvest more of the solar spectrum more efficiently. Despite these advances, thin film inorganic solar cells have limits since historically it is expected that technology will eventually advance to a point where the cost is once again dominated by the starting materials as was the case of 1st generation solar cells. Further, since these types of solar cells are typically deposited at relatively low temperatures, the resulting small grains introduce significant recombination at grain boundaries. Organic semiconductors offer an attractive alternative on both fronts due to the drastic decrease in cost and lack of dangling bonds at surfaces.

Organic semiconductors are different from inorganic semiconductors in many ways[27]. Instead of covalent bonds and band transport, organic semiconductors rely on Van der Waals interactions and hopping between localized states. Instead of a valence and conduction band, they have a lowest unoccupied molecular orbital (LUMO) and a highest occupied molecular orbital (HOMO). Instead of a p-n junction, there is an electron donor and acceptor interface. When an organic semiconductor absorbs a photon, it generates an exciton. This mobile, bound electron-hole pair must then diffuse to a heterojunction in order to dissociate and be separated by an offset in ionization potential or electron affinity that is greater than the exciton binding energy (typically a few 10^2 meV). A staggered band alignment, or type II alignment, ensures that one material transports the electrons and one transports the holes. These principles are illustrated in Figure 2.4.

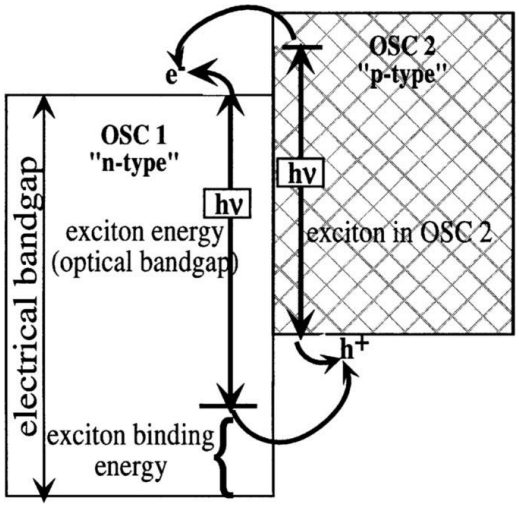

Figure 2.4: Energy level diagram for an excitonic solar cell in which the two organic semiconductors have a staggered gap alignment or type II heterojunction.

Benefits of organic semiconductors include a high absorption coefficient requiring only a few 10^2 nm thickness, low cost synthesis, room temperature solution processing, and functionality that can be controlled by chemical synthesis. However, the electron and hole mobilities are several orders of magnitude lower than inorganic semiconductors, and exciton diffusion lengths are around 10-15nm, which means that no site in the active layer should be more than 10-15nm away from a heterojunction. For this reason, a bulk heterojunction design is employed such that the junction is distributed throughout the entire volume by mixing together the two semiconductors to form a blended active layer, and the electric field providing directionality is supplied by electrodes with offset work functions. The required degree of nanoscale control is extremely difficult to achieve and often incomplete pathways or insufficient mixing occurs. This combined with the low mobilities leads to a low short circuit current and efficiency. In order to combine the advantages of both inorganic and organic semiconductors, namely high mobilities and low temperature solution processing, hybrid solar cells arose, gaining a lot of attention with the seminal 2002 paper by Huynh *et al*[28].

Hybrid solar cells employ an inorganic semiconductor for electron transport and a conductive polymer for hole transport with a type II band alignment in a bulk heterojunction design. By far, the most common hole conductor in hybrid solar cells is regioregular P3HT (poly(3-hexylthiophene). Regioregularity refers to the head to tail linking of the monomers. The polymer owes its conductivity to its conjugated backbone in which the atoms are covalently bonded with alternating single and multiple bonds resulting in electron delocalization due to the overlap of adjacent π-orbitals. P3HT is especially popular for organic and hybrid solar cells because it has a high absorption coefficient that is reasonably matched with the solar spectrum. As with organic solar cells, exciton dissociation and charge separation is favored by type II band alignment between the polymer and the inorganic semiconductor. High aspect ratio crystalline nanostructures such as nanowires, nanorods, or nanotubes are typically used in order to provide a directional path for electron transport. In the most promising devices, the inorganic nanostructures are grown on an electrode in a vertically aligned array so that the electrons have a direct, complete collection pathway. Since excitons would then diffuse radially to reach a heterojunction instead of vertically, the thickness of the active layer can be chosen for optimal absorption without negatively affecting the carrier collection efficiency and short circuit current. Further, both the polymer and nanostructure can serve as photon absorbers, and the bandgap of the nanostructure can be chosen so that the two have a complementary absorption spectrum. While the ease of fabrication and flexibility of design of hybrid solar cells is highly desirable, the polymer (hole transport material) tends to be the limiting factor. P3HT is semi-crystalline at room temperature, and annealing creates crystalline "nanodomains" where the polymer has self-organized into 2D sheets, improving the conductivity[29]. However, inclusion of electron acceptors such as nanowires or nanorods in the polymer matrix either disrupts the order and decreases the

conductivity or causes the distance between heterojunction sites to be longer than the exciton diffusion length. Comparing the above types of thin film solar cells, it seems that one simply trades one disadvantage for another, creating a new problem with every problem solved.

The final type of 2nd generation solar cell to be discussed is the dye-sensitized solar cell (DSSC). This photoelectrochemical cell employs quite different principles of operation, and in doing so avoids nearly all of the problems mentioned above. The DSSC was first reported by Grätzel and O'Reagan in 1991 to have an efficiency of 7.1%[30]. Since then it has been pushed to over 12%[31], making it fully competitive with existing commercial amorphous silicon thin film solar cells. DSSC operation is shown schematically in Figure 2.5(a).

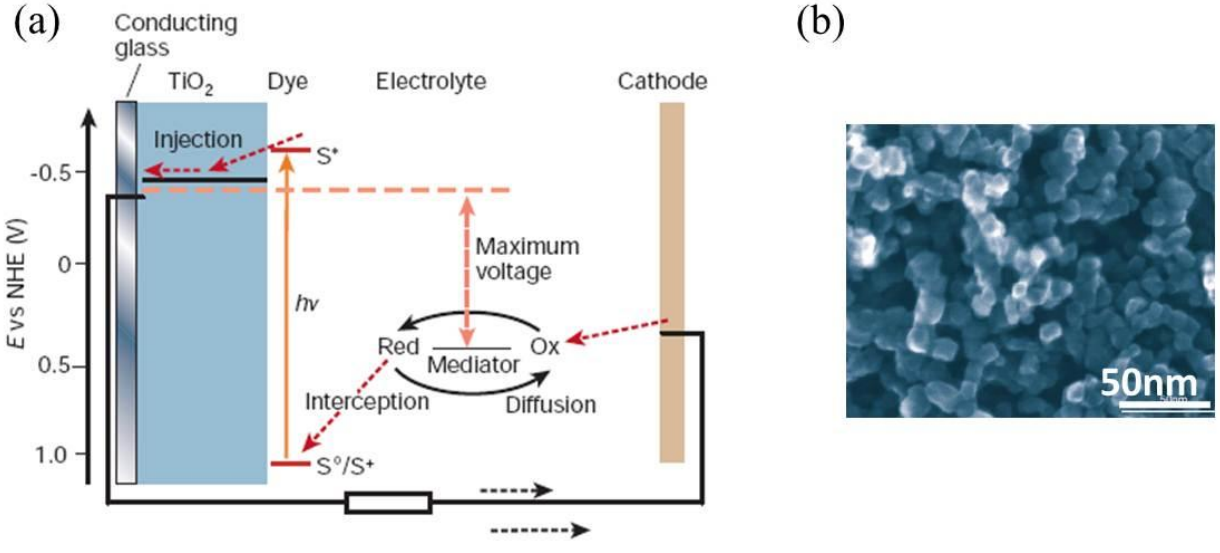

Figure 2.5: (a) Schematic of dye-sensitized solar cell operation and (b) scanning electron micrograph of the TiO_2 nanoparticle network. Both images are from reference [32]

Light is absorbed by a dye which is adsorbed as a monolayer onto the surface of an undoped mesoporous TiO_2 film consisting of nanometer scale particles which have been sintered together in order to permit conduction. The photoexcited electron is injected from the dye into the TiO_2 film and transported to the anode. The original state of the dye is regenerated by oxidation of the

electrolyte which typically consists of the redox couple iodide/triiodide. The iodide is in turn regenerated by reduction of triiodide at the cathode by electrons which have circulated through the external load, completing the circuit. In contrast with conventional solar cells, here each material performs one specific task. Most importantly, the functions of light absorption and charge carrier transport are completely decoupled. Further, the DSSC is a majority carrier device. Since there are no minority carriers, surface and bulk recombination due to defects is minimized.

The earliest attempts at dye-sensitized solar cells produced efficiencies <1%, primarily due to the fact that a monolayer of dye on a smooth surface is only capable of absorbing a tiny fraction of the incident light. Sintering together TiO_2 nanoparticles (NPs) several nanometers in diameter to form a ~10 μm thick film with ~50% porosity, as seen in Figure 2.5 (b), produces a surface area for dye adsorption over 10^3 times larger than a flat surface. Further, the pore size is large enough that the electrolyte can infiltrate easily, resulting in a junction of huge surface area between the two continuous interpenetrating networks. Due to the wide bandgap of TiO_2 (~3.4eV), the film does not compete with the dye for absorption of visible light, and it is stable against photo-corrosion in the electrolyte due to the strength of its chemical bonds. Additionally, TiO_2 is abundant, biocompatible, and inexpensive.

The nanostructured geometry of the NP film has several important implications for its photoelectrochemical behavior. First, a depletion layer, which occurs when electrons move into the electrolyte from TiO_2 and produce upward band bending at the interface, cannot be formed because the particles are too small. Hence there is no significant electric field to separate the photo-generated electron-hole pair. Second, space charge limitation of the current is not observed due to screening by the electrolyte, meaning that the current is not limited by the electrons' mutual repulsion of each other due to their electric fields. Third, the interpenetrating TiO_2-

electrolyte interface causes the electrons to be transported by ambipolar diffusion, meaning that the motion of the electrons drags along positive ions in the electrolyte. Therefore, drift transport, which is essential to 1st and many 2nd generation solar cells, is not present.

One would expect electron transport in DSSC's to be inefficient since the NP network is randomly formed and the inherent conductivity is low. Experiments involving the light intensity dependence of the electron diffusion coefficient suggest that the transport is limited by the residence time of electrons in traps and the number and size of inter-particle connections. The latter is significant since the injected electrons must travel through an average of 10^6 nanoparticles in order to be collected[33]. Indeed trap limited diffusion is a slow process and can limit the DSSC efficiency. Many people, including Grätzel, have suggested that a higher degree of order is desirable in order to both improve electron transport and to allow the junction to be formed under better control.

2.2 Nanowire Dye-Sensitized Solar Cells

2.2.1 Introduction

The most common attempt to achieve enhanced order in DSSCs is to replace the NP film with a vertically aligned nanowire (NW) or nanotube (NT) array, which are commonly found to have a superior electron lifetime and diffusion length compared to the NP film. This idea is similar to the hybrid bulk heterojunction cells discussed above. This design, as schematically shown in Figure 2.6, may also improve DSSC efficiency in another way.

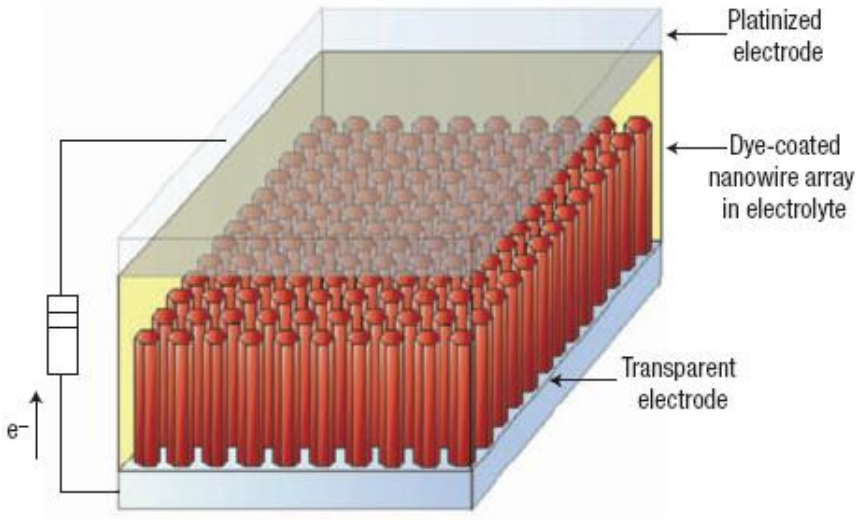

Figure 2.6: Schematic diagram of a nanowire-based dye-sensitized solar cell. Light is incident through the bottom. From reference[34]

Traditional DSSC's suffer from insufficient light harvesting in the 700nm-900nm range, and the development of dyes that absorb better in this range has been fairly unsuccessful. Increasing the NP film thickness to increase its optical density is also unsuccessful since the thickness is already limited by the electron diffusion length. With a NW or NT array, however, the thickness can be selected for maximum absorption without affecting the electron collection efficiency due to the high diffusion length. The first device of this form was reported for ZnO NW's by Law *et al* in 2005, to have an efficiency of 1.2-1.5%, due primarily to a low I_{SC} and FF[34]. Electron transport was shown to be improved due to the enhanced crystallinity and internal electric fields that can separate the electrons from oxidizing species in the electrolyte since the NW diameter is large enough to support a depletion layer and upward band bending at the surface. I_{SC} was limited primarily by a roughness factor (and hence dye-loading) that was about 80% lower and a FF that was about 50% lower than traditional NP based DSSCs. Since this paper, many similar attempts have been made using both NW and NT arrays, but the efficiency still fails to compete with the > 10% energy conversion efficiency reported for the NP-based DSSC. Many

explanations have been proposed for the poor performance, including an insufficient surface area for dye adsorption compared to the NP film, air trapped inside the NT's, and a large series resistance between the NW or NT and the barrier layer or conducting substrate.

2.2.2 TiO_2/Carbon Nanofiber Core-Shell Nanowire DSSCs

In 2009, Liu *et al* at Kansas State University and University of Kansas[35] reported a novel NW DSSC design which avoided the above failure mechanisms and showed particular promise. A schematic of the solar cell is shown in Figure 2.7(a).

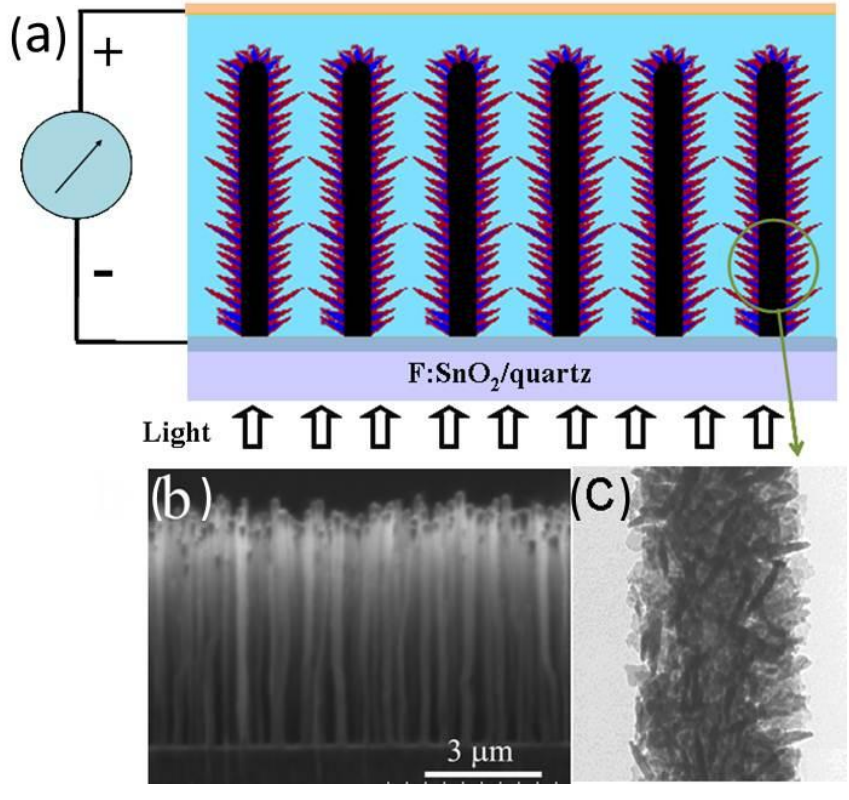

Figure 2.7: (a) Schematic of vertically aligned carbon nanofibers (CNFs) coated with TiO_2 nanoneedles for DSSC. (b) Scanning electron micrograph of CNF array. (c) Transmission electron micrograph of a CNF coated with TiO_2 nanoneedles. The diameter of the NW is ~ 250 nm

The solar cell consists of an array of vertically aligned carbon nanofibers (CNFs) coated with nanostructured anatase TiO_2. The CNF array, shown in Figure 2.7(b), consists of vertically aligned fibers with diameters around 80 nm and was grown by plasma-enhanced chemical vapor deposition on a quartz slide coated with 15 μm fluorine-doped tin oxide (FTO), a popular transparent conductor. The average nearest neighbor distance is 300 – 400 nm, leaving sufficient open space for TiO_2 growth, dye adsorption, and electrolyte penetration. A TiO_2 layer was then deposited on the CNF array via metal organic chemical vapor deposition. The TiO_2 film forms an interesting nanoneedle-like structure which wraps uniformly around each CNF, as shown in Figure 2.7(c). The titania film forms a conformal particulated film within 30 minutes growth time. With a longer deposition of 60 minutes, the particles elongate into nanoneedles stacked on the CNF surface. This high degree of structure provides an enhanced surface area for dye-adsorption, which is an improvement over previously reported smooth NWs and NTs. The work function of CNFs is presumably similar to graphite (4.5 – 5.0 eV), which matches well with FTO. Because of the desirable band alignment between CNF and TiO_2, electrons in the conduction band of TiO_2 will readily be transferred to CNF for transport to the anode. CNFs have an intrinsic resistivity of CNFs is 0.4 – 7 $m\Omega \cdot cm$[36–38], which is a few hundred times lower than the ZnO NWs utilized by Law *et al*[34], making them an excellent electron collector. Instead of electrons traveling through a 10+ μm thick TiO_2 NP film, they only must travel radially through the thin TiO_2 shell before being transported to the anode through the conductive CNF core.

The I-V curve of a DSSC constructed with these core-shell NWs is shown below in Figure 2.8 (a). The TiO_2/CNF DSSC provided a short circuit current density (J_{SC}) of 2.91 $mA \cdot cm^2$, which is approximately 10 times lower than traditional NP DSSCs and comparable to

ZnO NW DSSC. The V_{OC} and *FF*, however, are respectable. As shown in Figures 2.8 (b-c), the photocurrent and photovoltage are stable over several light ON-OFF cycles, suggesting the device is stable, at least for short times. The efficiency of 1.09 %, then is largely limited by the low photocurrent. Further evidence can be found in the incident photon to charge carrier conversion efficiency for different wavelengths, shown in Figure 2.8 (d). A narrow peak of nearly 35 % for 515 nm is observed, correlating with the peak absorption of the dye. This curve is broad and peaks near 90% in traditional NP DSSCs. This low photocurrent and hence efficiency in spite of the advantageous design of this solar cell is the basis for the individual nanowire work presented in the following sections of this chapter.

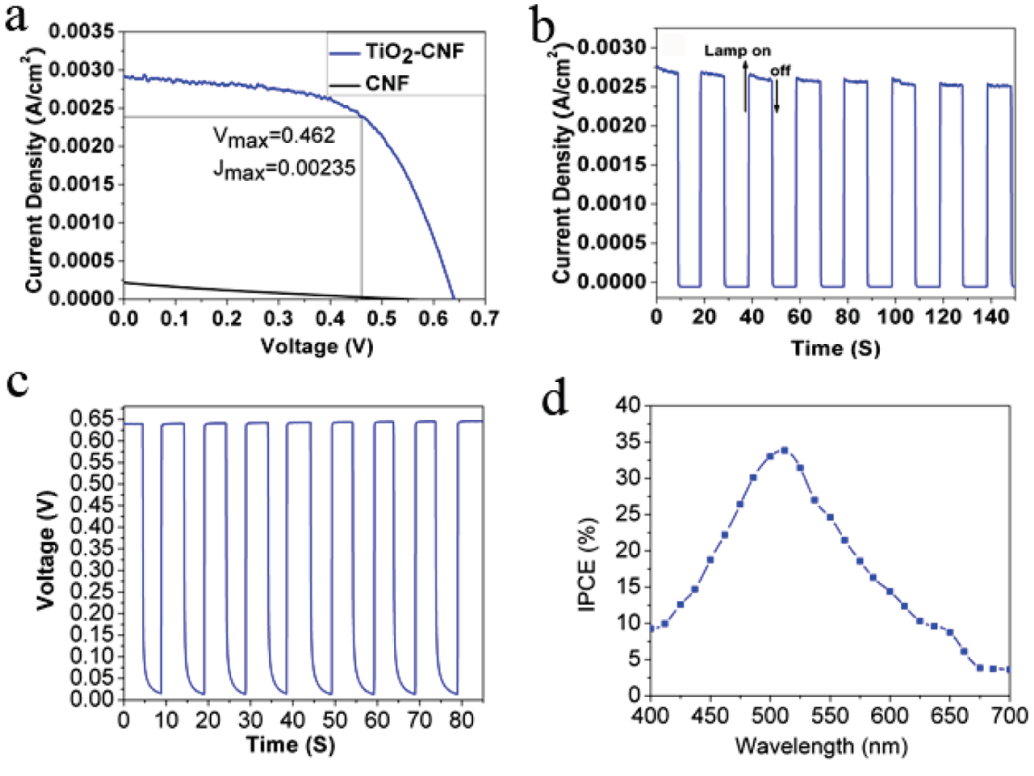

Figure 2.8: (a) I-V characteristics of a DSSC fabricated with a TiO_2 nanoneedle-coated carbon nanofiber array (blue line) and bare CNFs (black line). The current density and voltage at the maximum power point are marked. (b) Photocurrent and (c) photovoltage response during light ON-OFF cycles. (d) Incident photon to current conversion efficiency[35]

2.3 Motivation and Experimental Approach

2.3.1 Introduction

As discussed in the previous section, the CNF/TiO_2 core-shell DSSC design is especially promising because it offers several potential advantages over traditional NP DSSCs and previously reported NW or NT-based DSSCs. Despite these advantages, an efficiency of only 1.09 % was reported. The efficiency was limited primarily by a low I_{SC}. This could be caused by several different things, including but not limited to low dye loading, back reactions between electrons in the TiO_2 and oxidized dye molecules or oxidized species in the electrolyte, poor electron transport, or a poor CNF/TiO_2 interface. Within the bulk device structure, one is unable to determine which mechanism(s) limits the efficiency. Furthermore, it is difficult to learn much about the CNF/TiO_2 core-shell NWs themselves. They form the basic units of the DSSC, and therefore the DSSC is only as good as the NWs. An in depth understanding of the NWs is therefore essential for optimization of the bulk DSSC.

The method we utilize to overcome these hurdles is to isolate a single CNF/TiO_2 core-shell NW from the DSSC and study its properties under various conditions. By isolating a single NW one is able to obtain information which is not available in the bulk device. Furthermore, one can eliminate averaging and bottlenecks due to un-optimized fabrication techniques. This is especially important for the DSSC, whose performance is highly affected by packaging techniques, the best methods of which are not freely shared by the Grätzel group. Once an individual NW device is fabricated, one can treat it in various ways, such as chemically or thermally, and determine the effects of those treatments on its properties. The ultimate goal of

this approach is to correlate the physical nanoscale properties with the optoelectronic properties relevant to device performance.

In order to simplify the interpretation of the data and address a major issue, the 60 minute growth core-shell NWs were not used. In unpublished work by Liu and coworkers, it was observed that the TiO_2 nanoneedles fell off of the CNF after approximately 60 minutes in the electrolyte solution. Comparative before and after scanning electron micrographs are shown below in Figure 2.9.

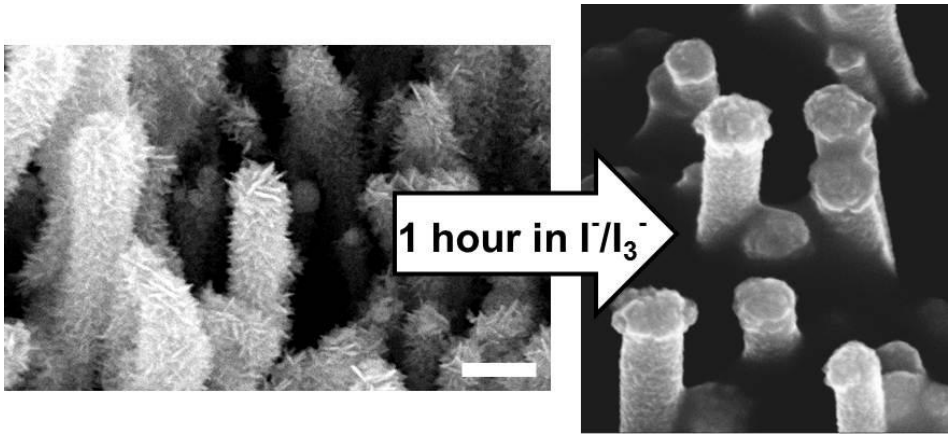

Figure 2.9: Scanning electron micrograph of the CNF/TiO_2 core-shell nanowire array before (left) and after (right) soaking in the DSSC electrolyte for ~ 1 hour.

It can be clearly seen that all that remains after soaking in the electrolyte are the CNFs and a thin layer of TiO_2. This suggests that the interfacial layer between CNF and TiO_2 may be of poor quality and susceptible to corrosion in the electrolyte. In order to study this layer, NWs that underwent 30 minutes of TiO_2 growth instead of 60 minutes were studied. As a reminder, after 30 minutes growth the TiO_2 forms a complete, conformal particulated layer around the CNF but has not yet started to elongate into nanoneedles. An added benefit of studying 30 minute instead of 60 minute NWs is that we can focus on charge transport through TiO_2 and transfer to CNF instead of between nanoneedles, which could be the subject of future work.

2.3.2 Sample Fabrication

In order to fabricate individual CNF/TiO_2 core-shell NW devices, the as-grown NWs were dispersed into ethanol and transferred onto a silicon substrate covered with 500 nm thermally grown silicon dioxide. Bi-layer electron beam resist (MMA-MAA / PMMA) was used in the electron beam lithography (EBL) process for definition of two or four electrodes. Before electrode deposition, a subset of the samples was treated with O_2 plasma at 20 W for 30 seconds via reactive ion etching (RIE) at a pressure of 7.1 mTorr in order to remove any possible residual electron beam resist and other surface contaminants which could prevent Ohmic contact between the electrodes and TiO_2 shell. Ti (15nm)/Au (120nm) electrodes were deposited by using electron beam evaporation through the EBL defined mask followed by liftoff with acetone. After fabrication, all samples were annealed at 400ºC for 30 min with a temperature ramping rate of 15ºC/min. The annealing was performed in vacuum at a pressure of ~10^{-5} Torr or better, with the intention of avoiding oxidation of Ti in the bottom layer of the electrode and desorbing any possible residual chemicals on the surface of the nanowire due to the above processes. To attach dye molecules onto the TiO_2 surface of the CNF/TiO_2 core-shell NW device, the O_2 plasma treated and untreated samples were soaked in 0.2 mM ethanol solution of cis-bis (isothiocyanoto) bis (2,2'-bipyridyl-4,4'-dicarboxylato)-ruthenium(II) bis- tetrabutylammonium dye (N719, Solaronix) for 12 hours and blown dry with dry N_2. The soaking and mounting of the samples were performed in dark in order to limit the premature exposure of the devices to light. The prepared samples were enclosed in an aluminum box in order to measure the dark I-V characteristics before exposure to one sun illumination (100mW/cm^2) produced by a solar simulator outfitted with an AM 1.5 G filter (Newport).

2.4 Photoconductivity and Dye Adsorption Studies

2.4.1 Introduction and Microstructural Characterization

The first set of studies on these CNF/TiO_2 core-shell NW devices revolved around the photoconductivity and the effect of dye adsorption. This served to provide a baseline and establish the inherent transport properties of the NWs. Figure 2.10(a) schematically depicts the structure of the CNF/TiO_2-dye core-shell NW device. It consists of a CNF/TiO_2 core-shell NW with two metal electrodes on the surface of the TiO_2 sheath. A scanning electron microscopy (SEM) image of a representative CNF/TiO_2 core-shell NW device is shown in Figure 2.10(b).

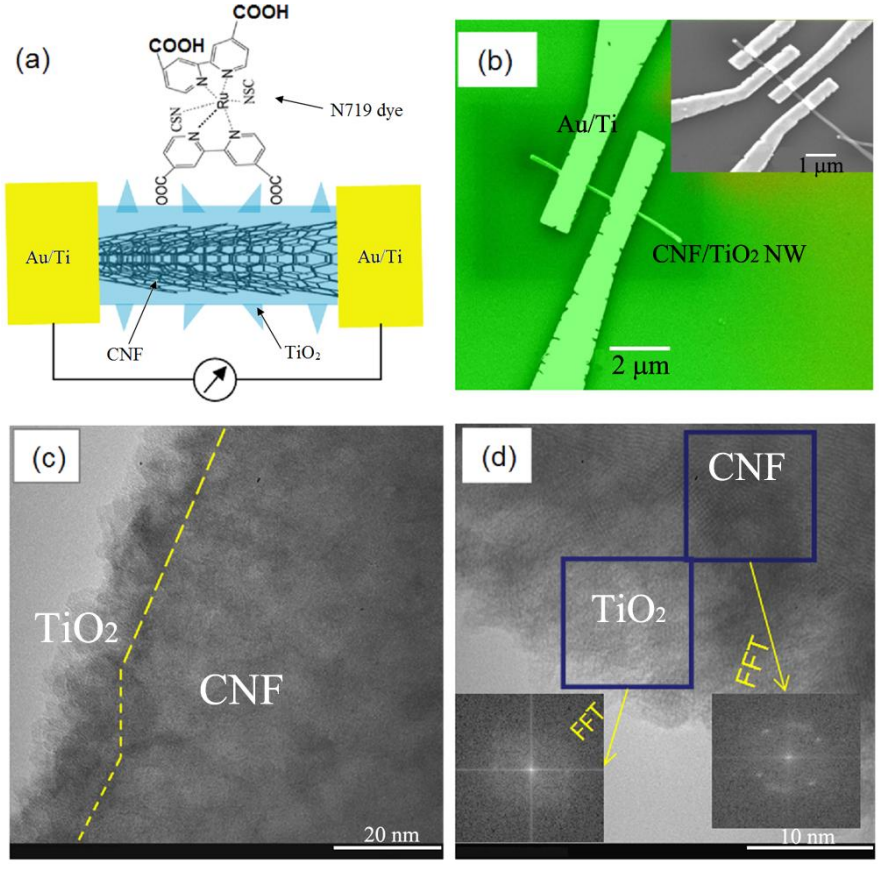

Figure 2.10: (a) Schematic diagram of a single CNF/TiO_2 core-shell NW device. (b) SEM image of a device used in the study. Inset shows a four-probe device used to measure contact resistance and resistivity. (c) TEM image showing the core-shell structure. The yellow dashed line shows

the interface between TiO_2 shell and CNF core. (d) Microstructure of the core-shell NW, insets give the FFT results for the core and shell, respectively.

The NW in the device has a stem length of ~ 4 micrometers. Additionally, a four-probe device is shown in the inset of Figure 2.10(b), which was fabricated to measure the contact resistance between the metal probes and the NW. The CNF core of the NW has an average diameter of ~ 100 nm while the TiO_2 sheath of the samples used in this study is about 10-15 nm thick[39]. The microstructures and morphologies of the CNF/TiO_2 core-shell NW were studied using high-resolution transmission electron microscopy (HRTEM). As shown in Figure 2.10(c), TiO_2 forms a conformal particulate film surrounding the CNF core, covering the CNF core uniformly even at a kink of the CNF, which is shown by the dashed line at the interface of the core and shell. Fast Fourier Transform (FFT) was used to analyze the crystalline structure of CNF core and TiO_2 shell. Distinct ordered planes as suggested by the discrete spots were observed on CNF [right inset of Figure 2.10(d)] while a mixture of compact fine grains several nanometers in size embedded in an amorphous phase was suggested for the TiO_2 sheath [left inset of Figure 2.10(d)]. X-ray diffraction analysis on CNF/TiO_2 NW array indicates the fine grains are anatase TiO_2[39]. HRTEM suggests the dimension of the grains is in the range of 3-5 nm.

2.4.2 Steady State I-V Characteristics

Figure 2.11(a) shows the *I-V* characteristics of Sample *d1*, which is a representative in a group of six samples not treated with O_2 plasma, in dark and under illumination before and after dye attachment. Although only the positive bias is shown, it should be noted that the curve is symmetric. Contact resistance in the range of 3-8 MΩ was typically observed for the untreated samples with a contact area of approximately 0.15 μm^2. As previously mentioned, this large

contact resistance is likely due to a contaminated TiO_2 surface which may prevent Ohmic contact between Ti and TiO_2 during metal evaporation and the diffusion of Ti to TiO_2 during annealing. Before dye attachment, Sample *d1* exhibits a considerably high dark current (open black circles). This may be attributed to the large number of dangling bonds and the interfaces in the amorphous TiO_2 phase and between crystallites and amorphous TiO_2 phase in the TiO_2 sheath. The resulting high density of oxygen vacancies may act as electron donors and therefore cause substantial dark current. The illuminated current (open red circles) is only slightly higher than the dark current before dye attachment, which may contain direct band transition in the TiO_2 (E_g~3.4 eV) close to the UV end of the solar spectrum and sub-band transition of TiO_2. The sub-band transition is commonly seen in nanostructured TiO_2 and is due to localized defect-induced band gap states. Furthermore, the measurement on uncoated individual CNF samples (not shown) exhibits no photoresponse under the conditions presented in this paper, suggesting the observed photoresponse is due to the TiO_2 or dye only.

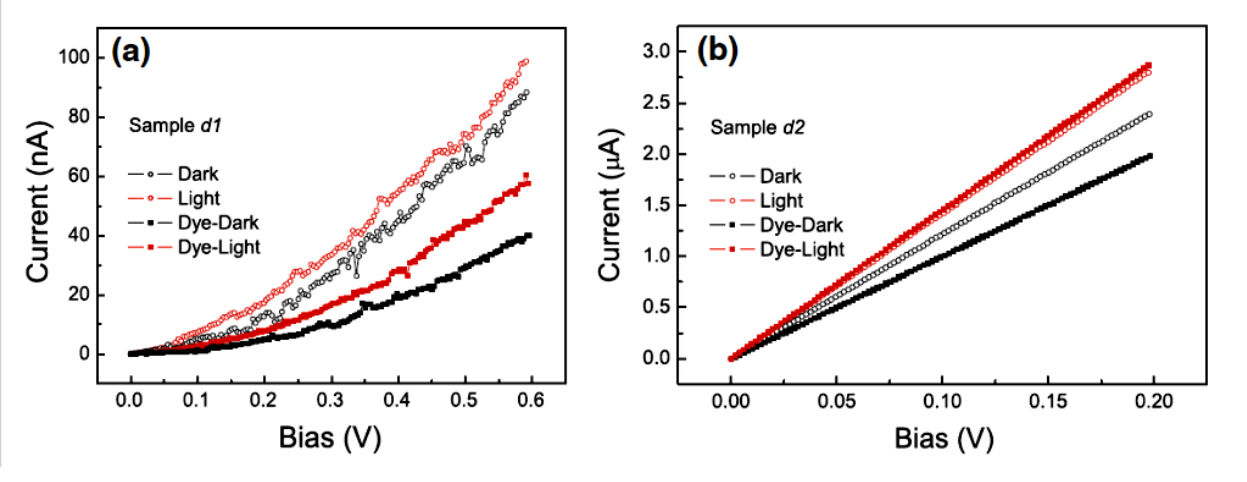

Figure 2.11: (a) Dark and illuminated I-V curves for Sample *d1* without and with dye and (b) the corresponding curves for Sample *d2*.

After attaching dye molecules, the dark (solid black squares) and illuminated (solid red squares) current of Sample *d1* decreased noticeably as shown in Figure 2.11(a). We speculate

that the decrease is due to the passivation of some hole traps during the dye attachment. The current decrease may then be explained in the following way. It has been suggested that non-equilibrium holes rapidly become trapped in deep traps which may be concentrated in particular regions due to inhomogeneity in the lattice such as grain boundaries. These traps produce a local potential barrier which prohibits electrons from readily recombining with the holes, thus separating charge carriers and improving conductivity[40]. The N719 dye is expected to attach to the TiO_2 surface via its carboxyl group[41]. While the sample is soaking in solution, the protons that previously resided on the now negatively charged carboxyl group may passivate some of the hole traps near the surface. These hole traps are commonly associated with oxygen vacancies, which can readily occur on the surface as well as at the grain boundaries within the nanocrystalline/amorphous TiO_2.

Even though both the dark and illuminated currents decreased, the photo-induced current, defined as the difference between the illuminated and dark currents at a particular bias, increased after dye attachment. This suggests that the dye molecules do in fact contribute to the photo-induced current, or more specifically the free electron density. This may occur in three ways. First, the dye molecules may inject photo-excited electrons into the TiO_2 layer and increase the electron density. It should be recognized that dye regeneration may not occur effectively in this case due to absence of the electrolyte, so this mechanism is not expected to contribute to the measured current. Second, the presence of the dye molecules may modify the number of the hole traps, as argued earlier. This mechanism will be demonstrated further via transient photoconductivity measurements. Third, since the measurements occur in air which contains molecular oxygen, a known electron scavenger[42], the presence of the dye molecules may block some of the molecular oxygen from removing conduction electrons and forming adsorbed O_2^-

sites which decreases the free electron density in the TiO_2. Measurements of single CNF/TiO_2 nanowires in vacuum (not shown) exhibit a current that is 1-2 orders of magnitude higher than in air. This is in qualitative agreement with studies on thin films of nanocrystalline TiO_2[43,44] in which environments containing lower oxygen content resulted in higher current due to the decreased number of electron scavengers. This suggests that blocking access to the surface of the TiO_2 would have a similar effect and thus increase the electron concentration and hence current.

The I-V measurements were repeated on Sample *d2*, which is representative of the samples with electrode contact area treated with O_2 plasma before electrode deposition. The O_2 plasma treatment improved the electrical contact to the CNF/TiO_2 NW considerably as shown in Figure 2.11(b). From four-probe measurements, the contact resistance of the treated samples is several to several tens of kΩ, which is two to three orders of magnitude smaller than that of the untreated samples. The resistivity of Sample *d2* is estimated to be $(6.4 \pm 2.1) \times 10^{-2}$ Ω·cm. This value seems reasonable since it lies between the intrinsic resistivity of CNF ($0.4\text{-}7\times10^{-3}$ Ω·cm[36,37]) and that of TiO_2 thin films ($2.6\times10^{-1}\text{-}10^{6}$Ω·cm[45,46]). The low resistivity of the core-shell nanowire compared to thin film TiO_2 suggests that the CNF does in fact contribute to the charge transport even when both electrical contacts are on the TiO_2 shell. This indicates low resistance across the CNF/TiO_2 interface. This low-resistance interface may be understood from the growth chemistry of the TiO_2 shell on CNF. During PECVD, a mixture of C_2H_2 (at 62 sccm) and NH_3 (at 252 sccm) was used as gas precursor. Particularly, the NH_3 content is about four times that of C_2H_2. This generates an important plasma etching effect to remove the amorphous carbon which may be deposited at the CNF surface. For many carbon nanotube studies the amorphous carbon has been the major factor affecting the interface properties. The hydrogen atoms covalently bonded to the CNF surface at the graphitic edge do not seems to be a problem.

Four-probe electrical measurements with side contact by Zhang *et al*[37] did not show any evidence of an interface problem. In addition, during growth of TiO_2, the oxygen atoms involved in the reaction will likely react with hydrogen and form a C-O bond before TiO_2 is deposited. The I-V characteristics become more linear after O_2 plasma treatment, which indicates an Ohmic contact on the metal-semiconductor interface. The reduction of the contact resistance results in a significant current enhancement of almost two orders of magnitude both in dark and under illumination as compared to the untreated Sample *d1*. In addition, the photo-induced current in Sample *d2* is significantly higher than in *d1*. At 100 mV bias, the photo-induced current in Sample *d2* is ~0.21 μA after dye attachment, which is about two orders of magnitude higher than in the untreated samples. This result confirms that an Ohmic contact to the nanostructured materials is essential to the charge transport in a NW device[47,48].

The O_2 plasma treatment was also applied to the TiO_2-dye interface in order to examine if a similar residue or interface layer was present which could hinder dye adsorption. To make a direct comparison, the dye was removed from Sample *d2* before it was subjected to O_2 plasma cleaning under the same processing conditions mentioned earlier except for a longer processing time of one minute. Immediately after the treatment, the sample showed an enhanced photo-induced current which decayed back after 12 hours in the dark in air. Dye was then attached using the previously described method, and the photo-induced current recovered more or less the original value shown in Figure 2.11. This observation suggests that the surface of the TiO_2 was clean with respect to dye attachment.

2.4.3 Spectral and Intensity Dependence

The spectral dependence of the photo-induced current (Sample *d2*) before dye attachment is illustrated in Figure 2.12(a). Two peaks are clearly visible. The first is at wavelengths smaller than 375 nm which corresponds to a bandgap of ~3.3 eV and is within the reported range for nanocrystalline TiO_2[49]. The second peak appears around 550 nm, which has been observed on TiO_2 nanoparticles and is attributed to the sub-band transitions[39]. Interestingly, no such peak was observed on the photoluminescence curve measured on TiO_2/CNF array with 60 minutes of TiO_2 growth time[39], as opposed to 30 minutes for the samples used in this work. A plausible explanation is the much improved crystallinity in TiO_2 layer with longer growth time, which resulted in much reduced sub-band charge carriers. On the other hand, the direct transport measurement employed in this work may provide higher sensitivity than the optical one. As we mentioned earlier, the possible contribution of the CNF core to the spectral feature of the photo-induced current can be ruled out. In fact, the same spectral current measurement was repeated on individual CNF devices and no photo-induced current was observed.

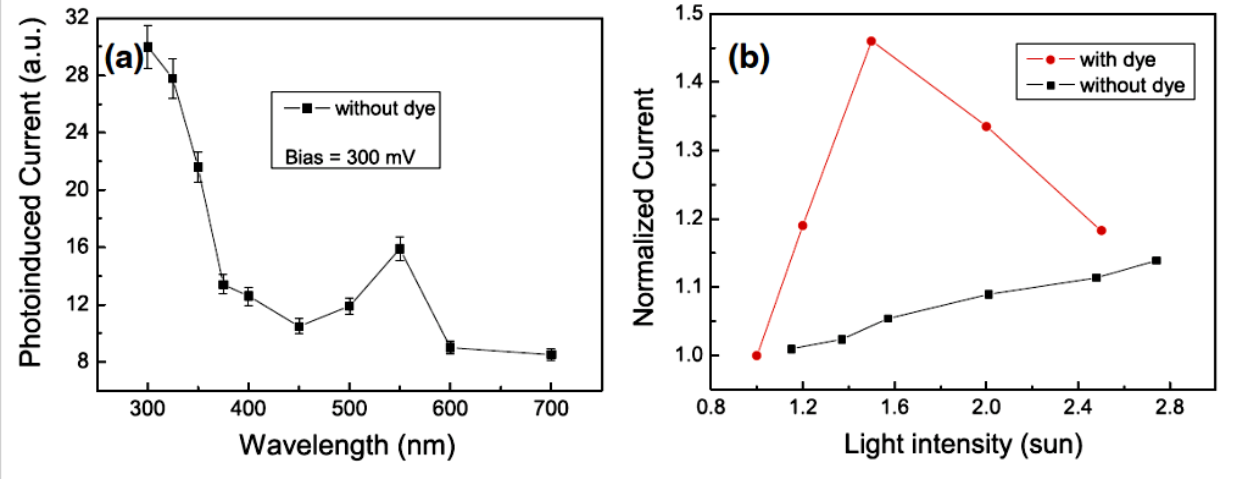

Figure 2.12: Photo-induced current at constant bias for a single CNF/TiO_2 NW device as a function of (a) incident light wavelength and (b) white light intensity

Figure 2.12(b) shows the photo-induced current (normalized to that at 1 Sun) for Sample *d2* with and without dye as a function of incident light intensity. Before dye attachment, the current increases linearly with the light intensity, which indicates the carriers excited in TiO_2 is proportional to the number of incident photons. However after dye molecules were attached to the NW, the photo-induced current vs. light intensity curve experienced a dramatic drop at a light intensity of around 1.5 suns. This phenomenon may be attributed to the bleaching effect of dye molecules. After dye molecules were damaged above a certain light intensity, they may be detached from the TiO_2 surface. Based on the above discussion, this would reintroduce many electron traps and open up the TiO_2 surface to electron scavenging by molecular oxygen leading to a decrease in the number of free electrons.

2.4.4 Transient Photoconductivity

While the previously mentioned I-V measurements were made under steady state conditions, the samples in fact exhibit a transient response to either the introduction or removal of incident light. The presence of transient photoconductivity is well documented in nanocrystalline TiO_2 thin films[43,44,49], but is interesting to observe in a single NW. In this measurement, the samples were first exposed to one sun illumination at a constant bias of 100 mV. The high surface–to-volume ratio and thus high density of electron traps due to hydroxylated surface Ti sites[50] prevents achievement of steady state current until all traps are filled and equilibrium is reached between trapping and de-trapping events. It was observed (not shown) that after dye attachment, the time required to reach steady state current was reduced by approximately 75%. This suggests that the dye molecules may passivate many of the hydroxylated surface Ti sites and greatly reduce the number of electron traps. However, since

nearly one minute is still required to reach steady state current after dye molecules are attached, it is likely that many potential dye adsorption sites remain and the dye loading is not optimized. Once a steady state current was achieved, the incident light was removed and the photo-induced current decay was recorded. Figure 2.13 shows the normalized photo-induced current decay profile in log-log and linear scale (inset) for samples without and with attached dye molecules. The mechanism responsible for the observed slow current decay may be described as follows. As previously mentioned, under illumination nonequilibrium holes become trapped in deep traps due to oxygen vacancies leading to an excess electron density equal to the trapped hole density[51]. These traps are assumed to be concentrated in certain regions due to inhomogeneities such as grain boundaries. This leads to local electric fields which spatially separate charge carriers and require electrons to overcome a potential barrier in order to recombine[40]. As time goes on, the separation between the quasi Fermi levels increases causing the recombination time to increase along with it.

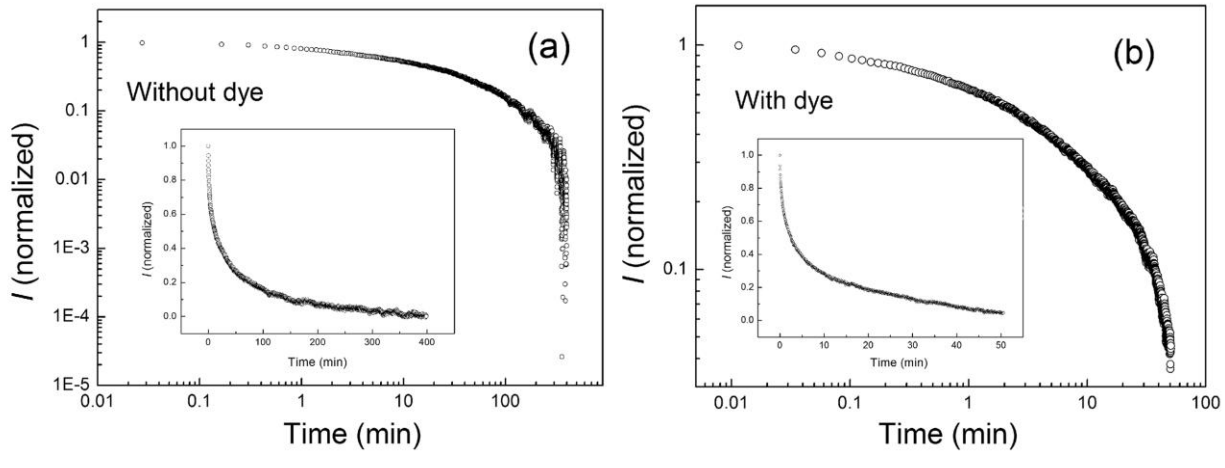

Figure 2.13: Normalized photo-induced current decay of Sample *d2* (a) without dye and (b) with dye. Inset shows the same data on a linear scale.

As can be seen in Figure 2.13, the decrease in current is immediate and initially very fast followed by a much slower leveling off as the probability for the electron capture by tunneling through surface and inter-grain potential barriers decreases, which is consistent with previous work done on nanocrystalline TiO_2 thin films[44]. It can be clearly seen that the photoconductivity decay is more rapid when the dye is present. This is consistent with the above observations that the dye attachment passivates some hole traps on the surface. As the number of hole traps decreases, the recombination time also decreases.

2.4.5 Conclusion

In conclusion, electrical conductivity has been investigated on individual CNF/TiO_2 core-shell NW attached with N719 dye molecules in dark and under illumination. It has been found that the contact resistance to the TiO_2 surface may sensitively affect the dark and photo-induced conductivity by nearly two orders of magnitude, suggesting that care must be taken to ensure Ohmic contact between the TiO_2 structure and the anode in the DSSC. The nanocrystalline state of the TiO_2 shell affects both spectral and dynamic behaviors of the conductivity due to the presence of the defect-induced bandgap states and hole traps such as oxygen vacancies. The dye attachment reduces such an effect by passivating some of the vacancies at low illumination intensity up to 1.5 suns, above which damage to and subsequent detachment of the dye molecule may occur. The single nanowire approach presented in this work may be applied to many nanostructures involved in nanostructured DSSC and other optoelectronic devices to achieve an understanding of the electrical transport at the nanoscale.

2.5 Thermal Annealing Studies

2.5.1 Introduction and Microstructural Characterization

The work presented in this section on TiO_2/CNF core-shell NWs is a follow up to the work in Section 2.4. Sample fabrication follows the procedures outlined in Section 2.3.2, except that all samples now underwent the oxygen plasma treatment before electrode deposition in order to improve electrical contact. Since the above photoconductivity study gave some insight into the importance of the crystalline quality, this work utilizes a single NW approach to study the role of the semiconductor microstructure as related to DSSC performance in CNF/TiO_2 NW's. The microstructure is important to study since it may sensitively affect dye adsorption, electron transfer from the dye, and electron transport to the core, all regarded as main functions of the semiconductor. Analysis of two sets of nanowires is presented, one of which underwent an annealing treatment in air to improve the crystallinity.

Figure 2.14(a) shows a TEM image of a typical CNF/TiO_2 nanowire used in this study. From this and additional TEM images (not shown), the CNF core was found to have an average diameter near 100nm, while the TiO_2 shell was found to be 20-25nm thick.

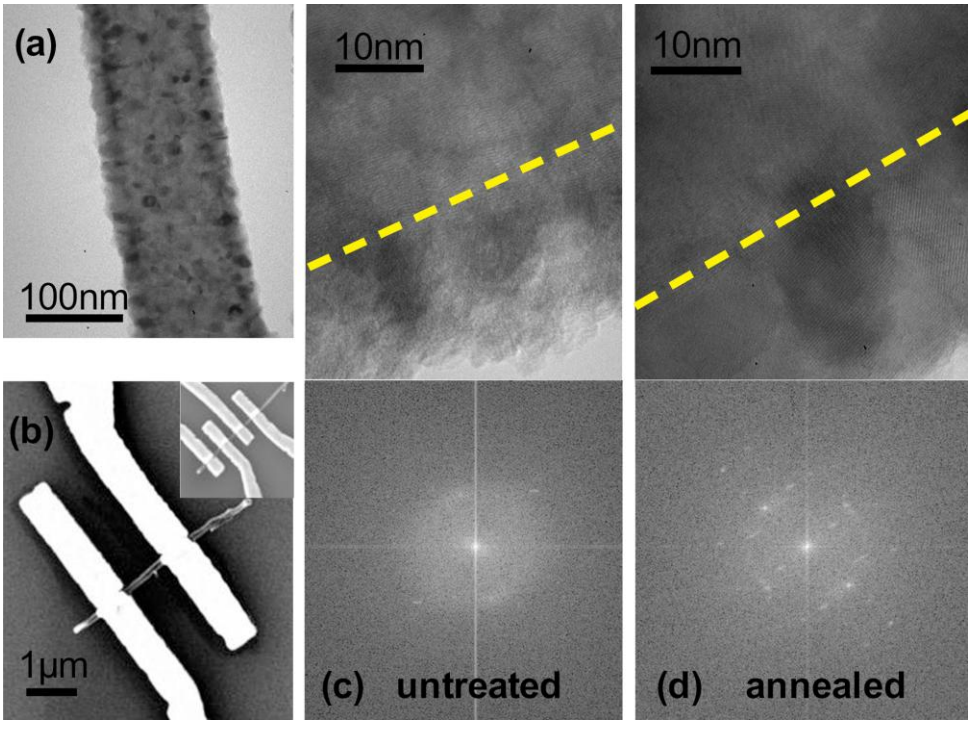

Figure 2.14: (a) TEM image of CNF/TiO_2 nanowire used in this study. (b) SEM image of a two probe CNF/TiO_2 nanowire device prepared for single nanowire measurements. (c) and (d) High resolution TEM images (top) and FFT (bottom) of an untreated and annealed nanowire showing the difference in crystalline order. The location of the interface between CNF and TiO_2 is marked with a dashed line.

Figure 2.14(b) shows a typical scanning electron micrograph of a single CNF/TiO_2 NW with electrodes after completion of all fabrication steps. The length of each nanowire is approximately 4-6μm. Figures 2.14(c) and 2.14(d) show a representative HRTEM image and Fast Fourier Transform (FFT) pattern for each class of nanowires used in this study. The TiO_2 shell surrounds the CNF core uniformly, and the location of the interface between the core and shell is marked with a straight dashed line for clarity. The untreated sample is shown on the left in Figure 2.14(c) and the sample which underwent an extra annealing treatment is shown on the right in Figure 2.14(d). The top halves of Figures 2.14(c-d) show images of the edge of the nanowire sidewalls, where it appears that the annealed sample contains larger crystallites with distinct ordered planes, while the untreated sample contains smaller crystallites mixed within an

amorphous phase. The average crystallite size appears to have increased from 5-9nm to 10-15nm after the annealing treatment. The bottom halves of Figures 2.14(c-d) show FFTs of the high resolution images and illustrate the change in overall crystalline order between the two samples. The pattern in the FFT of the untreated sample in Figure 2.14(c) shows continuous rings and a weak pattern of discrete spots, which indicates the presence of amorphous TiO_2 and some fine crystallites. By comparison, the annealed sample shows multiple sets of discrete spots in the FFT of Figure 2.14(d), indicative of the larger TiO_2 grains observed in the image. A close examination of Figure 2.14(d) suggests that these single crystal grains form a continuous layer around the CNF core. This is further illustrated in Figure 2.15.

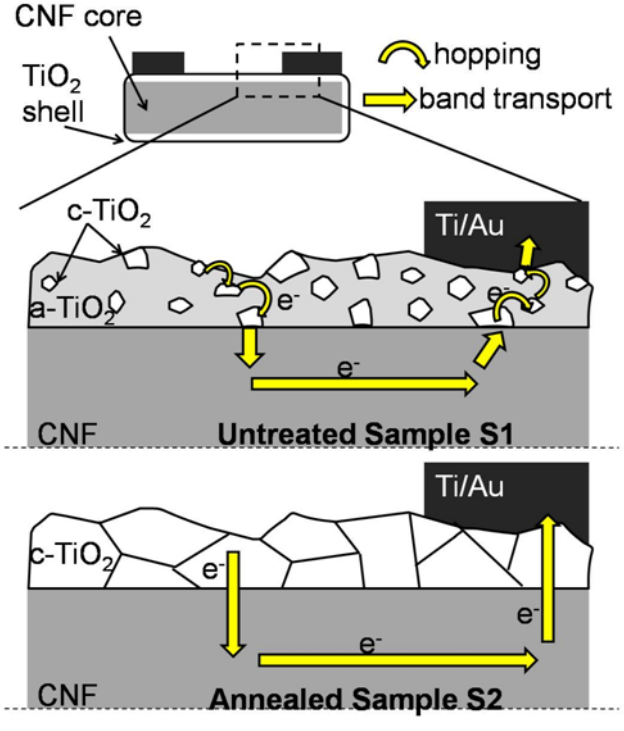

Figure 2.15: Cartoon illustrating the difference in charge transport between the untreated and annealed nanowires due to the crystallite size and presence of amorphous TiO_2.

2.5.2 Dark and Illuminated I-V Characteristics

Data from two representative samples are presented in this paper, although more than ten samples were investigated. *S1* is the untreated sample, and *S2* is the annealed sample. Dark and illuminated I-V characteristics of both samples with and without dye are shown in Figure 2.16. Based on four probe measurements, the resistivity was found to be 10^{-1}-$10^{-2}\Omega\cdot$cm for the untreated samples and 10^{-2}-$10^{-3}\Omega\cdot$cm for the annealed samples. These values lie between the reported ranges for a bare CNF (10^{-3} $\Omega\cdot$cm[36,37]) and anatase TiO_2 thin films (10^{-1}-10^{6} $\Omega\cdot$cm[45,46]). Reduction of CNF resistivity after annealing is not expected since chemical reactions that may occur involving the carbon atoms typically lead to higher resistivity compounds. The drop in resistivity is therefore attributed to the improved TiO_2 structural order, as follows. The untreated sample contains nanoscale crystallites embedded in amorphous TiO_2, the resistance of the former being several orders of magnitude lower than the latter[52], so that charges must hop between crystallites. The enhanced TiO_2 crystallite size may facilitate such "hopping" dominated charge transport by reducing or eliminating the amorphous gap between the crystallites. Again, this is illustrated in Figure 2.15.

As can be seen in Figure 2.16, both devices exhibit a significant dark conductance, generally accepted to be due to n-type doping caused by oxygen vacancies in TiO_2. Without dye, the dark resistance of *S1* is approximately twice that of *S2*, which is likely due to the improved charge transport in the more ordered TiO_2 layer of *S2*.

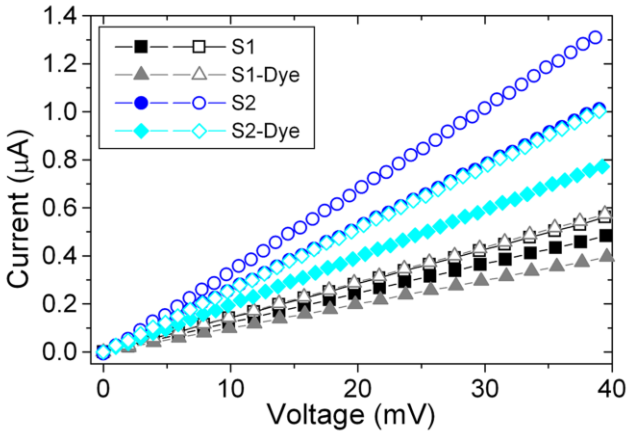

Figure 2.16: Dark (solid markers) and 1 sun (open markers) I-V curves for *S1* (black squares, grey triangles) and *S2* (blue circles, cyan diamonds) with and without dye, respectively.

Once again, it should be noted that the illuminated current is not a true photocurrent but rather represents photoconductivity. Additionally, individual CNF's were found to exhibit no photoresponse under the reported conditions, so any response is assumed to be due to TiO_2 only. Without dye, the illuminated current is 17% higher than the dark for *S1* and 30% higher for S2. The cause of the large photo-induced current, defined as the difference between illuminated and dark currents, for both samples has two main components: sub-bandgap absorption due to localized defect states within the bandgap[49] and photoconductivity due to hole trapping in the TiO_2 shell, which can be explained by a simple model proposed by Sheinkman and Shik[40]. Once a photon is absorbed, the photo-generated hole becomes trapped in a deep trap within the bandgap due to inhomogeneities such as oxygen vacancies. A localized potential barrier is produced which inhibits recombination and spatially separates electrons from trapped holes. The result is an increase in free electrons and thus conductivity.

The larger photo-induced current observed for Sample *S2* may be explained in the following way. Since the resistivity of amorphous TiO_2 is several orders of magnitude higher

than the resistivity within the crystallites, it can be approximated that the excitation of bandgap states within amorphous TiO_2 does not contribute to the measured current unless the excitation occurs very close to a crystallite so that the electron may hop to a lower resistivity region in order to be transported to the CNF core. Further, with a bandgap of 4.4eV (corresponding to a wavelength of 282nm), band to band transitions in amorphous TiO_2 are not expected to make a significant contribution to the current due to the small fraction of light in the solar spectrum with sufficient energy. It follows then that having a larger portion of the TiO_2 volume filled with crystallites may lead to a higher number of band to band excitations due to the lower bandgap and also a higher number of bandgap states that contribute to the photoconductivity if the effect of the anneal is to increase crystallite size but not necessarily decrease the defect concentration within the crystallites. This is supported by the intensity dependence of the photo-induced current shown in Figure 2.17.

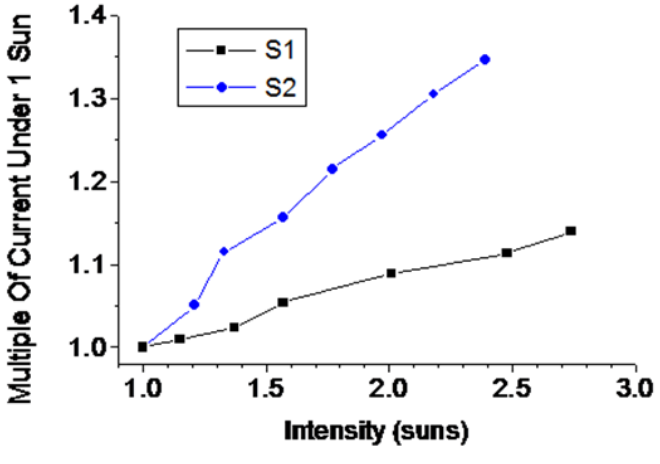

Figure 2.17: Intensity dependence of the photo-induced current of Sample S1 (black squares) and Sample S2 (blue circles).

The photo-induced current was measured at a fixed bias of 100mV in the range from 1 sun to approximately 2.5 suns. The current was normalized to the current under one sun for each sample in order to facilitate comparison. The data for each sample is nearly linear and increases monotonically, suggesting that the number of excited charge carriers is proportional to the number of incident photons, as expected. Sample *S2*, however, shows an enhanced response to increasing intensity as exhibited by factor of three increase in the slope over Sample *S1*. This supports the claim that the photons are more efficiently converted to collected electrons in Sample *S2* due to the larger volume portion of crystalline TiO_2.

Figure 2.16 also shows the dark and illuminated I-V characteristics of both samples after dye attachment. The dark conductivity is decreased after dye attachment for both *S1* and *S2*. This is likely due to the passivation of hole traps during dye attachment, particularly by protons which previously resided on the carboxyl group of the N719 dye before it became bound to TiO_2. It can be seen that the photo-induced current is increased for *S1* while it remains essentially constant for *S2*. It should be noted that the dye is unable to contribute directly to the current due to the absence of the electrolyte, and so the difference must be attributed primarily to conductivity, specifically free electron density. Molecular oxygen is a known electron scavenger on the surface of TiO_2[50], and the presence of dye molecules may be able to block the adsorption of molecular oxygen and the subsequent scavenging of conduction electrons to form O_2^- sites. During the annealing of *S2*, however, molecular oxygen can dissociate and fill oxygen vacancies on the surface and diffuse into subsurface regions. Since oxygen vacancies can act as active sites for chemisorption of molecular oxygen[42], electron scavenging may already be minimized in *S2* before dye is attached due to its improved surface stoichiometry. This is supported by work by Pan *et* al, which found that oxygen did not adsorb on stoichiometric TiO_2 surfaces[53].

2.5.3 Transient Photoconductivity

As previously mentioned, the samples exhibit transient photoconductivity, a well documented phenomenon in nanocrystalline TiO_2 thin films[43,49]. As can be seen in Figure 2.18, the current increases sharply after the onset of illumination and then levels off.

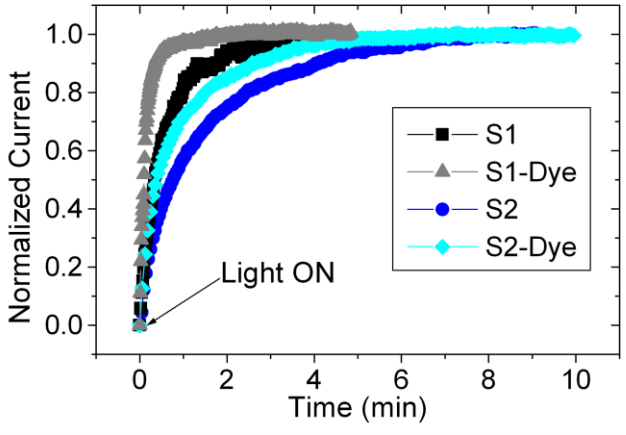

Figure 2.18: Normalized photo-induced current onset at 100mV for *S1* (black squares, grey triangles) and *S2* (blue circles, cyan diamonds) with and without dye, respectively.

Fitting the data to a simple exponential function results in time constants of 0.59 and 0.14 minutes for *S1* and 1.4 and 0.75 minutes for *S2* without and with dye, respectively. These differences are significantly larger than the observed sample to sample variability of a few seconds. The slow response is due to electron trapping via hydroxylated Ti sites on the surface and electron scavenging by oxygen molecules in the surrounding atmosphere[50]. A steady state current cannot be achieved until equilibrium is established between these events and their corresponding reverse processes. We have observed that in vacuum the NW's take a much longer time to reach a steady state current, which is in agreement with studies on thin film nanocrystalline TiO_2 in which this phenomenon has been attributed to an electron scavenging

rate which is proportional to the concentration of oxygen in the environment[43]. Since both measurements on *S1* and *S2* were made under the same conditions, the difference in rise times without dye could be attributed to a lower oxygen adsorption rate in *S2* due to its improved surface stoichiometry. It can also be seen that both samples experience a decrease in rise time with dye. This is likely due to the lower number of hydroxylated Ti sites and electron scavenging events on the surface due to dye attachment. Further, the drop in rise time is more drastic for *S1*, which supports the argument that the surface stoichiometry is improved in the annealed sample. A corresponding trend was observed in the photoconductivity decay times, shown in Figure 2.19.

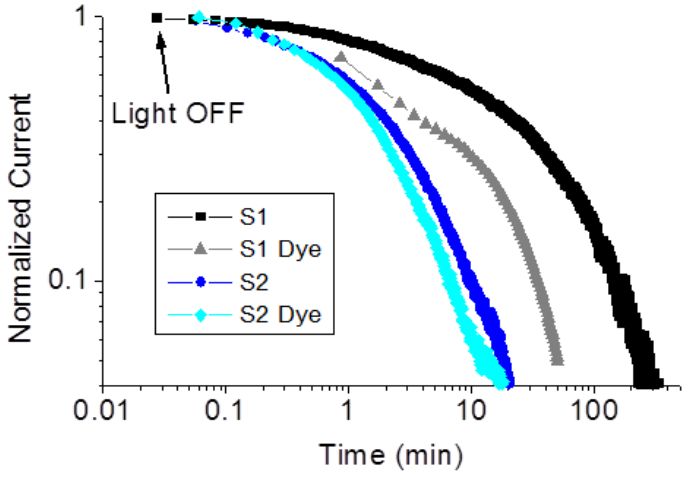

Figure 2.19: Normalized photo-induced current decay at 100mV for *S1* (black squares, grey triangles) and *S2* (blue circles, cyan diamonds) with and without dye, respectively.

The decay time, which depends on electron-hole recombination at hole traps, decreased after annealing and again after dye attachment for both samples. This supports the claims that annealing in air can decrease the number of oxygen vacancies and that dye attachment passivates hole traps. Kim *et al* found that reducing the number of oxygen vacancies on the surface of TiO_2

increased the amount of adsorbed N719 dye[54], which was explained by an increased electrostatic interaction between the $-COO^-$ groups of the dye and the Ti^{4+} sites on the treated surface compared to the Ti^{3+} sites on the surface with more oxygen vacancies. Therefore, taking steps to decrease the number of oxygen vacancies on the surface of the NW's could lead to a higher dye loading and thus higher photocurrent and efficiency.

2.5.4 Conclusion

In conclusion, the effect of annealing on the conductivity of single CNF/TiO_2 core-shell nanowires was studied in an attempt to elucidate the limiting factors of the CNF/TiO_2 NW array-based DSSC and motivate design constraints for future core-shell nanostructure-based DSSC's. The NW's which underwent an annealing treatment in air contained larger crystallites and much reduced amorphous TiO_2, which decreased the nanowire resistivity and increased photoconductivity. Further, since amorphous TiO_2 may not be able to effectively transport electrons to the CNF due to its high resistivity, any dye molecules adsorbed on the amorphous phase may be unable to contribute significantly to the DSSC photocurrent. The transient measurements suggest that the number of oxygen vacancies, which act as bandgap states and hole traps, is reduced in the annealed sample. This is beneficial for DSSC performance since it may increase the dye loading and also decrease the absorption of visible light by TiO_2. The results suggest that the optimal structure for a large surface area core-shell NW array for DSSC's would involve large crystallites with a stoichiometric surface which span the entire thickness of the shell.

2.6 Summary and Future Work

This work began as an attempt to identify the issues which limited the performance of the CNF/TiO_2 core-shell nanowire dye-sensitized solar cell developed by the research group of Jun Li at Kansas State University. The design, which was very unique and promising, underperformed with regard to short circuit current and efficiency. By simply growing the nanowires and assembling the solar cells without investigating the quality and properties of the nanowires, one is unable to diagnose the problems, and a low efficiency is not surprising. This work provided valuable information regarding the nanowire microstructure and how it affected the DSSC performance. Several failure mechanisms were suggested, along with a means to eliminate or minimize them. Professor Li's group has not reported any device with improved crystallinity, due in part to ongoing work to improve their packaging techniques. They have, however, done some studies on the improved nanowire arrays. They found that dye coverage could be doubled if they followed the annealing recipe suggested by this work, which was qualitatively predicted. Additionally, they found that the needles no longer fell off in the electrolyte, suggesting that the interfacial layer needed to be optimized. This should not only improve device stability but also electrical contact between the CNF and TiO_2. The growth and thermal annealing conditions still need to be optimized in order further improve efficiency utilizing this design. Ideally there would be an iterative process where systematic changes would be made to the NW fabrication process followed by optoelectronic characterization of individual nanowires in order to track the improvements and provide feedback into the growth and thermal annealing conditions.

The next stage for the individual CNF/TiO_2 core-shell nanowire project was to fabricate a working individual nanowire solar cell. The author made the decision to abandon this project for

reasons which will be discussed below. With some modifications, this could make an interesting project for another student who would like to pick up where the author left off. The intended design, shown in Figure 2.20, mimicked the assembly and packaging of the bulk DSSC, except only one nanowire would be used, and it would be on its side as opposed to standing up on the substrate.

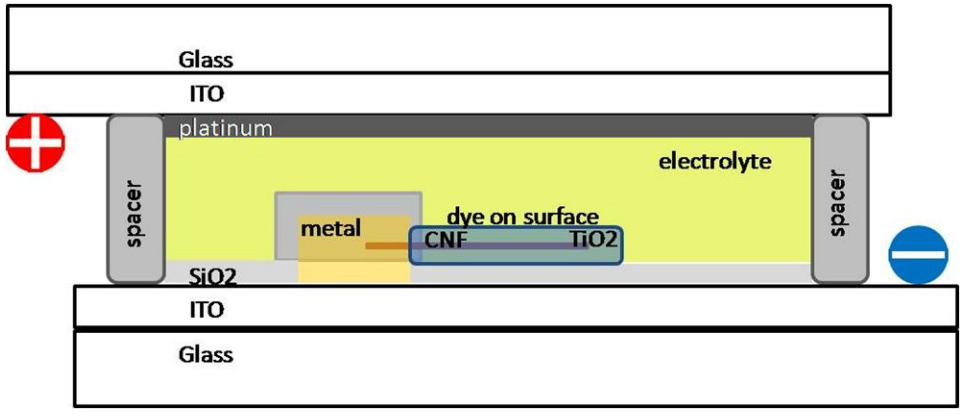

Figure 2.20: Schematic of the originally proposed individual nanowire DSSC. This design mimics the design of the bulk DSSC, except with a single nanowire.

The fabrication steps were to be as follows. First, an insulating layer, such as SiO_2, would be deposited on commercial indium-doped tin oxide (ITO) coated glass. The ITO would be one electrode. The nanowire would then be deposited on top of the insulator. A window would be opened above one end of the nanowire using electron beam lithography (EBL). The TiO_2 shell and underlying SiO_2 would be removed by reactive ion etching in CF_4 + H_2 plasma. Metal would then be deposited in order to connect the CNF core to the ITO. Another insulating layer would be deposited on top of the metal through a separate EBL step in order to prevent shorts between the two electrodes. Dye would be attached to the TiO_2, and the cell would be assembled in the standard fashion using a hot melt space to seal in the electrolyte and platinum-coated glass as the counter electrode.

The goal of this stage was to create a single NW DSSC in which essentially all parameters are controllable. In the bulk device, certain configurations and treatments are infeasible given its geometry and fabrication limitations. For example, the contact resistance between the NW's and the transparent conducting electrode on which they are grown cannot be controlled. Certain treatments to the TiO_2 surface, such as plasma treatment via reactive ion etching, may be difficult since the sidewalls are perpendicular to the substrate. Also, the power generation capability of an individual nanowire is unknown since averaging between very effective and very ineffective NWs may occur in the bulk device. By studying an individual NW in this DSSC device configuration, one is able to directly and quantitatively study the effect of various treatments, such as thermal, chemical, or plasma, on the solar cell figures of merit. One unique benefit of the DSSC assembly is that one is able to disassemble the cell, remove the dye, treat the nanowire in some way, re-adsorb dye, and repackage the cell. This way many treatments on *the same* nanowire are possible, if desired.

The author worked for several months on fabrication of this device. At the time the best available method for insulator deposition was electron beam evaporation. Unfortunately, oxides deposited this way are prone to pinholes and oxygen deficiency. This makes them semiconducting and permeable to the electrolyte, both detrimental to the device design. Much work was done to minimize this problem with no success. A better method would be to use atomic layer deposition (ALD) of aluminum oxide, which is now available in the research group. ALD would help minimize pinholes and also ensure a conformal, electrically insulating layer. Another issue which must be considered is that of clearly detecting the small current produced by this device. Current on the order of 1-100 pA is expected. The noise level is difficult to anticipate, but it is expected to be a non-trivial issue. Since the chip is of microscopic size, and

the electrolyte contacts the whole device volume, even a very tiny leakage current between the electrodes would easily mask the signal from the nanowire. A very clever device design may be able to minimize these issues. One must be careful, however, not to make the design so unlike the original design that the results are unable to be extended to the bulk DSSC.

Chapter 3

Individual Multiwall Carbon Nanotube Infrared Detector

3.1 Introduction to Infrared Photodetection

A photodetector measures photon flux or optical power by converting the energy in the absorbed photons into a measurable form[55]. This can be done via one of two methods. The first utilizes a photonic effect. By absorbing photons to promote electrons to higher energy levels, mobile charges are produced. If an electric field is present, the charges move to produce a measurable electric current. This effect can exist in two forms, external and internal. In the case of the former, the photo-generated electrons escape the material in the form of photoelectric emission; in the case of the latter, they remain in the material and increase the conductivity. The second method involves the conversion of photon energy into heat. While thermal detectors are typically less efficient and slower than photonic detectors due to the time required to effect a temperature change, they have gained popularity for military and commercial applications in recent years as resolution and sensitivity have improved dramatically. Hot electron bolometers, are the exception and can be very fast with speeds up to 10 GHz. They operate at cryogenic temperatures, however, which makes them less convenient.

In the case of photonic detectors, absorption of a photon by a semiconductor excites an electron from the valence band to the conduction band, resulting in a free electron in the conduction band and a hole in the valence band. In the presence of an electric field, both the electrons and holes are transported through the material to contribute to a current. Some photodetectors incorporate an internal gain mechanism to amplify the current and make the

signal more detectable. Photonic detectors most commonly either consist of a photoconductor or a photodiode, as described below.

Photoconductive detectors consist of an intrinsic semiconductor whose conductivity changes in response to absorption of incident photon flux. In these devices, an electric field is generated by an external voltage source in order to transport the photo-generated charges. Either the photocurrent or voltage drop across a serial load resistor is measured. Often times the anode and cathode contacts are interdigitated on the same surface of the material to maximize light reaching the photoconductor. The increase in conductivity from a photon flux Φ can be calculated as follows. Assuming the semiconductor volume is V and the fraction of incident photons producing an electron-hole pair is η, the electron-hole pair production rate per unit volume is $\eta\Phi/V$. If τ is the excess carrier recombination lifetime, electrons are lost at a rate $\Delta n/\tau$. Under steady state conditions both rates are equal, so $\Delta n = \eta\tau\Phi/V$. The change in conductivity is then

$$\Delta\sigma = \frac{\eta e \tau\left(\mu_e + \mu_h\right)}{V}\Phi, \tag{3.1}$$

where μ_e and μ_h are the electron and hole mobilities. The response time of a photoconductive detector is constrained by the transit time, which is limited by the mobility, and RC time constant.

Like photoconductive detectors, photodiode detectors also rely on photo-generated charge carriers for their operation. Instead of the conductivity however, the photodiode's reverse current increases when it absorbs photons. In a p-n junction diode, electrons and holes generated in the depletion region quickly drift in opposite directions due to the built in electric field.

Another option is the p-i-n junction diode, which has a number of advantages over the p-n diode due to the increased width of the depletion layer. First, there is more area available for absorbing light. Second, the greater drift length means that a higher proportion of the current is carried by the faster drift process instead of the slower diffusion process. Finally, increasing the depletion layer width reduces the junction capacitance and RC time constant. In addition to transit time and RC time constant, photodiode detectors possess a third contribution to the response time due to the diffusion of carriers that are generated outside, but sufficiently close to, the depletion region. Compared to drift, this is a relatively slow process. Nevertheless, photodiodes tend to be faster than photoconductors because of the large velocity brought about by the strong field in the depletion region.

Presently, most photonic infrared detectors are based on interband transitions in narrow bandgap semiconductors such as HgCdTe and InSb. The desire to further extend the operational wavelength range and decrease production costs by utilizing a mature processing technology led to work on quantum well infrared photodetectors[56] which utilize intraband transitions. Similar in design but boasting many potential benefits, quantum dot photodetectors have also been proposed and realized[57]. Normally, operation at wavelengths beyond about 2 μm requires that the devices be cooled to minimize thermal excitation of electrons either from the valence band or quantum well into the conduction band.

Thermal detectors, or bolometers, operate in a totally different manner[58]. Bolometers typically utilize the temperature dependence of the sensing element's electrical resistance in order to measure the power of incident electromagnetic radiation. In this way it is similar to the photoconductive detector described above, but the mechanism is fundamentally different. In a

bolometer, the energy of incident photons is converted to heat which leads to a change in resistance. When the radiation is removed, the absorptive element returns to the temperature of its thermal sink. The mechanism and sign of the resistance change depends on the material being utilized; metals, semiconductors, and superconductors can all be used as absorptive elements in bolometers. The intrinsic time constant which determines the speed of the detector is equal to the ratio of the heat capacity of the absorptive element to the thermal conductance between the absorptive element and its thermal sink[59].

Most commercial thermal infrared detectors are based on vanadium oxide (VO_X, where X is typically ~ 1.8) or amorphous silicon. Thermal detector semiconductors may be heavily doped such that conduction is by variable range hopping as described by Efros and Shklovskii[60]. Electrons hop with the absorption and emission of phonons, which gives rise to the temperature dependence of the resistance. Alternately, thermal detector semiconductors may be intrinsic or lightly doped such that the temperature dependence of the resistance depends on the creation of mobile carriers by thermal excitations across a small bandgap.

In order to compare the device studied in this chapter with commercial and previously reported detectors, it is important to first explain the commonly used photodetector figures of merit. Specific to photonic detectors, the quantum efficiency, η, is the flux of generated electron-hole pairs contributing to the photocurrent divided by the flux of incident photons. There are many mechanisms which may prevent an incident photon from contributing to the photocurrent. The photon may not be absorbed due to insufficient absorbing material thickness, or it may be reflected from the surface. Also, electron hole pairs produced near the surface of the detector

often recombine quickly due to surface defects acting as recombination centers. Converting these mechanisms to equation form, the quantum efficiency is given by

$$\eta = (1-r)\varsigma[1-\exp(-\alpha d)], \tag{3.2}$$

where r is the reflectance, ς is the fraction of electron-hole pairs that contribute to the photocurrent, α is the absorption coefficient, and d is the photodetector depth. Instead of quantum efficiency, thermal detectors have a temperature coefficient of resistance, (TCR), which is the relative change of a material's resistance with temperature. This can be positive or negative, and is given by

$$TCR = \frac{dR/dT}{R_0}, \tag{3.3}$$

where R is the resistance, T is the temperature, and R_0 is the resistance at some specified reference value.

One of the most commonly referenced figures of merit for both photonic and thermal photodetectors is the responsivity, which relates the electric current to the incident photon power. In the photonic case, recalling the definition of quantum efficiency, η, we know that a photon flux Φ gives rise to a current $I = \eta q \Phi$, where q is the electronic charge. Converting flux to power provides the relation $P = h\upsilon\Phi$, where h is Planck's constant and υ is the frequency. Taking the ratio of current to incident power, the responsivity in units of A/W is given by

$$R_I(\lambda) = \frac{I}{P} = \frac{\eta q}{h\nu} = \eta\frac{\lambda}{1.24}, \tag{3.4}$$

where λ is the wavelength of the incident light in microns. In the thermal case, responsivity is used in the form $R_I(\lambda) = \Delta I / P$ or $R_V(\lambda) = \Delta V / P$, where ΔI is the change in current measured if a voltage bias is used, ΔV is the change in voltage measured if a current bias is used, and P is the incident photon power. Because absorbed photons do not directly produce mobile charge carriers, ΔI or ΔV and hence responsivity are also a function of the bias, which must be applied in order to measure the change in resistance.

Another commonly referenced detector figure of merit for both photonic and thermal detectors is the specific detectivity, D*, which is square root of the area × bandwidth product normalized to the noise equivalent power, *NEP*:

$$D^* = \frac{\sqrt{A\Delta f}}{NEP} \tag{3.5}$$

Here the units are cm·Hz$^{1/2}$/W (also called a Jones), A is the photosensitive area, Δf is the bandwidth, and NEP is the noise equivalent power. The noise equivalent power is defined as the signal power that gives a signal to noise ratio of unity at the detector output at a given modulation frequency, wavelength, and effective noise bandwidth. *NEP* can be expressed as a function of responsivity, R, the noise bandwidth, and the noise level, X_n, in the form

$$NEP = \frac{X_n \sqrt{\Delta f}}{R_{I,V}}, \tag{3.6}$$

so that the detectivity can also be expressed in terms of the responsivity as

$$D^* = \frac{R_{I,V} \sqrt{A}}{X_n}. \tag{3.7}$$

Here X_n refers to either voltage noise, V_n in $V \cdot Hz^{-1/2}$, or current noise, I_n in $A \cdot Hz^{-1/2}$, depending on which was being measured.

There are several sources of noise that are inherent to the photodetection process, regardless of the material. Photon noise, the most fundamental source of noise, is associated with the random arrival of photons themselves. In the photonic case, photoelectron noise is associated with the fact that the photo-generation of charges is random. Each photon generates an electron-hole pair with probability η and fails to do so with probability $1-\eta$. Also in the photonic case, gain noise occurs because each photon generates a random number of carriers whose average is equal to the gain. Receiver circuit noise is present due to the various components of the circuitry. Background noise is photon noise associated with extraneous light reaching the detector. This is especially destructive to a measurement in the mid- and far-infrared ranges because of the thermal radiation emitted at these wavelengths by objects at room temperature. Also present is $1/f$ noise, which is present in almost all electronic devices and results from a variety of effects.

To summarize, photonic infrared detectors have fast response times in the nanosecond to microsecond range, are cooled during operation, and are expensive. With the exception of hot electron bolometers, hermal infrared detectors have slower response times in the millisecond range, operate at room temperature, and are inexpensive to make and operate. As will be discussed in the following sections, previous work on carbon nanotube infrared detectors have seen both photonic-like and thermal-like behavior. It will be important to have a clear picture of the microscale structure of the devices in order to really understand the mechanism and optimize the device.

3.2 Carbon Nanotubes for Infrared Detection

3.2.1 Optical Properties of Carbon Nanotubes

The optical properties of carbon nanotubes (CNTs) are due to their unique electronic structure. The electronic density of states for the π electrons in a semiconducting single wall nanotube (SWNT) has spikes called van Hove singularities, as shown in Figure 3.1.

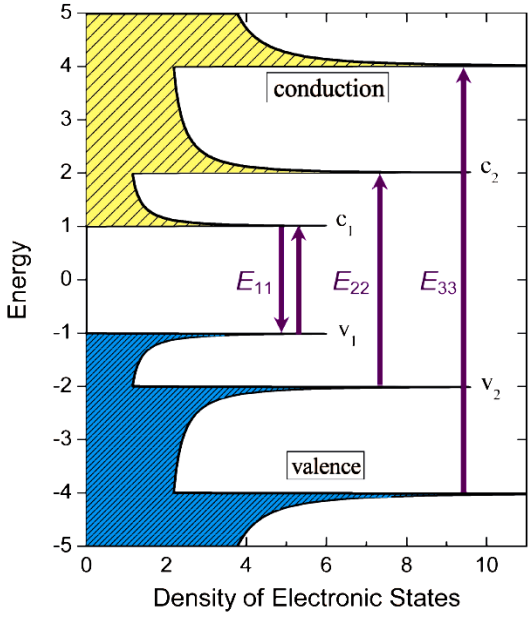

Figure 3.1: Schematic density of electronic states in a semiconducting single wall carbon nanotube. The sharp maxima are van Hove singularities. The arrows show the dominant optical transitions.

The sharp maxima are the van Hove singularities which result from confinement of the electronic states, and the indices refer to the sub-band to which they belong. Optical absorption originates from transitions E_{11}, E_{22}, etc. in Figure 3.1 so that the absorptions spectrum is very broad with several peaks as opposed to conventional 3D materials which have a sharp absorption threshold. Photo-excited electrons and holes in CNTs form strongly bound excitons with a binding energy

that decreases with increasing nanotube radius[61]. This is due to the fact that the bandgap of a CNT is approximately inversely proportional to the tube diameter. As an example, varying the tube diameter from 1 nm to 2 nm changes the SWNT band gap from ~ 0.8 eV to ~ 0.4 eV. This corresponds to photon wavelengths from 1.55 μm to 3.11 μm. It is not surprising then that CNTs, either in single-wall or multiwall (MWNT) form, show outstanding absorption in the infrared (IR) spectrum, making them promising candidates for IR detector applications[17,62–73]. In the absence of a driving force or sufficient thermal energy to separate the bound electron-hole pairs, they will eventually recombine and give their energy to the lattice in the form of heat. CNTs whose excitons are dissociated before they can relax will behave as a photoconductive photodetector, while CNTs whose excitons relax and give their energy as heat to the lattice will behave as a bolometer.

When examining the effects of illumination of CNTs, electronic excitations are not the only phenomenon to consider, however. Photo-desorption of molecules adsorbed on the CNT surface may also have a significant effect on the CNT's measured electronic resistance. Oxygen molecules which function as electron acceptors or hole donors may lower the hole concentration in p-type SWNTs and reduce conductivity. Desorption of these oxygen molecules by incident radiation would then decrease resistance, which is the same effect as photon absorption. It is important to distinguish these two effects from each other when interpreting CNT IR sensor data. One important note, however, is that the importance of oxygen desorption may be reduced in MWNT if many shells contribute to the resistance measurement but only the outermost shell is affected by oxygen adsorption/desorption. This will be discussed further in later sections.

3.2.2 Previous Reports and Motivation

There have been many attempts to fabricate and characterize IR detectors which employ CNT films[66,72,73] and individual CNTs[69–71] as the detection elements. Although promising results have been obtained, the specific detectivity, *D**, of the reported CNT IR detectors is typically several orders of magnitude lower than that of their commercial competitors. For SWNT and MWNT film IR detectors, the best reported *D** values are 4.5×10^5 and 3.3×10^6 cm·Hz$^{1/2}$/W, respectively[72,73]. These *D** are at least two orders of magnitude lower than that of the uncooled vanadium oxide (VOx) IR bolometers, which boasts D* on the order of 10^8 cm·Hz$^{1/2}$/W[74,75].

The first reported work on CNT based IR detectors was published in 2006 and utilized a suspended SWNT film[66]. At that time it was uncertain whether photo-absorption in CNTs produced excitons or free carriers. Interestingly, the authors observed no resistance change due to incident IR light on SWNT films which were supported directly by the substrate. By suspending the SWNT film, however, they were able to observe a clear, reproducible photoresponse. This alone suggests a bolometric instead of photonic response. In further support of this conclusion, they observed that the typical time constant was about 50 ms, and the response depended on dR/dT, the sign and magnitude of the change in resistance with temperature of the SWNT film. The CNT response to IR photons was then proposed to occur as follows. Absorption of IR photons by SWNTs produces excitons which undergo ultrafast relaxation. The energy is transferred to the lattice via electron-phonon interactions which increase the temperature of the film. This induces a change in resistance according to the film's TCR.

Work by Dr, Rongtao Lu and coworkers at the University of Kansas aimed to exploit the above effects in a more scalable way by partially suspending a SWNT film over periodic trenches in a Si/SiO_2 substrate[72]. They found that the change in resistance over original resistance, $\Delta R/R$, was -0.04% for SWNT on a flat substrate and -0.14% for a partially suspended film. This clearly demonstrated the importance of reducing the absorptive element's thermal link to the environment, but the specific detectivity and responsivity were still 10^3 and 10^5 times lower than commercial uncooled vanadium oxide bolometers, respectively. This led the authors to test a MWNT in the same configuration[73]. MWNT may offer several advantages over SWNT in this application. First, IR light absorption may be increased due to the higher number of shells. Additionally, the inner shells are naturally suspended with a poor thermal link to the substrate and environment. As mentioned above, this is due to the fact that radial thermal conductivity is three orders of magnitude lower than in the axial direction. Consistent with expectations, the photoresponse of MWNT film was one order of magnitude higher than SWNT. Interestingly, the effect of suspending the MWNT film was less pronounced than in the SWNT case. This is likely because the MWNT response contains contributions from inner shells which are already effectively suspended. Additionally, the difference in response time between suspended and unsuspended films was two orders of magnitude in the SWNT case, but the two were comparable in the MWNT case. This is likely because the unsuspended SWNT film response was dominated by the very slow photo-desorption process discussed above due to elimination of the bolometric response by the thermal link to the substrate. Despite these improvements, the specific detectivity and responsivity were still 10^2 and 10^4 times lower than commercial uncooled vanadium oxide bolometers, respectively, representing an improvement of one order of magnitude across the board over suspended SWNT films.

It is natural to suspect that intertube junctions in the disordered CNT films in the above studies may have a negative effect on the IR detector performance. The resistance of the junctions is unknown and difficult to control. Suppose a very simplistic model in which the total resistance of the film can be generally described by the equation $R = n \cdot R_{CNT} + (n-1) \cdot R_J$, where R is the total film resistance, R_{CNT} is the average CNT segment resistance, R_J is the intertube junction resistance, and n is an integer equal to the average number of CNT segments that the current must pass through between the electrodes. If R_{CNT} is much less than R_J then the total resistance will be dominated by the junction resistance, which is unlikely to change much with temperature. If this is the case then TCR will be very small, on the order of $\Delta R_{CNT}/R_J$. Additionally, it was observed that thermally annealing CNT films at 400 °C in vacuum better than 5×10^{-6} Torr for 90 minutes improved noise level by two orders of magnitude[76,77]. This was suspected to be due to improved intertube coupling. Since D* is inversely proportional to noise level, this is very important for CNT-based IR detector performance.

In light of the observed benefits of utilizing MWNTs due to their naturally suspended and thermally isolated inner shells and the detriments of intertube junctions, an individual MWNT IR sensor was proposed. In an individual MWNT IR sensor, intertube junctions are absent so TCR will reflect the MWNT and MWNT-metal interface only. Additionally, noise will be reduced due to the lack of junctions of questionable quality. Finally, inner tubes will be naturally suspended, so no complicated device fabrication steps to suspend the MWNT above the underlying substrate will be necessary. So far very little has been reported on individual CNT IR sensors, likely because of the low responsivity of a single CNT[65,70]. As will be discussed below, the details of the device configuration and electrical contact are critical to device performance, which could explain the small photoresponse in these previously reported individual CNT devices.

3.3 Individual Carbon Nanotube Infrared Detector Studies

3.3.1 Device Fabrication and Geometry

MWNTs grown by chemical vapor deposition with diameters in the range of 40-60 nm were deposited on silicon substrates with 100 nm thermally grown SiO_2. Two Ti/Au (20/60 nm) electrodes were fabricated onto the selected individual MWNT using electron beam lithography (EBL) followed by electron beam evaporation and lift off. The electrodes were found to make a Schottky contact to the MWNT. The position of electrodes was carefully controlled during the EBL so that one electrode covered one end of the MWNT while the other electrode covered only the MWNT sidewall. Two types of control MWNT devices were fabricated: one with Ohmic Pd electrodes and one with Schottky Ti/Au electrodes. In each control device both electrodes covered the sidewall of the MWNT without any metal contact to the MWNT end. In addition, MWNT films of 200 nm thickness fabricated from the same batch of the MWNTs were prepared for comparison[73,77]. The samples were annealed at 400 °C in vacuum better than 5×10^{-6} Torr before measurements to improve the electrode contact[77].

Schematics of the asymmetric Schottky device are shown below in Figure 3.2(a).

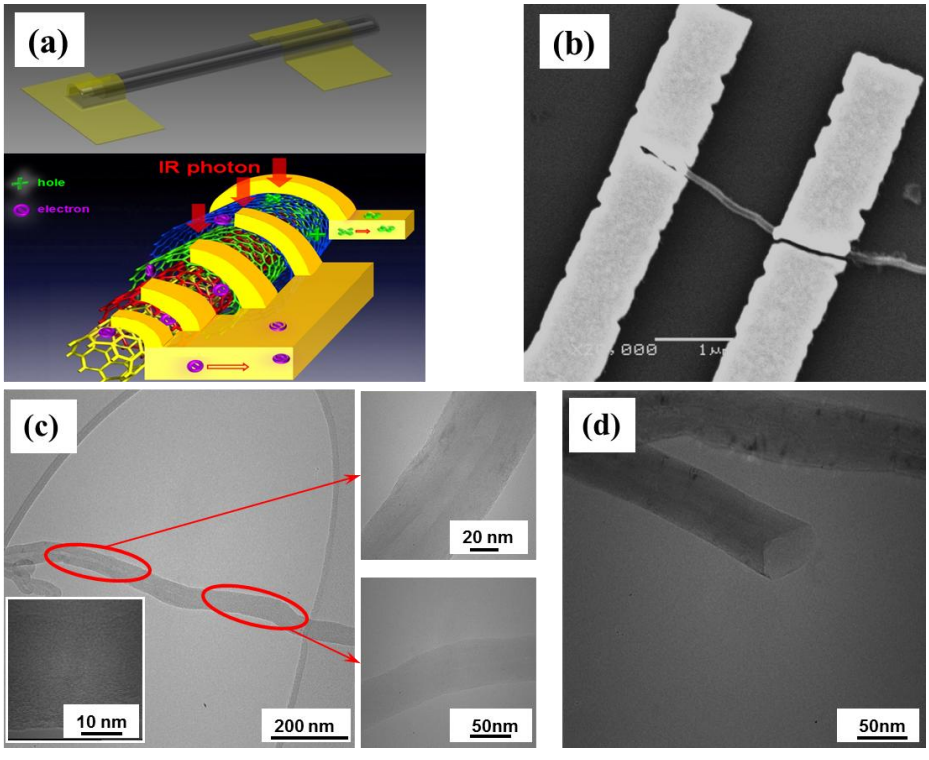

Figure 3.2: (a) 3 dimensional view and diagram of individual MWNT with asymmetric electrodes. (b) Scanning electron micrograph of an individual MWNT device with the described geometry. (c) Typical transmission electron micrograph of a MWNT with diameter of 50-60nm. (d) TEM image of MWNT showing the open end.

This asymmetric Schottky contact configuration is essential for the operation of this device. First, the photocurrent generated at the two contacts will not completely cancel each other, as follows. Because electrical and thermal transport is hindered in the radial direction compared to the axial direction[78,79], the electrode on the end of the MWNT may be able to make contact to and collect photo-generated carriers from the inner shells while the electrode on the sidewall will primarily collect photo-generated carriers from only the outermost layer or few layers. Second, because the contact is not Ohmic, the thermal link between the MWNT detector element and the electrodes will be reduced. This may result in an elevated temperature within the MWNT with Schottky contacts compared to that with Ohmic contacts. This could lead to enhanced photo-

generation of free carriers if the added thermal energy exceeds the exciton binding energy, which can be as small as few to few tens of meV in the MWNT with large diameters[80]. A negligible photoresponse was obtained on the control devices with symmetric Pd and Ti/Au electrodes. This may be attributed to the efficient thermal links by the large Ohmic contacts although the inner CNT shells are naturally suspended. These points further highlight the importance of a device's microstructure, particularly the electrode configuration and material.

A scanning electron microscopy (SEM) image of a representative MWNT photodetector is shown in Figure 3.2(b). The spacing between the electrodes is 1.3 μm and the diameter of this particular MWNT is approximately 60 nm. The active detection area is therefore defined as 1.3 μm × 60 nm. Notice that the left end of the MWNT is covered by the electrode, which may enable the metal electrode to provide electrical contact to all shells throughout the entire MWNT's cross-section. Figure 3.2(c) shows transmission electron microscopy (TEM) images of a similar MWNT. The inner shells can be clearly identified in the high resolution TEM image [bottom left inset of Figure 3.2(c)] and the shell number is estimated to be between 60 and 70. The diameter of the MWNTs is typically in the range of 50 - 60 nm. In addition, some segments of the MWNT have a bamboo-like structure[81] with a hollow center with diameter in the range of 10-15 nm [Figure 3.2(c), upper blow-up] while in other parts the hollow center becomes negligible [Figure 3.2(b), lower blow-up]. Figure 3.2(d) shows another TEM image in which the end of the MWNT can be clearly identified. This suggests that direct contact to the inner shells by an electrode positioned over the end is indeed possible.

3.3.2 Photoresponse and I-V Measurements

Figure 3.3(a) compares the normalized resistance (R) vs. temperature (T) curves in semi-

log scale for individual MWNT with asymmetric Ti/Au electrode (blue), individual MWNT with symmetric Pd electrodes (black), and MWNT film (red). The individual MWNT with asymmetric Ti/Au electrodes shows much a stronger temperature dependence as compared to the other two kinds of samples. In fact, the R-T curves of the MWNT film and individual MWNT with Pd electrodes almost coincide over the temperature range of 77 K to room temperature, as shown in a closer view in the inset of Figure 3.3(a) with a linear scale. This is not surprising since larger diameter MWNTs have smaller band gaps, as mentioned above, making their behavior less susceptible to temperature than a larger band-gap semiconductor. Additionally, the connection at the intertube junctions seems to be independent of temperature, resulting in similar normalized R-T curves on these two kinds of samples. The much steeper R-T curve for the individual MWNT with asymmetric Schottky contacts may be attributed to a dynamic contribution from the Schottky contacts in the form of a contact barrier height which is comparable to the thermal energy in this temperature range.

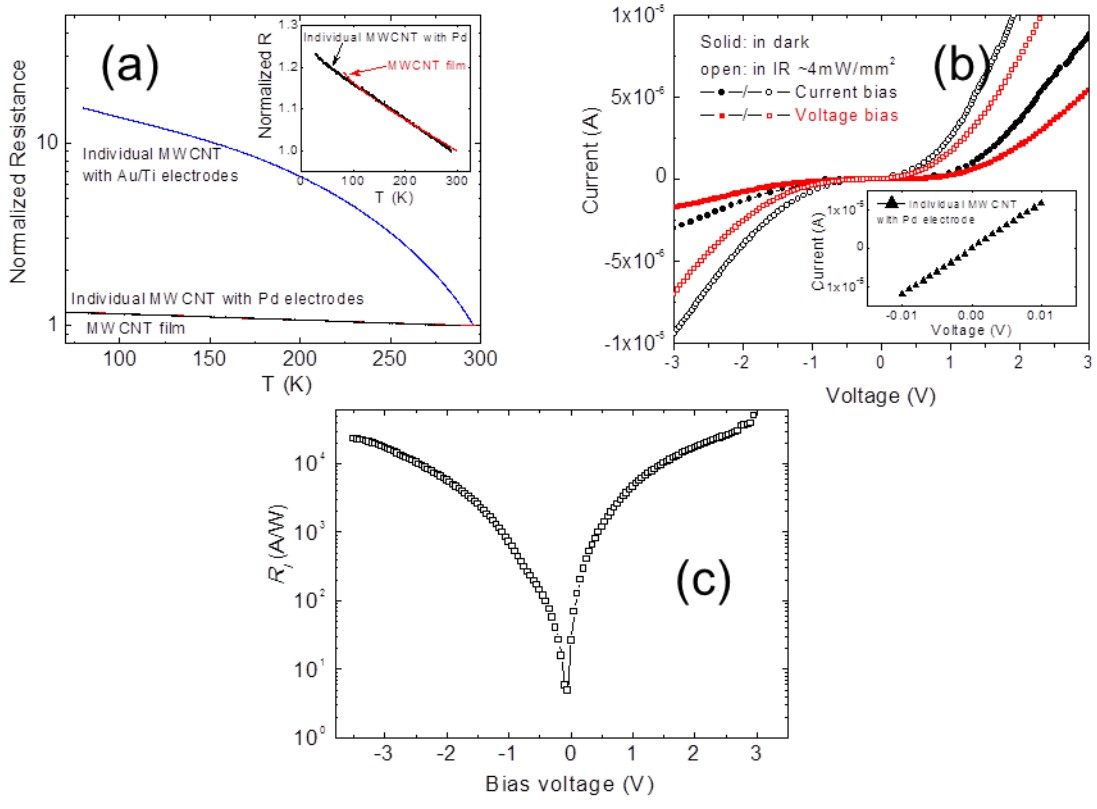

Figure 3.3: (a) Normalized R-T curves of a typical individual MWNT with asymmetric Au/Ti electrodes biased at 5nA, MWNT with symmetric Pd electrodes biased at 0.1μA, and MWNT film biased at 1μA, separately. The R-T curves of the latter two are shown in linear scale in the inset. (b) Comparison of current biased and voltage biased curves of an individual MWNT. Inset shows V-I curve of individual MWNT with symmetric Pd contacts. (c) Current responsivity versus bias voltage in 4mW/mm^2 IR radiation calculated from (b).

The TCR value calculated is in the range of -1.6%/K to -3.9%/K among a group of samples measured at room temperature, which is considerably larger than the TCR of ~ -0.1%/K for individual MWNTs with Pd electrodes and ~ -0.08%/K for MWNT films at the same temperature.

Figure 3.3(b) compares the current (or voltage) biased I-V (or V-I) curves, respectively, for the same MWNT sample shown in Figure 3.2(b) in the dark and under IR irradiation with a wavelength range of 1.1 - 1.3 μm and an intensity of 4 mW/mm^2. The I-V (and V-I) curves are

nonlinear, confirming the detector is a Schottky device. Clear IR responses have been observed in both voltage and current biased cases with no qualitative differences. The mechanism of the IR response is thought to be due to photo-absorption and exciton formation near the Schottky contacts followed by exciton dissociation due to the electric field present near the MWNT – electrode interface leading to a photocurrent. Because one electrode contacts only the outer most shell or few shells and the other electrode contacts the inner shells, the photocurrent generated at each contact will not cancel out. This is the most important distinction between this and previously published work.

In order to compare this result with the previously reported photoresponse of individual MWNTs, the absolute value of current responsivity R_I in the individual MWNT with asymmetric Schottky contacts was calculated from the voltage biased V-I curves in Figure 3.3(b) and plotted in Figure 3.3(c). This figure represents a significantly enhanced R_I on these devices. For example, R_I of 2-4$\times 10^4$ A/W at +/– 3V bias is more than three orders of magnitude larger than the 23 A/W obtained on an individual MWNT with symmetric Schottky contacts[70]. We also note that we observed a negligible R_I on the control samples with both Ti/Au electrodes on the sidewall under the same experimental conditions. This is anticipated since both contacts were in the IR beam spot, and the photocurrent generated by IR absorption would cancel out in the symmetric contact geometry. In addition, negligible photoresponse was observed on the MWNT samples with two symmetric Pd Ohmic contacts under the same IR light, as shown in the inset of Figure 3.3(b). This device is expected to behave as a bolometer due to the lack of a strong electric field to dissociate the exciton. The linear V-I curves indicate a good Ohmic electrical contacts provided by the Pd electrodes. The undetectable photoresponse in this kind of MWNT bolometer then (the dark and illuminated curves overlap on each other) is most probably due to

the efficient thermal link from the detector to the environment through the Ohmic metal contacts as well as lack of electrical access to the inner shells.

While more systematic studies are necessary to pinpoint the exact mechanism responsible for the much enhanced R_I obtained on the individual MWNT with asymmetric Schottky contacts, we postulate that several unique features which combined together may explain the improved performance. Some features have been mentioned above, and all are summarized here. First, the Schottky contact on the end of the MWNT may electrically contact the inner CNT shells provide a pathway for collecting photocurrent from essentially all shells on one end of the device. On the other end of the device photocurrent will be collected from only the outer most shell or few shells. This way the total photocurrent generated will not cancel out if the entire device is inside the beam spot. Considering that all inner CNT shells may absorb light with a similar efficiency, the photocurrent collected at the MWNT end should increase with the number of inner CNT shells up to an optimal MWNT diameter (or number of inner shells) for a complete light absorption, which is on the order of 50-100 nm[82]. Additionally, the Schottky contacts have a much reduced thermal link compared to Ohmic contacts. This may result in considerably enhanced detector element temperature which may exceed the exciton binding energy in large diameter CNTs and consequently lead to a thermally assisted generation of photocurrent. While accurate measurement of the individual MWNT temperature remains challenging, some estimation that supports this argument may be extracted from the transport property of individual MWNT and will be discussed in the following.

Figure 3.4(a) depicts the temporal dynamic resistance change of an individual MWNT with asymmetric Schottky contacts under modulated IR radiation at room temperature. The MWNT was current biased at 10 μA with an IR power intensity of ~3.5 mW/mm^2 and

modulation frequency of 10 Hz. The measured dynamic resistance change ratio $\Delta R/R_0$ (R_0 is the resistance in dark and ΔR is the magnitude of the resistance change under IR radiation) is about 40% for this individual MWNT, which is more than 60 times larger than the $\Delta R/R_0 \sim 0.6\%$ obtained on a MWNT film bolometer under comparable IR radiation[73].

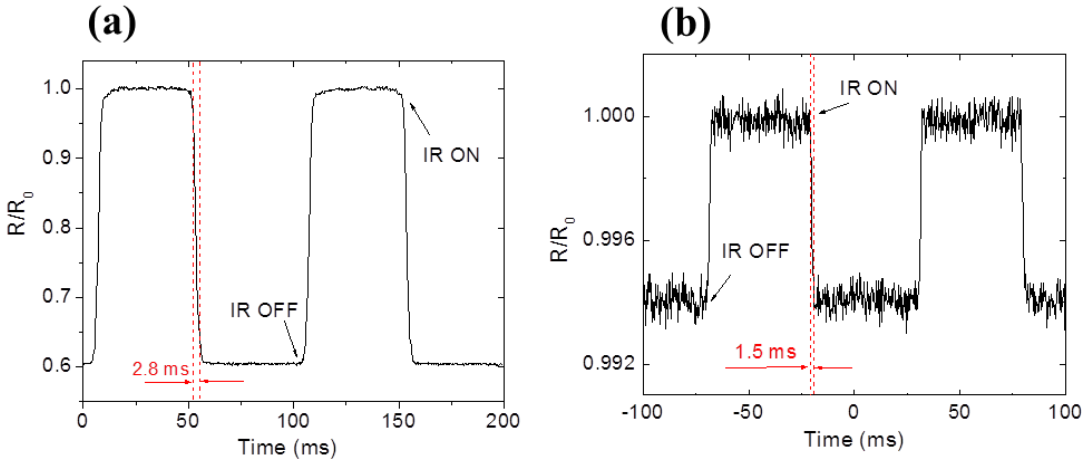

Figure 3.4: Temporal IR Photoresponse of an individual MWNT under ~3.5 mW/mm^2 IR radiation biased at 10 μA, f = 10 Hz. (b) IR photoresponse of MWNT film under ~3mW/mm^2 biased at 2 mA, f = 10 Hz. The marked response time is measured from 90% to 10% of the total change.

Considering that the $\Delta R/R_0$ in the film case is a thermal effect, the maximum temperature rise of a MWNT can be estimated to be about 8 K using the TCR ~ -0.08%/K at room temperature for the MWNT film[77]. Similarly, a maximum temperature rise in the individual MWNT with asymmetric Schottky contacts of around 10 K can be estimated using the observed resistance change and the TCR ~ -3.9%/K at room temperature. Since the exciton binding energy in the MWNT of large diameter could be as small as few meV, which corresponds to less than 100 K, the 10 K temperature rise may provide nontrivial thermal energy to assist in exciton dissociation. The observed response time is about 2.8 ms for the individual MWNT as measured from 90% to

10% magnitude change, which is slightly larger yet comparable to the response time measured on MWNT films of around 1.5 ms[73]. The response times in both individual and film MWNT samples are more than one order of magnitude shorter than that of suspended SWNT films[66,72], where film suspension is necessary to reduce the thermal link to the environment in order to achieve non-negligible responsivity.

3.3.3 Specific Detectivity Calculations

The *D** values are plotted as function of bias current density in Figure 3.5(a) for individual MWNTs with asymmetric Schottky contacts and MWNT films. Since the MWNT film is not dense, the current density estimated using the nominal film thickness ~ 200 nm may have a large uncertainty. The IR light was fixed at 0.3 mW/mm^2 intensity and 10 Hz modulation frequency for both samples. A much narrower current density range was applied to the film since a saturation of *D** in the MWNT film has been observed in this range already. The saturation of *D** in MWNT films [inset of Figure 3.5(a)] may be attributed to self-heating and a decrease in TCR at higher bias currents for a bolometer[73]. In addition, deviation of noise voltage from an ideal 1/f character was not rare[83,84], and enhanced noise was observed in the MWNT film at higher current density possibly due to the overheating of intertube junctions. The kind of *D** vs. current density trend observed in the MWNT film has been reported in conventional VO_X film bolometers in which the TCR value decreases at higher bias current due to the power dissipation of the DC electrical bias[74]. In contrast, no D* saturation was observed in the case of the individual MWNT with asymmetric Schottky contacts within a much wider bias current range, as seen in Figure 3.5(a). This suggests less power dissipation which may be attributed to nearly ballistic charge transport along the CNT shells.

The maximum D^* is about 1.4×10^9 cm·Hz$^{1/2}$/W at 4×10^5A/cm^2, the maximum current density applied in this experiment (higher current density was avoided to protect the sample), which is considerably higher than that of most conventional VOx uncooled bolometers[74,75]. Further, Figure 3.5(a) reveals that the individual MWNT can work in a very wide current density range, up to at least 10^5 A/cm^2, which is about two orders of magnitude higher than the upper limit of ~ 3000 A/cm^2 for MWCNT film before D^* saturates.

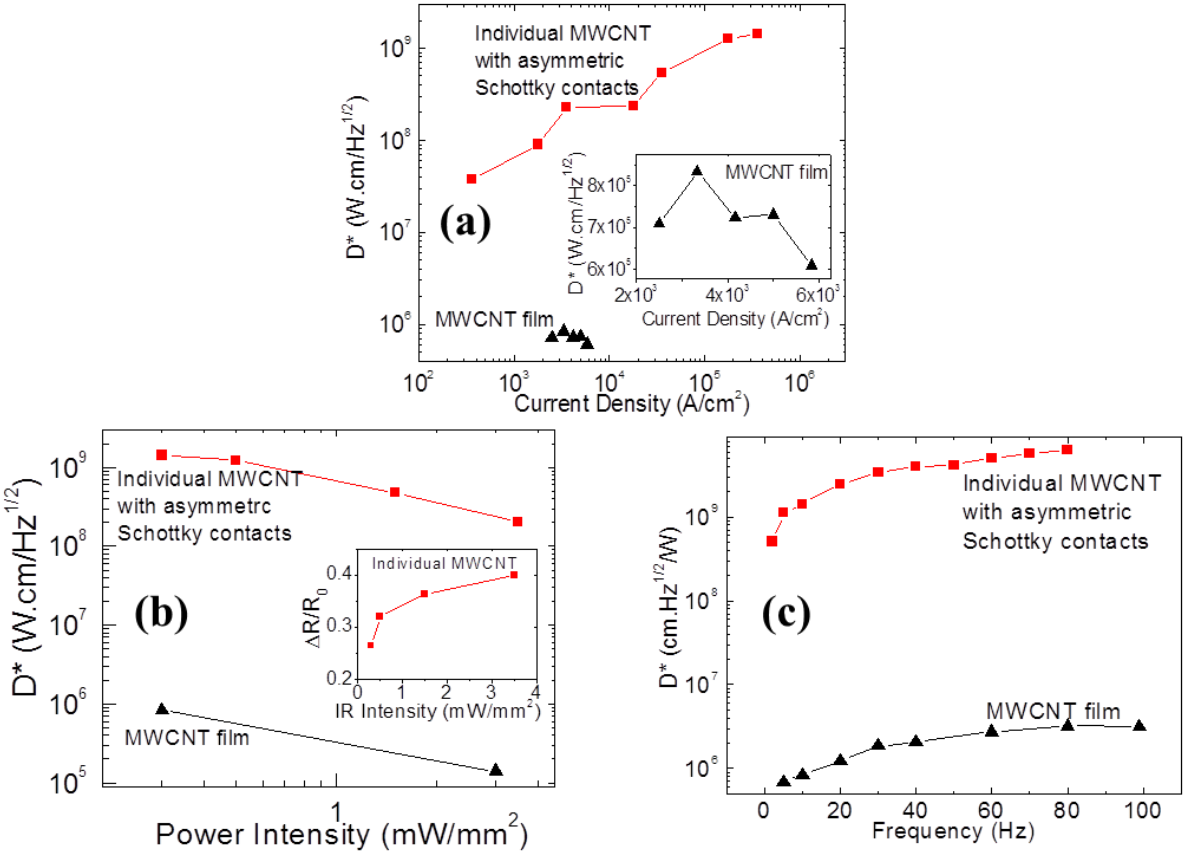

Figure 3.5: D* versus bias current density comparisons for individual MWNT with asymmetric Schottky contacts and MWNT film (blown up for clarity in the inset). (b) D* versus IR power intensity of the same types of devices. Inset shows the resistance response versus incident power in the individual MWNT. (c) D* as a function of modulation frequency at a constant IR power intensity (0.3 mW/mm^2) and current bias (10 μA and 2 mA for individual MWNT and film, respectively).

Figure 3.5(b) shows a comparison of D^* values for the MWNT film and individual MWNT with asymmetric Schottky contacts as function of incident IR power intensity. Both samples were biased at the current density corresponding to their maximum D^* obtained in Figure 3.5(a). A similar trend of monotonic decreasing D^* with IR light power density can be observed on both samples. This trend is induced by the nonlinear variation of $\Delta R/R_0$ with IR power intensity, as shown in the inset of Figure 3.5(b) for the individual MWNTs with asymmetric Schottky contacts, which results in decreasing responsivity with increasing IR power intensity. Consequently, D^* decreases since the noise voltage remains almost constant with increasing IR power intensity. This variation trend is qualitatively consistent with the reported trend for SWNT bundle microwave bolometers where R_V decreases by two orders of magnitude while the incident microwave power intensity increases by four orders of magnitude[85].

It is important to note that the nonlinear increase of $\Delta R/R_0$ with power intensity is not expected for a purely photonic response as the photo-carrier generation should be linearly proportional to the number of the incident photons, which has been reported by Xi *et al* in individual CNTs with natural Schottky symmetry under near-IR illumination of 1.9-3.9 W/mm[63,70]. This is further evidence that the observed photoresponse in the individual MWNT with asymmetric Schottky contacts may not be a conventional photonic response. Instead it is most probably a photonic effect combined with thermally assisted exciton dissociation.

The dependence of D^* on modulation frequency for both individual and film MWNT samples are compared in Figure 3.5(c). The D^* increases monotonically with increasing frequency for both kinds of samples. This increase is attributed to the decrease in1/f type noise voltage with increasing frequency[76,77,83]. Moreover, at a fixed bias current, the 1/f type noise voltage will saturate to the thermal noise when the frequency is high enough, thus the D^*

saturates accordingly since the decrease of R_V with frequency is very small. For individual MWNT, D^* almost saturates at 80 Hz with a maximum ~ 6.2×10^9cm·Hz$^{1/2}$/W, which is more than two orders of magnitude higher than the best saturated D^* in MWNT film. In addition, this D^* value is about one order of magnitude higher than that of the commercial VO_X uncooled IR detectors ~ 10^8 cm·Hz$^{1/2}$/W[14] and five times of the state-of-art doped VO_X thin film bolometer at D^*~1.2×10^9 cm·Hz$^{1/2}$/W[75]. This result demonstrates that the individual MWNT with asymmetric Schottky contacts is competitive for practical applications of uncooled IR detectors.

3.3.4 Conclusion

In conclusion, a significantly enhanced detectivity of up to 6.2×10^9 cm·Hz$^{1/2}$/W has been obtained on individual MWNT IR photodetectors at room temperature, making CNT superior to conventional uncooled VO_X IR detectors. The novelty of these detectors is in the adopted asymmetric Schottky contacts on the MWNT, which enables highly efficient collection of photocurrent from the inner CNT shells at one end of the device, preventing photocurrent cancellation at the electrodes. This yields a significantly enhanced photoresponsivity of up to 10^4 A/W, which is three orders of magnitude larger than that previously obtained on CNT Schottky devices. In addition, thermally assisted exciton dissociation to mobile charge carriers facilitated by the reduced thermal link at the Schottky contacts to the environment may provide a further contribution to the photocurrent. The demonstrated performance makes individual MWNT photodetectors competitive for practical uncooled IR detections.

Chapter 4

Correlation of Defect Structure and Diffusion in Transferred Graphene Films Grown by Chemical Vapor Deposition

4.1 Introduction to Graphene

As mentioned above, graphene was first discovered experimentally in 2004, but its story began long before. Theoretically, graphene has been studied since the 1940's as a way to describe other carbon-based materials like graphite[86,87], which was important at the time for use in nuclear reactors. The term "graphene" was first coined in 1962 by Hanns-Peter Boehm in regard to thin carbon foils produced from graphite oxide[88]. In the 1970's it became known that graphene could be grown on solid substrates either by the thermal decomposition of carbides[89] or epitaxially on metal films[90]. However, graphene was of little interest until the direct observation of isolated graphene in 2004, sparking exponentially growing interest. Perhaps the reason it took so long for isolated graphene to be experimentally discovered was because, by and large, people didn't expect it to exist. Also coming into play could be the fact that there were no known experimental tools available to search for one atom thick flakes in a large graphitic debris field.

Graphene is the name given to an atomic monolayer of sp^2-bonded carbon atoms arranged in a two dimensional hexagonal lattice. Each carbon atom hybridizes the 2s, $2p_x$, and $2p_y$ orbitals to contribute to the structure and stability of the sheet via covalent bonds. The remaining p-orbital, p_z, lies perpendicular to the plane of the sheet and overlaps with the other half-filled p_z orbitals of the neighboring atoms to form the π^* (conduction) and π (valence) bands. As seen in Figure 4.1(a), the lattice can be viewed as two interpenetrating triangular sublattices.

The atoms of one sublattice are located at the center of triangles defined by the atoms of the other sublattice. The carbon to carbon inter-atomic length is 1.42Å. The unit cell, denoted by the dashed box, consists of two atoms, A and B, and is invariant under a 120° rotation about any lattice site.

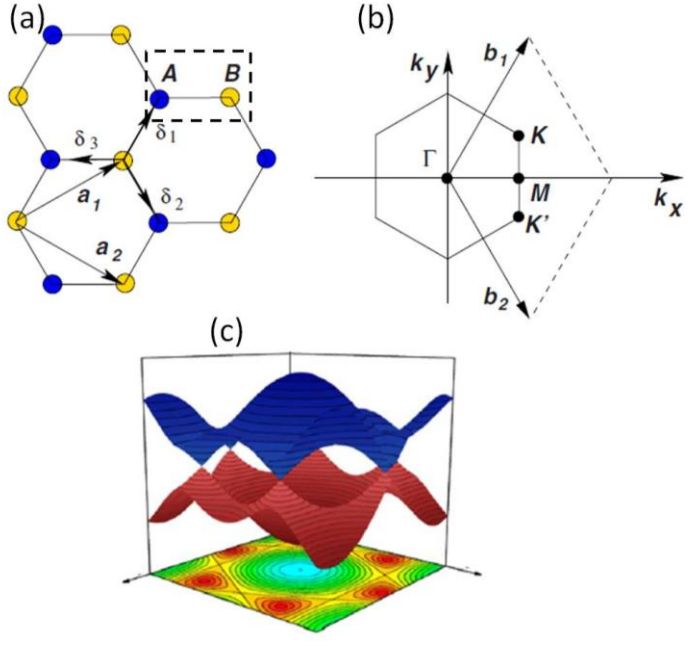

Figure 4.1: (a) Lattice structure of graphene, depicted as two interpenetrating triangle sub-lattices (denoted as yellow and blue circles) with lattice vectors and unit cell marked. δ_i are the nearest neighbors. (b) The corresponding Brillouin zone and reciprocal lattice vectors. *K* and *K'* are the Dirac points. (c) Band structure of graphene. The valence and conduction bands touch at the Dirac points.

The lattice vectors are given by

$$\vec{a}_1 = \frac{a}{2}\left(\sqrt{3},1\right), \vec{a}_2 = \frac{a}{2}\left(\sqrt{3},-1\right) \tag{4.1}$$

where a = 0.246 nm is the lattice constant. The reciprocal lattice, depicted in Figure 4.1 (b), is also hexagonal and has lattice vectors given by

$$\vec{b}_1 = \frac{2\pi}{a}\left(\frac{1}{\sqrt{3}},1\right), \vec{b}_2 = \frac{2\pi}{a}\left(\frac{1}{\sqrt{3}},-1\right) \tag{4.2}$$

with lattice constant $4\pi/\sqrt{3}a$. There are two non-equivalent points in the first Brillouin zone labeled *K* and *K'*. The other four corners are related by reciprocal lattice vectors and do not represent distinct states.

The band structure of graphene's π electrons was first determined using the tight binding approximation in 1947[86]. By using a linear combination of Bloch wave functions for sub-lattices A and B and assuming each atom has three nearest neighbors, the energy-momentum dispersion relation can be found. As seen in Figure 4.1(c), the conduction and valence bands meet each other at the *K* and *K'* points to produce conical shaped valleys. The Fermi level is located at the apex of these cones, called the Dirac point, where the electrons and holes are degenerate. This band structure makes graphene a zero band gap semiconductor and introduces some interesting physics which will be discussed later. Since there are two atoms (and hence two electrons) per unit cell, the valence band is completely full and the conduction band is completely empty at absolute zero. In the low energy regime, i.e. in the vicinity of the *K* and *K'* points, the energy-momentum dispersion relation is linear, and charge carriers appear to be zero rest mass relativistic particles with an effective "speed of light" $v_F \approx 10^6$ m/s. These quasi-particles are referred to as massless Dirac fermions[91].

Interestingly, it was thought for many years that a single layer of graphene could not exist in freestanding form. More than 70 years ago Peierls[92] and Landau[93] concluded that long range two-dimensional crystalline order was impossible, and strictly 2D crystals would be thermodynamically unstable. Atomic monolayers as we knew them only existed as a part of a larger 3D structure, typically grown epitaxially on crystals with matching lattice constants. This of course all changed in 2004 with the experimental discovery of graphene[8]. The existence of these one-atom thick crystals, however, does not disprove the decades old theories. It has been

observed experimentally that graphene warps gently in three dimensions on the scale of approximately 10 nm[94].This suppresses the thermal fluctuations that otherwise were thought to lead to atomic displacements on the order of inter-atomic distances which would make graphene unstable.

4.2 Motivation and Methodology

4.2.1 Graphene in Transparent Electronics

Thanks to the ability to acquire very high quality samples via mechanical exfoliation of graphite[95], many new and/or interesting physical phenomena have been observed in graphene including but not limited to Shubnikov–de Haas oscillations[8,96], ballistic transport[97], room temperature quantum Hall effect[98], fractional quantum Hall effect[99], the Klein paradox[100], and the breakdown of the Born-Oppenheimer approximation[101]. Nearly all of the most exciting and renowned observations of graphene revolve around its unique electronic transport properties. While graphene has proved itself as an exceptional playground in which to probe interesting physical phenomena, it is also emerging as an excellent candidate to improve the quality, affordability, and speed of many modern electronic devices.

More details of exfoliated graphene flake device physics and fabrication will be explored in Chapter 5. The focus of this chapter is on the use of graphene in transparent commercial electronics. Graphene could be used as a large scale transparent conductor or an array of components on a chip. Taking transparent conductors as an example, the need for flexible, highly transparent, low sheet resistance conductors has increased in recent years with the development of technologies such as touch screens, flexible displays, printable electronics, thin film photovoltaics, and more. The current industry standard transparent conductor, indium tin oxide

(ITO), which has transparencies of > 90% at a wavelength of 550nm, sheet resistances of 10-30 Ω/□, and a favorable work function for hole collection in many organic and hybrid solar cells. ITO, however, is not ideal because of the limited supply and rising cost of indium, costly high vacuum deposition techniques, and the difficulty of producing flexible or curved ITO surfaces with acceptable conductivity. Additionally, indium is known to diffuse through active layers of organic light emitting diodes and degrade the performance. Graphene is a highly desirable replacement for ITO because it is a flexible zero bandgap semiconductor with extremely high carrier mobilities which absorbs only 2.3% of visible light per sheet[102]. Additionally, graphene can be doped chemically to levels of 10^{12} cm^{-2} while maintaining mobilities on the order of 10^5 $cm^2/V \cdot s$[11,20]. While the sheet resistance of a single layer of graphene can be rather high compared to ITO, additional layers reduce the sheet resistance according to the following relationship[103].

$$R_{sh} = \frac{1}{q\mu N_i N} = \frac{62.4\Omega}{N} \tag{4.3}$$

Here N is the number of graphene layers, N_i is the carrier concentration, q is the electron charge, and μ is the mobility. This equation uses $N_i = 10^{12}$ cm^{-2} and $\mu = 10^5$ $cm^2/V \cdot s$, which is optimistic yet still gives an idea of the type of sheet resistance that should be attainable in an optimized fabrication scheme.

The method of mechanical exfoliation, which is used to produce high quality graphene flakes from pyrolytic graphite and will be discussed in Chapter 5, produces a random debris field of graphitic flakes. Careful hunting allows one to identify a small number of monolayer graphene flakes which are typically on the order of < 1 – 100 μm in size. While the quality and electronic properties of these flakes are excellent, this is not a scalable process for producing the large area graphene films which are needed for the proposed applications. Chemical routes to exfoliate

graphene from graphite have not met much success because of graphite's hydrophobic surface that will not disperse unassisted in organic solvents. One alternative is to synthesize graphite oxide (GO) sheets by oxidizing graphite with strong acids followed by intercalation and exfoliation in water. After the resulting GO flakes are deposited on a substrate, they can be reduced to produce graphene[104]. Unfortunately this process results in some irreversibly damages areas which behave as electron traps and severely degrade the sheet resistance[105]. Graphene films produced this way can have in the range of 90% transparency at 550 nm wavelength and 5 kΩ/□ sheet resistance[106].

A much better approach than dispersing graphene or GO flakes to produce a continuous film is the large area growth of graphene. Several methods to grow large scale graphene films have been developed including vacuum decomposition of SiC[107,108] and chemical vapor deposition (CVD) on metal films such as nickel[109,110], copper[111,112], and other transition metals[113,114]. Of these methods, CVD on copper is particularly promising because it yields films which are predominantly monolayer, consist of comparatively large grains, and are easily transferrable to an arbitrary substrate[115]. The last point is especially critical because graphene films on a metal substrate cannot be used as-is for any electronic application. Despite the great practical promise, the mobility of graphene grown by CVD on copper is typically 1-2 orders of magnitude lower than substrate-supported exfoliated graphene. Much work has been done to increase the grain size, and grains as large as 0.5 mm have been realized[116], but so far no result has been able to approach the mobility of exfoliated graphene. Graphene produced by CVD on either copper or nickel and transferred to another substrate can typically achieve up to 80-90% transparency at 550 nm wavelength and several 10^2 Ω/□[109,110,117]. If CVD grown graphene is to become a viable solution for transparent electronics, its electronic quality must be greatly

improved. This type of improvement cannot be achieved without first acquiring a solid understanding of the microstructure of the grown and transferred graphene films.

4.2.2 Large Area Growth of Graphene by Chemical Vapor Deposition

Growth of graphene on copper by CVD is certainly a deep research field, many of the details of which are beyond the scope of this document. Therefore only a brief summary of the mechanism and process will be given here[118]. Generally, graphene is grown on copper by the decomposition of hydrocarbon gas over a copper substrate that is held at ~ 1000 °C. Copper foils with thicknesses from 25 – 50 μm and a low pressure (0.5 – 50 Torr) or atmospheric pressure mixture of methane and hydrogen gases are normally used. Graphene grains nucleate on the surface of copper, grow in size over time, and eventually coalesce with neighboring grains to form a continuous layer. After this point, further exposure to the carbon precursor does not result in growth of additional layers, making it a self-limiting process. The weak interaction between graphene and copper allow flakes to expand over copper grain boundaries without significant structural disruption.

Graphene grown by CVD on copper can be transferred to an arbitrary substrate by a method which will be described below. Transferred graphene films will contain three different types of boundaries which vary in origin and feature size. The first and most fundamental are grain boundaries which occur when grains of different crystal orientation coalesce during growth, as described above. These domains vary greatly in size from $< 10^2$ nm to $> 10^2$ μm depending on the growth conditions. The second are wrinkles due to the difference in thermal expansion coefficient of graphene and copper[111]. Graphene has a large negative thermal expansion coefficient of -6×10^{-6}/K at 27 °C[119] while copper has a large positive thermal

expansion coefficient of $24 \times 10^{-6}/K$[119]. This suggests that there will be significant shrinkage of copper relative to graphene with cooling. This induces mechanical stress on graphene resulting in the formation of wrinkles. These wrinkles may span multiple graphene grains and define closed domains which are typically a few to a few tens of microns in size. The third and least fundamental type of boundary are creases formed during the graphene film transfer process. These large features are visible by optical microscopy and do not necessary form closed domains. Of these three types of boundaries, only the effect of grain boundaries on electronic transport properties has received much attention[120–122]. All three types of boundaries, however, may have a deleterious effect and therefore must be characterized and understood.

4.2.3 Methodology

In this work graphene grown by CVD on copper and transferred to an insulating substrate using standard techniques is studied. Raman spectroscopy, a very powerful technique to study graphene, is used to characterize the graphene film and boundaries in predetermined areas of interest. Because of the complications induced by the fabrication steps necessary to etch and deposit metal electrodes as well as the influence of electrode material and contact quality on electronic measurements, an optical technique is used to measure carrier diffusion. Carrier diffusion is related to mobility through the Einstein relation, which for graphene is

$$D = \frac{\mu k_B T}{2q}, \tag{4.4}$$

where D is the diffusion coefficient, μ is the mobility, k_B is Boltzmann constant, T is the temperature, and q is the electronic charge. Using these techniques together, the nature of the boundaries and their influence on carrier diffusion can be correlated on the transferred film.

4.3 Defect Characterization by Raman Spectroscopy

Graphene sheets were grown on a 25 micron thick copper foil (Alfa Aesar, item No.13382) by CVD at 1000 ^{o}C following previously published procedures[111,123]. A mixture of CH_4 (35 sccm) and H_2 (2 sccm) was used for the gas precursors. The Cu substrate was placed inside a fused silica furnace tube and heated to 1000 ^{o}C under H_2 flow. Growth of graphene was initiated by introduction of CH_4 after the growth temperature was reached. The growth time was 30 minutes. In order to transfer the CVD-grown graphene films onto the desired substrate, poly-methyl methacrylate (PMMA) was first spin-coated on the surface of the as-grown graphene on copper. The film was then placed into iron chloride solution (0.1g/mL) to remove the copper foil, rinsed in DI water three times, and allowed to soak in 2L fresh DI water overnight to further remove remaining iron and copper residuals. The target substrate (BK7 glass) was then immersed into the DI water and used to lift the graphene film from the liquid. The sample was placed into an oven in air at 80 ^{o}C for one hour for drying. PMMA was then re-deposited and allowed to cure slowly overnight. This second PMMA step helps to reduce cracking in the graphene. Finally, the PMMA was removed with hot acetone.

Alignment marks were patterned using electron beam lithography (EBL) on top of the graphene film in order to reproducibly locate specific features. Following liftoff, the graphene was cleaned by thermal annealing in flowing hydrogen (500 sccm) and argon (486 sccm) gas at 400°C for 15 minutes in order to remove polymer residue from the film transfer and EBL processes. Regions of interest were first identified optically. Atomic force microscopy and confocal Raman mapping were utilized in order to further characterize the film (Witec Alpha 300) The Raman system utilized a 488 nm excitation laser with an approximately 330nm beam spot, and spectra were taken at a rate of 8 points per micron. Transient absorption microscopy

measurements were used to determine the effect of the defect structures on the charge carrier transport.

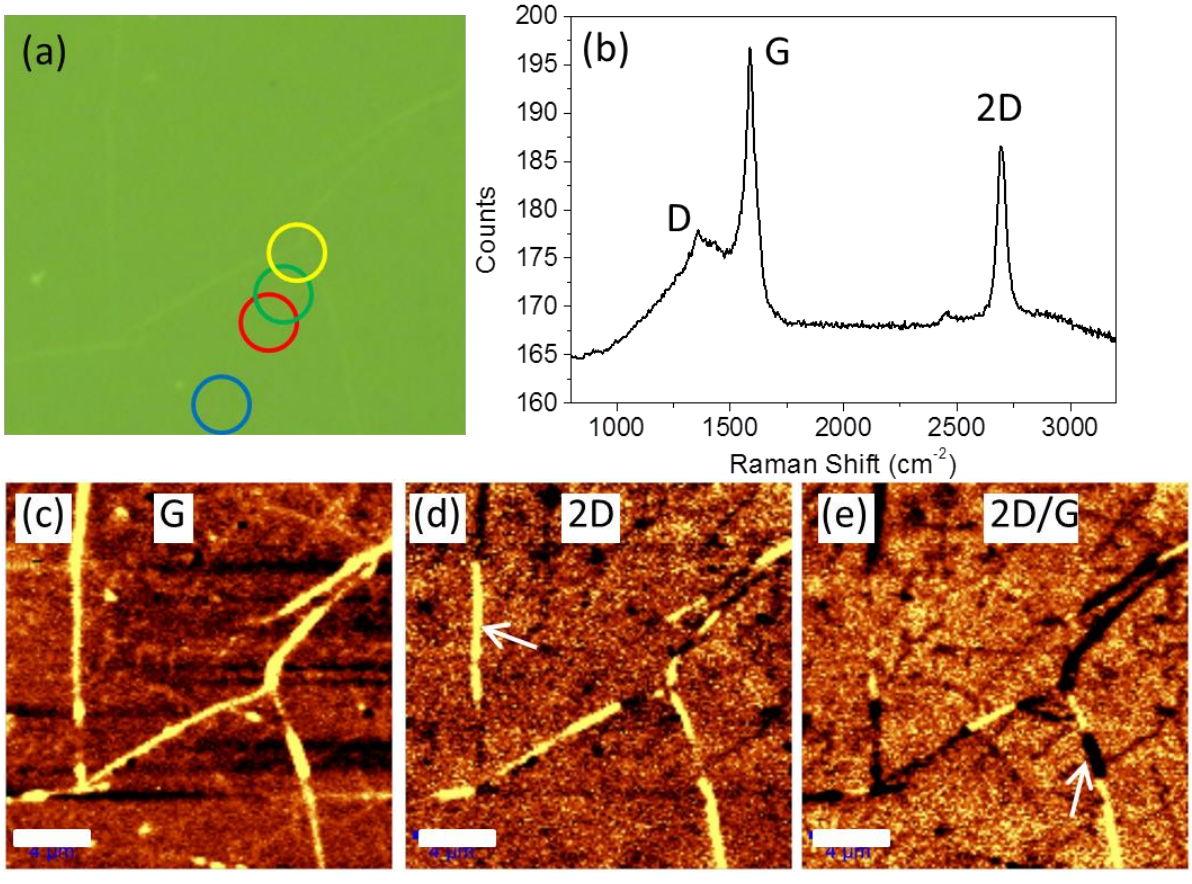

Figure 4.2: (a) Optical image of graphene on glass. The circles represent measurement points in Figure 4.4. The large visible lines are creases. (b) Average Raman spectrum away from the creases. (c-e) Raman maps of the G, 2D peak intensities, and 2D/G ratio, respectively. Scale bars are 4 μm.

An optical image of the first region under study is shown in Figure 4.2(a). The green tint is due to the Raman filter. The primary visible features are the creases. The average Raman spectrum over the areas more than 2 μm away from any creases is shown in Figure 4.2(b). The D peak, located near 1360 cm^{-1}, is due to breathing modes of sp^2 carbon atoms in rings and is activated by and scales with the density of defects as graphene becomes nanocrystalline[124]. The

G peak, located near 1590 cm^{-1}, is due to the in-plane bond stretching of all pairs of sp^2 carbon atoms[124]. The 2D peak, located near 2700 cm^{-1}, is the second order of the D peak[125]. The 2D peak is sharp and symmetric. The values of the full width at half maximum (FWHM) of the 2D peak form a Gaussian-like distribution around a FWHM of 43 cm^{-1}. Raman spectra taken with the same system on exfoliated graphene flakes yielded a FWHM of ~ 28 cm^{-1} for monolayer graphene and ~ 50 cm^{-1} for bilayer graphene. There were no points in the Raman map of this CVD graphene sample with a 2D peak FWHM less than 30 cm^{-1}, yet there certainly should be at least some area consisting of monolayer graphene. Therefore, the CVD graphene film likely yields a wider 2D peak than normal due to doping but consists of primarily monolayer graphene. The ratio of the intensity of the 2D peak to G peak is low compared to mechanically exfoliated monolayer graphene flakes but is not uncommon among CVD-grown graphene. This is because the G peak signal is enhanced due to the presence of regions with more than one graphene layer[126] and carbon-based residue which was not fully removed during the annealing step. A high doping level may also be responsible, and will be discussed further below. Maps of the G peak intensity (I_G), 2D peak intensity (I_{2D}), and the ratio of the 2D peak to G peak intensities (I_{2D}/I_G) are shown in Figures 4.2(c-e), respectively. The background, which varied with position, was subtracted from each calculation.

It is clear from Figures 4.2(c-e) that the creases are not uniform and contain many features. Analysis of the Raman spectra of the different regions reveals a wide variety of structural characteristics. The region marked with the white arrow in Figure 4.2(e) has the lowest ratio of D peak intensity to G peak intensity (I_D/I_G) and consists of several layers of high crystalline quality graphene. The bright yellow regions within the creases of Figure 4.2(e) consist of single layer graphene as evidenced by large I_{2D}/I_G ratio. One possible reason that these regions

show an enhanced I_{2D}/I_G compared to the surrounding graphene could be because they are slightly suspended during the drying process. Ni *et al* found that suspended graphene had a higher 2D peak intensity due to the absence of substrate charged impurities which increase carrier density and electron or hole inelastic scattering rate which in turn reduce I_{2D} [127]. The region marked with the white arrow in Figure 4.2(d) displays a large I_{2D} and I_G, such that the ratio is indistinguishable from the surrounding graphene. This is may be due to an interference effect which enhances Raman band intensity due to multiple reflections of the laser or the Raman signal itself[128]. The remaining dark regions within the creases of Figure 4.2(e) contain an enhanced G peak, suggesting multiple layers, possibly due to folding. The height of the creases was below the resolution of the AFM system, suggesting that they may be no more than 3 Å above the surrounding graphene. Further investigation with a higher resolution AFM system is planned.

In addition to the prominent creases, fainter boundaries separating regions of approximately 2 – 6 μm in size are visible in Figures 4.2(c-e). These are suspected to be the wrinkles due to the difference in thermal expansion of graphene and copper. Corresponding features are visible in Raman maps of graphene on copper, as shown in Figure 4.3, indicating that they are intrinsic to the growth process and not due to the transfer. The wrinkles are visible in the optical image on copper in Figure 4.3(a) and appear as dark boundaries in the G and 2D peak intensity plots in Figures 4.3 (b-c), respectively. These images were taken on a different sample grown under the same conditions. The resulting domain size is very similar to that in Figure 4.2. Performing Raman spectroscopy on graphene directly on copper is more difficult than on glass due to a large fluorescence signal from copper and the uneven surface of the foil.

The dark and light diagonal bands in Figures 4.3 (b-c are likely due to a difference in laser spot focus on the uneven surface.

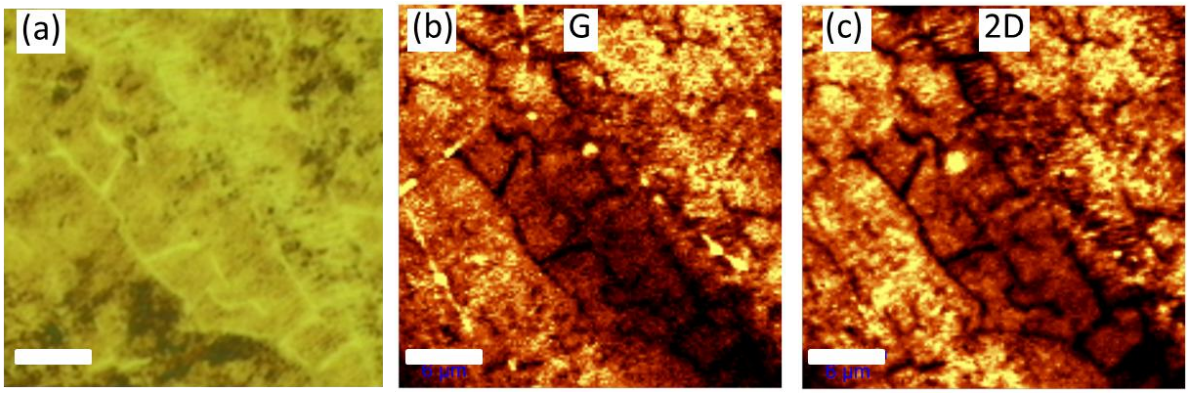

Figure 4.3: (a) Optical image of graphene grown on copper. (b), (c) Map of G, 2D peak intensity in the region depicted in (a). All scale bars are 6 μm.

No creases are visible in Raman maps of graphene on copper, and neither creases nor wrinkles are visible in exfoliated graphene, as expected. The wrinkles are most visible in Figure 4.2(e) and are also clear in the map of the 2D peak position (not shown), in which they are shifted to lower wave numbers. The map of the G peak position, however, is completely featureless. The positions of both the G and 2D peaks in graphene have been shown to be sensitive to doping level[101,129,130], with both peaks shifting with increased n- or p-type doping. The G peak nearly symmetrically shifts to higher wave numbers regardless of the doping type, while the 2D peak shifts to lower (higher) wave numbers for n-type (p-type) doping. The boundaries discussed here, however, display a shift of the 2D peak but not the G peak. Das *et al* found that the shift of the 2D peak due to n-type doping by electrostatic gating became more prominent at high doping levels while the shift of the G peak saturated[129]. Additionally, they observed a decrease in the ratio I_{2D}/I_G at high n- or p-type doping, with the value dropping below unity for electron or hole concentrations above approximately 2×10^{13} cm^{-2}. These observations

indicate a high level of doping in the graphene film in this study and may also help explain the relatively low I_{2D}/I_G observed in this work. Electronic measurements of other graphene films fabricated with the same procedure reliably exhibit Dirac points greater than 30 V using a back gate and 90 nm SiO_2, indicating strong p-type doping in as fabricated films. Together, these observations suggest that the film is primarily p-doped while wrinkles are n-doped. This suggests that if doping is in fact responsible for the 2D peak shift of the wrinkles in the transferred film, the wrinkles may become doped either during the copper etching or transfer process. Because the iron chloride solution used to etch the copper is highly oxidative, it could be that the etchant dopes the graphene film p-type but cannot reach certain areas of graphene which are folded up in the wrinkles. This does not, however, explain why the wrinkles would be heavily n-doped. The mechanism behind this doping trend is not understood at this point; further studies are needed.

Grain boundaries have been reported to appear solely in the Raman map of the D peak intensity due to the presence of structural disorder at the location of merged grains[121,122,131]. The map of D peak intensity in this work, however, is featureless except for some portions of the large creases. The reason that the grain boundaries are not visible is suspected to be because the grain size is smaller than the excitation laser beam spot. The average grain size can be estimated based on I_D/I_G according to the equation:

$$L_a(nm) = (2.4 \times 10^{-10})\lambda_{laser}^4 \left(\frac{I_D}{I_G}\right)^{-1} \quad (4.5)$$

where λ_{laser} is the laser wavelength in nanometers[132]. This yields an average grain size of 278 nm, which is consistent with other estimates on CVD grown graphene using this equation[133,134]. Given that the laser beam spot is as small as 330nm (given by WITec) and the Raman spectra are taken at a rate of 8 points per micron, the absence of grain boundaries in the Raman maps is consistent with this estimate of grain size.

4.4 Optical Measurement of Diffusion

In order to study the effect of the above three types of boundaries on charge carrier dynamics, especially transport properties, transient absorption microscopy measurements were performed in the same region. A 100-fs laser pump pulse with a central wavelength of 756 nm was tightly focused to the graphene film with a spot size (FWHM) of 2.3 μm. This excites electrons to the conduction band by interband absorption. A 100-fs probe pulse with a central wavelength of 1734 nm and a spot size of 3 μm is used to detect these injected carriers. The differential transmission of the probe pulse induced by the carriers is measured by using a mechanical chopper to modulate the pump beam intensity at a few kilohertz and detecting the transmitted probe with a photodiode and a lock-in amplifier referenced to the modulation frequency. The differential transmission signal is proportional to the carrier density and therefore can be used to monitor the carriers. Since the laser spot sizes are about 10 times larger than typical grain sizes but smaller than typical wrinkles and creases, the measurement results must be due to either wrinkles or creases, while the effect will be one of averaging over many grain boundaries.

First, we measured the differential transmission as a function of the time delay of the probe pulse with respect to the pump pulse, with the two laser spots overlapped in space. A typical signal decay profile is shown in Figure 4.4(a). The data is best fit by two time constants: t_1 = 0.2 ps and t_2 = 1.4 ps. This is qualitatively consistent with previous measurements on exfoliated graphene[135], reduced graphene oxide[136], epitaxial graphene on silicon carbide[136–138], and with the following mechanism. After excitation, the carriers quickly thermalize through carrier-carrier intraband scattering and then relax through carrier-phonon interband scattering. We attribute the two time constant to the thermalization time and energy relaxation time of these

hot carriers.

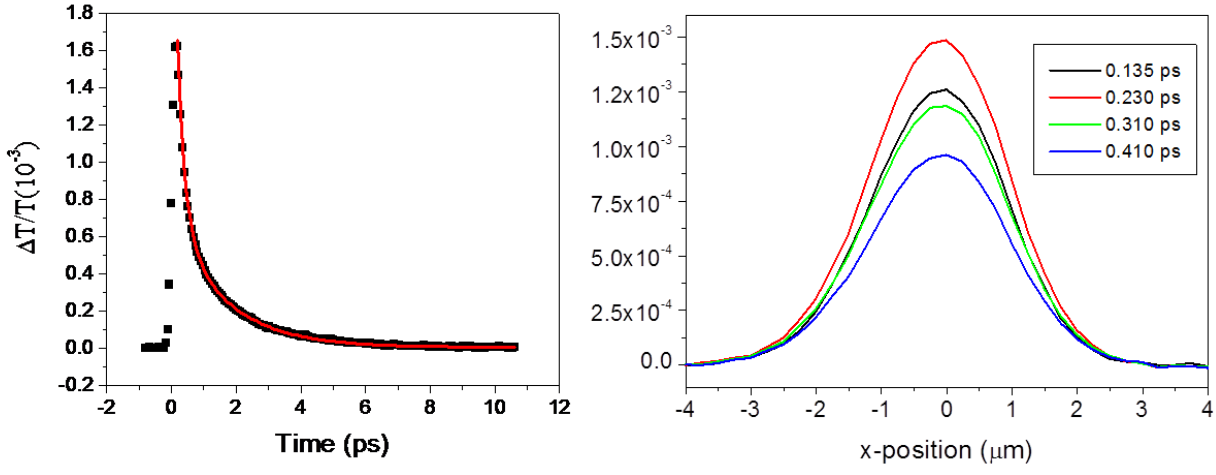

Figure 4.4: (a) Typical ΔT/T decay profile with exponential fit. (b) Example spatial distribution of charge carriers given by ΔT/T versus probe position at four different probe delay times.

Next, we used recently developed techniques to study carrier diffusion in various positions in this area[136]. Here, the differential transmission signal is measured as we scan the probe spot across the pump spot with a fixed probe delay. This yields a spatial distribution of the carriers at that probe delay. This is illustrated in Figure 4.4(b), which shows an example differential transmission signal as a function of the probe position and delay time relative to the pump pulse. Since the laser spots have Gaussian shapes, the initial distribution of carriers is Gaussian. Diffusion of carriers within the graphene film will cause the size of the distribution to increase. Quantitatively, the squared width increases linearly with time, with a slope determined by the diffusion coefficient[136] according to the equation

$$w^2(t) = w^2(0) + 16\ln(2)Dt, \tag{4.6}$$

where *w* is the width of the carrier distribution, and *D* is the diffusion coefficient. The squared width can be deduced by a Gaussian fit of the measured carrier profiles and plotted as a function of time in order to extract *D*, the diffusion coefficient.

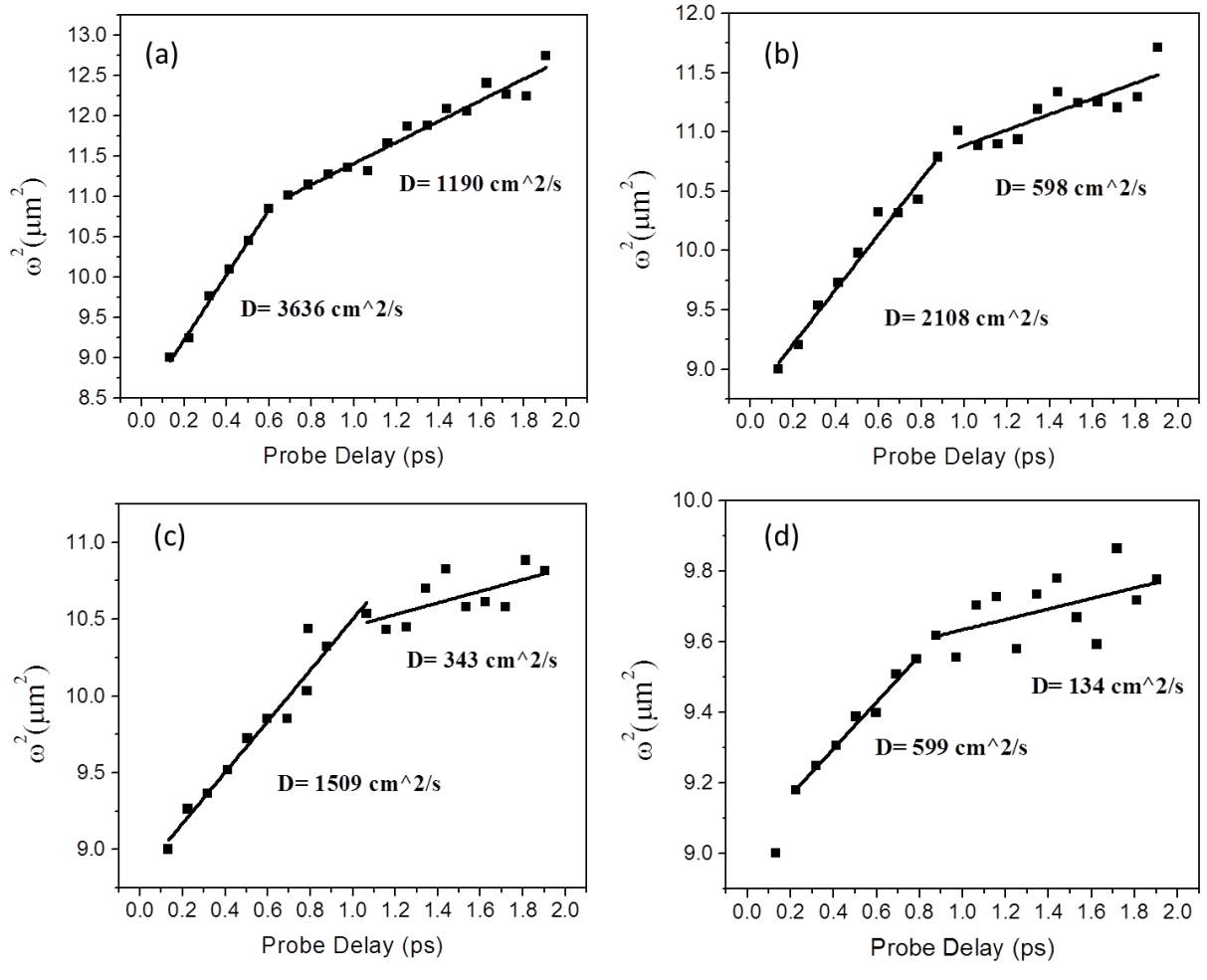

Figure 4.5: Measurements of diffusion coefficient at the four locations marked in Figure 4.2(a). Carrier profile width squared is plotted against probe delay time so that the slope is equal to the diffusion coefficient. Plots (a-d) represent the blue, red, green, and yellow circles in Figure 4.2(a), respectively.

In order to study the influence of the crease on carrier dynamics, measurements of diffusion coefficient at four locations are shown in Figure 4.5(a-d), representing the blue, red, green, and yellow circles in Figure 4.2(a), respectively. Figure 4.5(a) is measured away from any

creases, and Figures 4.5(b-d) sequentially approach the wishbone shaped intersection of creases with each subsequent point containing an increasing contribution from the creases. At every position the carrier behavior is best modeled by two separate diffusion coefficients: one for short probe delay times of up to 0.6 - 1 ps, denoted D_1, and one for longer probe delays, denoted D_2. As the excitation site approaches the crease intersection, both D_1 and D_2 decrease but the ratio D_1/D_2 increases. Stated another way, there is a faster decline in D_2 than D_1. This suggests that D_2 may be more sensitive to the presence of the crease and may be less intrinsic to CVD grown graphene than D_1.

At every position there is a clear, significant broadening of the carrier density profile owing to the diffusion of carriers. Although the diffusion equation predicts an overall linear increase of the squared width of the profile, there appears to be two time ranges with different slopes. The initial fast expansion is followed by a seemingly slower one. Recently, the nature of the transient absorption signal at late probe delays (i.e. > 1 ps) in CVD graphene has been studied[139]. This recent study showed that such a slow component might be induced by extrinsic agencies in the samples which can be removed by prolonged laser exposure. The profiles measured at late probe delays could be a superposition of a fast-expanding profile induced by the charge carriers and a nonexpanding profile caused by these extrinsic agencies. This can give rise to an apparently slower expansion. However, at early probe delays the carrier contribution dominates, and the expansion accurately reflects the carrier diffusion. Hence, in the following we will focus on the initial expansion and D_1 only.

To further separate the role of the wrinkles and creases, D_1, t_1, and t_2 were measured in two linear scans over a second region of graphene, presented in Figure 4.6. Figure 4.6(a) shows an optical microscope image of the area of interest. The curved bright feature at the top of the

image is part of a titanium alignment marker. The two black horizontal lines denoted y_1 and y_2 are separated by 1 μm and represent scans of the diffusion coefficient D_1 and signal decay profile. Each line contains seven data points with a step size of 1 μm. The far left point is denoted as position 0 μm. A crease runs through the center of the scan, at the 3 μm position.

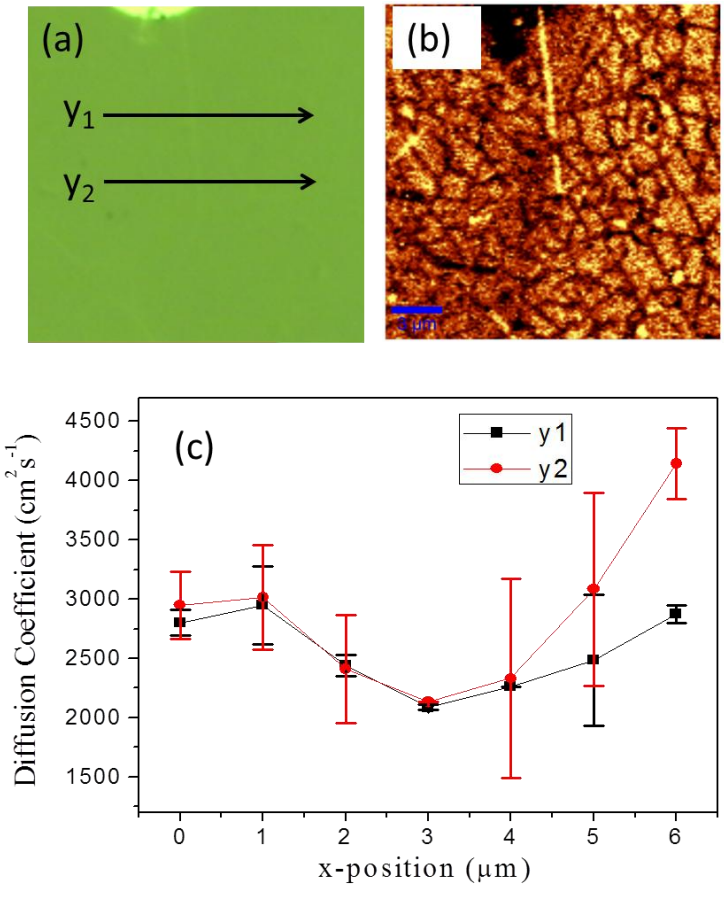

Figure 4.6: (a) Optical image of the region of interest. The two scanned lines are marked with black arrows. (b) Raman map of the ratio I_{2D}/I_G in the region shown in (a). The scale bar is 6μm. (c) Map of diffusion coefficient D_1 versus position along scans y_1 and y_2.

This is clearly visible as the vertical bright yellow line in the Raman map of I_{2D}/I_G in Figure 4.6(b). Also visible are wrinkles separating regions of a few microns in size. Diffusion coefficient D_1 is plotted against position in Figure 4.6(c) for both scans y_1 and y_2. It is clear that

the diffusion is worst when the pump pulse is directly on top of the crease. Interestingly, the differential transmission decay time constants, shown in Figure 4.7 show no clear trend relative to position, suggesting that the crease does not affect carrier lifetime. Scans y_1 and y_2 yield similar diffusion coefficients at all points except for position 6 μm. Since the probe beam spot is 3 μm in diameter, scans y_1 and y_2 will both contain information from a shared central horizontal strip. Scan y_1 (y_2) will also contain information from a strip above (below) the central strip of graphene film. The close overlap of the two data sets is not surprising since the crease runs equally through both scans.

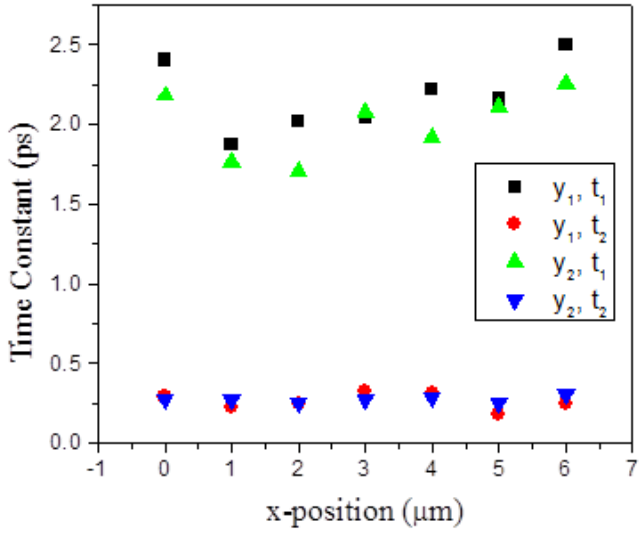

Figure 4.7: Signal decay time constants t_1 and t_2 along each point in scan y_1 and y_2

The clear difference in D_1 between scans y_1 and y_2 at position 6 μm is interesting. One possible explanation for this difference could be the presence of wrinkles, as follows. The wrinkles may serve as obstacles that decrease the diffusion of charge carriers, particularly if they are charged relative to the surrounding graphene film. The typical wrinkle domain size is on the order of or a few microns larger than the beam spot. For this reason, the points in scans y_1 and y_2

are likely to have very similar fractional areas consisting of wrinkles. At positions 5 and 6 μm, however, it is possible that y_2 may by chance probe an area entirely or nearly within a single wrinkle domain. This would imply that carriers can diffuse farther before encountering a wrinkle, leading to a 50% increase in diffusion coefficient for positions 6 μm. One interesting consequence of this hypothesis is that the effect of the crease is comparable or smaller than the effect of the wrinkles on the carrier diffusion judging by the size of the dip in the center of this curve at the position of the crease. This may be because the creases consist of folds and bends in the graphene film which may not alter the electronic structure much. The wrinkles on the other hand form at higher temperatures in a more dynamic process and may be doped relative to the surrounding graphene or consist of very sharp folds.

The results in this section suggest that the diffusion coefficient is affected by the presence of creases and wrinkles, but the exact mechanism explaining these trends is not obvious. Diffusion coefficient of carriers with a certain temperature is determined by the mean free path of those carriers. The mean free path is limited by various scattering mechanisms. The most important contributions are phonon scatterings and defect/impurity scattering. The reduced diffusion coefficient in the regions with creases and wrinkles can be attributed to the increased defect/impurity densities since we do not expect the phonon scatterings to be influenced significantly by the creases and wrinkles.

4.5 Summary and Future Work

To summarize, the microstructure of graphene grown by CVD on copper was studied with Raman spectroscopy and correlated with optical measurements of carrier diffusion. By avoiding patterning the film and depositing metal electrodes, several complicating factors are

avoided. We found that in addition to grain boundaries, wrinkles formed during cooling after growth and creases from the transfer process both affect carrier diffusion by comparable amounts. Additionally, it was suggested that wrinkles may be heavily doped oppositely than the rest of the graphene film. This could be due to the oxidizing nature of the copper etchant which also contacts the graphene film. This work contributes to the effort to improve the quality of CVD grown graphene films so that large area graphene films can reach the demonstrated potential of exfoliated graphene flakes and become a commercially viable transparent conductor.

Since much of the work on this project was done very near to the time of the writing of this dissertation, the questions raised by the study have not yet had a chance to be investigated. One main question likes in the slower diffusion coefficient, D_2, at longer probe delays. Earlier studies on graphene grown on SiC did not observe D_2 because the carriers relaxed out of the probing window before the *longer time* regime could be reached. It is possible that D_2 could be due to some kind of contamination on the surface on graphene that can be burned off with laser exposure. When graphene is transferred from copper there will be some PMMA residue on the graphene which is difficult to remove fully. This residual PMMA could be the extrinsic agency mentioned above which contributes to the differential transmission signal without an expanding carrier profile. It is also possible that D_2 is caused by some kind of defect structure in graphene which slows diffusion. If this is the case, it suggests that laser exposure can somehow treat or modify these defects. Even if this is not the most likely scenario, it would be extremely interesting.

The first step in sorting this out is to repeat the experiment on graphene on SiC. By using the recently developed technique of probing at lower carrier energies, longer probe delays can be accessed. If D_2 is observed, PMMA is not responsible. If D_2 is not observed, PMMA can be spun

on the graphene, baked, and removed in acetone in order to simulate the processing of CVD grown graphene. If D_2 is observed, then PMMA is responsible. If it is not observed, then PMMA is not responsible and there is evidence that D_2 could be intrinsic to graphene. Another interesting study would be to change the copper etchant or the amount of time graphene is exposed to the etchant to see how it affects the results of this study. If the copper etchant is responsible for the doping trend of the graphene film and wrinkles, it could very well have an effect on diffusion. The correlation of diffusion as measured by optical techniques with microstructural characterization is a powerful approach, and I hope it continues after I leave KU.

Chapter 5

Graphene-Metal Contact for Studying the Superconducting Proximity Effect in Graphene-Nb Junctions

5.1 Introduction

5.1.1 Introduction to This Chapter

This project began over one and a half years ago with the goal of demonstrating the superconducting proximity effect in graphene with niobium electrodes. At the time, no one had reported this phenomenon using Nb, which is significant because the critical temperature of Nb is 9.2 K, which is well above liquid helium temperature of 4.2 K and the highest of all elemental superconductors. As is sometimes the case, this project experienced significant delays due to unforeseen equipment failures. More importantly, as will be discussed later in this chapter, this project was also delayed by a difficulty in achieving acceptable contact between the metal and graphene. It often happens in research that an interesting problem surfaces en route to the intended experiment, and this project is an example of such an occurrence.

Because graphene is a single layer of atoms, the nature of its contact is highly sensitive to the particular electrode material, graphene surface contamination, deposition technique, and deposition conditions. Additionally, as will be discussed below, the superconducting phenomena of interest in this work are themselves highly sensitive to graphene-superconductor contact quality. These two facts make the study of contact to graphene extremely important. As mentioned in the first chapter of this dissertation, contact to a nano-scale structure such as graphene is an essential component of a device's microstructure. Without a thorough

understanding of the microstructure of the graphene-superconductor contact interface, the intended phenomena may be destroyed or difficult to measure or interpret.

While many devices suitable for testing at low temperature have been fabricated, this project has not yet reached the stage of characterizing the proximity effect in graphene-Nb junctions due to equipment complications. Nonetheless, it is still an important topic to include in this dissertation. The importance of the overarching theme of correlating microstructure of carbon-based nano-materials with electronic performance is emphasized by these findings. Additionally, the depth of physics which one can study in an optimized graphene-Nb system is significant and worth pursuing. Certainly if I were staying at KU longer I would be focused on this project for the duration of my tenure. This chapter will introduce the physics and properties of graphene which are relevant to the superconducting proximity effect, discuss the previously reported works and their relevance to the contact issue, and present our findings so far. Finally, the outlook, ongoing work, and future steps will be outlined.

5.1.2 Brief Introduction to Superconductivity and the Superconducting Proximity Effect

Superconductivity, the phenomenon of zero dc electrical resistance below a critical temperature, was discovered by H. Kamerlingh Onnes in 1911. His pioneering work with liquid helium and the properties of matter at low temperatures earned him the Nobel Prize in Physics in 1913. In the following century, a great amount of effort has been invested in the field of superconductivity, including research leading to four additional Nobel Prizes. Superconductivity is indeed a very deep and rich field of physics, the majority of which is well beyond the scope of this dissertation. This introduction will briefly explain the relevant phenomena only to the point

which is necessary to understand the motivations behind the experiment with graphene and the importance of the graphene-superconductor interface.

The superconducting state involves the flow of electrical currents without any voltage drop, the expulsion of magnetic fields from the interior of the material (known as the Meissner effect), the quantization of the magnetic flux through a hole in the material, and the appearance of an energy gap in the excitation spectrum of the electrons. The Bardeen-Cooper-Schrieffer (BCS) theory showed these phenomena were a result of the formation of electron pairs, called Cooper pairs. These pairs, consisting of electrons with opposite spin, form due to a phonon-mediated attractive force. Essentially, the charge of one electron creates a deformation in the lattice resulting in a region with slightly higher positive charge density, attracting the second electron. The Cooper pairs are quasi-bosons which condense into a single macroscopic quantum state. This leads to the so-called superconducting energy gap which is highest at low temperatures and vanishes at the critical temperature. With this imagery in mind, it is not hard to imagine that superconductivity might "leak" into a normal non-superconductor. This is known as the proximity effect.

The proximity effect can be explained as follows[140]. If a superconductor and a normal non-superconductor are in intimate contact, assuming there is no oxide or contamination between them, there will be a leakage of Cooper pairs from the superconductor, *S*, into the normal material, *N*, and a leakage of normal electrons from *N* into *S*. Once the Cooper pairs cross the *SN* interface they will eventually de-pair, and once the normal electrons cross the *SN* junction they will eventually pair up. This results in a reduction of the pair density in *S* and an appearance of a pair density in *N*. These variations can extend several hundred nanometers in each medium, corresponding to the coherence length in each material. As a result the critical temperature of *S* is

suppressed, and signs of superconductivity arise in *N*. If the normal channel is short enough, a supercurrent can flow through a *SNS* junction. If the *N* material is a semiconductor instead of a metal, the carrier concentration, *n*, can be tuned. The coherence length in *N* will then be proportional to $n^{1/3}$.

Related to the flow of Cooper pairs and normal electrons across *SN* interfaces is a phenomenon called Andreev reflection. Andreev reflection is a type of scattering which occurs at *SN* interfaces by which a normal current is converted into a supercurrent. When an electron (hole) is incident on the *SN* interface from the normal side at energies less than the superconducting energy gap, it forms a Cooper pair in the superconductor with the retroreflection of a hole (electron) of opposite spin and momentum to the incident electron (hole), as seen below in Figure 5.1.

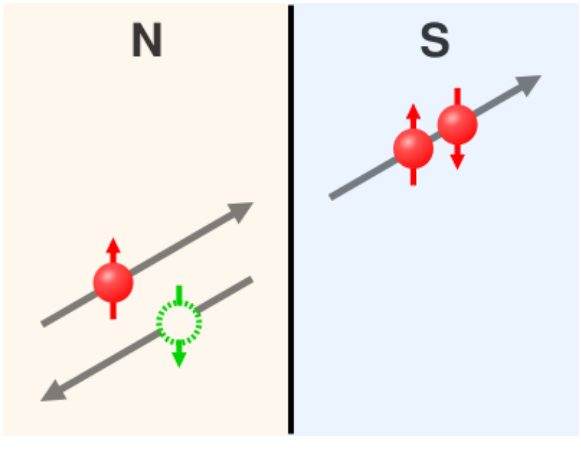

Figure 5.1: An electron, shown in red, is incident on the normal-superconductor interface. It crosses the barrier and forms a Cooper pair in the superconductor by producing a retroreflected hole, shown in green, of opposite spin.

The term retroreflection refers to the fact that the hole is reflected back along the path of the incident electron. This is in contrast to specular reflection, in which the hole is reflected from the interface in a mirror-like geometry. Through time reversal symmetry, the same process works

with an incident hole instead of an incident electron. The process of Andreev reflection assumes that the barrier transparency is high. That is, there is no oxide or tunnel barrier. This will be especially important for graphene, which is just one atomic layer thick and prone to surface contamination.

A similar phenomenon to the proximity effect is the Josephson Effect, the flow of a supercurrent across a Josephson junction which consists of two superconductors separated by a weak link. This weak link could be a thin insulating barrier, a normal metal, or a physical constriction which weakens the superconductivity. Josephson predicted that Cooper pairs could flow through an insulating barrier via quantum tunneling, even with no potential difference[141]. This pair tunneling depends on the difference in phase of the effective wave functions on either side of the junction. This phase difference varies with space and time and is used as the variable in the macroscopic quasi-classical theory for the electrodynamics of the junction. As the separation between the superconductors is reduced, the wave functions penetrate the barrier sufficiently to couple to each other, reducing the system energy. When the energy associated with the coupling becomes greater than the thermal fluctuation energy, the phases become locked and Cooper pairs can pass from one superconductor to the other without energy loss. In section 5.2.2, the previous reports of graphene-superconductor junctions will be presented. Before we get into these details, some important properties of graphene must first be introduced.

5.1.3 Introduction to Graphene's Relevant Properties

Graphene has many properties which make it desirable for electronic devices, including superconducting devices. First, the ability to control the electronic transport properties of a material by application of an external electric field is at the heart of modern electronics, and

graphene meets this requirement easily. Because of the linear dispersion curve near the Dirac point, as presented in Section 4.1, the Fermi level of graphene can be adjusted electrostatically. The ambipolar field effect, which allows a switch between 2D electron and hole gas behavior using an applied gate voltage, was first demonstrated in the seminal 2004 paper by Novoselov *et al*[8]. In pristine graphene, the resistivity versus gate voltage curve has a sharp peak at zero gate voltage. The conductivity increases linearly with gate voltage on either side of the maximum resistivity point. If the graphene is situated on top of a SiO_2-coated Si wafer, the back gate voltage induces a surface charge density given by

$$n_s = \frac{\varepsilon_0 \varepsilon_r V_G}{tq} \tag{5.1}$$

where ε_0 and ε_r are the permittivity of free space and the relative permittivity SiO_2, respectively, V_G is the gate voltage and t is the oxide thickness. A significant concentration of electron (holes), on the order of 10^{13} cm^{-2}, can be induced by a positive (negative) applied gate voltage. The graphene carrier density at negative, zero, and positive applied back gate voltages is depicted clockwise from left, respectively, in the insets of Figure 5.2.

It should be noted that the ability to control the electronic properties via back gate is compromised when multiple layers of graphene are utilized in the device. The current ratio of I_{ON}/I_{OFF}, where the OFF state is defined at the minimum conductivity point and the ON state is defined at a fixed voltage from the Dirac point, decreases as the inverse of the thickness of the graphene stacks in the range from single layer graphene to over ten layers of graphene. This trend reflects a decrease in ON conductivity and an increase in OFF conductivity with increasing number of layers[142]. This can be explained fairly simply. Since the electrodes are deposited on the top of the graphene stack, they can be assumed to only make an electrical connection to the

top one to few layers, depending on the deposition conditions and whether or not a high temperature annealing took place. Additionally, since the screening length in graphene is less than the thickness of bilayer graphene, only the bottom 1-2 layers of graphene are coupled to the potential in the gate oxide. Due to the weak Van der Waals coupling between adjacent graphene layers, any charge modulation in the bottom layers is not fully accessible by top electrodes in the case of a several-layer graphene stack.

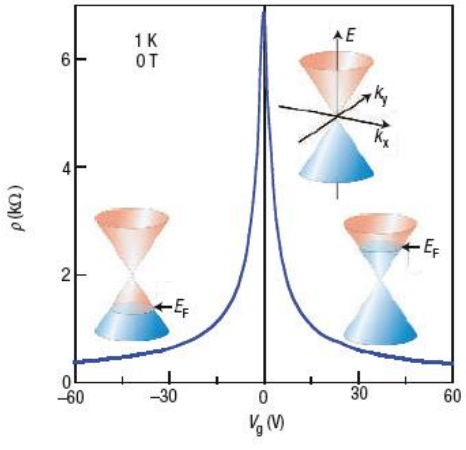

Figure 5.2: Resistivity versus gate voltage as a depiction of the ambipolar field effect in graphene. The insets show the low energy spectrum *E(k)* which displays the change in Fermi level with gate voltage. Figure from reference[20].

The location of the Dirac point, or charge neutrality point (CNP) at $V_G = 0$ is theoretically expected due to the previously discussed band structure, yet deliberate sample fabrication steps must be taken in order to ensure that this is observed. Unintentional doping due to physisorbed water molecules[143] and other environmental adsorbates as well as polymer residue from various fabrication steps leads to hole-metal behavior and a shift of the CNP to positive voltages. By annealing the samples in vacuum at a temperature typically greater than 200°C, one is able to desorb the unwanted adsorbates and shift the peak closer to zero[18]. Alternately, current

annealing by sending a large current through the graphene sample to induce sample heating in vacuum can also achieve the desired effect[144]. Of course, in order for graphene to be measured in its pristine, undoped condition, it must be measured under ultrahigh vacuum (UHV). As soon as the sample is exposed to ambient conditions it will nearly return to its previous doped state[144]. Since measurement in UHV is not always possible or practical, an awareness of the gas adsorption/desorption process is necessary in order to identify and/or minimize the temperature-dependent or current-dependent effects.

Another property of graphene that makes it especially attractive for device applications is its high mobility. Since mobility helps determine the speed at which an electronic device can operate, graphene offers the potential for ultrafast device applications, possibly greater than 500 GHz[18]. Additionally, high mobility allows a large change in conductivity to be induced by a small change in charge carrier density. At a carrier density of 1×10^{12} cm^{-2}, an intrinsic mobility limit on the order of 2×10^5 cm^2/Vs is expected[11]. By comparison, the room temperature mobility limit of silicon is approximately 1.4×10^3 cm^2/Vs, and that of indium antimonide is 7.7×10^5 cm^2/Vs, which is the highest known room temperature mobility of any conventional semiconductor. Because experimental values of $< 10^4$ cm^2/Vs are commonly found in graphene, much work has been done to investigate the limiting factors, specifically the various scattering mechanisms.

As a one-atom thick material, graphene consists entirely of surface. Because of this, graphene's electronic properties are sensitively affected by the underlying substrate. Because there is evidence that exfoliated graphene is free of structural defects[145], the mobility of graphene on SiO_2 at low and room temperatures is thought to be limited primarily by impurity scattering due to charged impurities in the SiO_2[11,146,147]. With a typical charged impurity concentration of

approximately 5×10^{11} cm^{-2}, SiO_2 is known to dominate transport properties of other 2D semiconductor systems[148]. This high concentration of charged impurities is not the only way SiO_2 affects the mobility, however. Remote interfacial phonon scattering, derived from the polar interactions in SiO_2, may also contribute to graphene's room temperature electronic dynamics[11,149], suggesting that nonpolar substrate or suspended samples may help optimize graphene's mobility.

In 2008, Bolotin *et al* took the substrate out of the equation entirely by suspending electrically contacted graphene 150 nm above the underlying SiO_2 gate[150]. They were able to achieve electron mobilities greater than 2.3×10^5 cm^2/Vs at electron concentrations of 2×10^{11} cm^{-2}. By suspending the sample, not only was the scattering due to the substrate removed, but residual impurities that would otherwise be trapped between the substrate and the graphene could be removed by current annealing. Under these conditions, the mean free path was determined to be on the order of the dimension of the device, suggesting that larger area devices may exhibit even higher mobilities by reducing the effect of scattering due to the edges and electrodes.

Yet another attractive property of graphene is the unique nature of its charge carriers[20]. Graphene's charge carriers mimic relativistic particles that are more naturally described with the Dirac equation than the Schrödinger equation. Their interaction with the periodic potential of graphene's honeycomb lattice gives rise to quasiparticles, called massless Dirac fermions, that are accurately described at low energies by the (2+1)-dimensional relativistic Dirac equation with an effective "speed of light" $v_F \approx 10^6$ m/s. The quasiparticles can be viewed as electrons which have lost their rest mass. While the relativistic-like description of electron waves on a honeycomb lattice has been known theoretically for many years, the experimental discovery of graphene allows for a new way to probe quantum electrodynamics, exciting great interest.

Because graphene's charge carriers are massless Dirac fermions, graphene exhibits a half-integer quantum Hall effect[96]. Briefly, the classical Hall effect occurs when a current carrying channel is subjected to a perpendicular magnetic field. The direction of the force on the moving charges due to the magnetic field depends on the sign of the charge, creating a potential difference between the two sides of the channel. The Hall coefficient is the ratio of the induced electric field to the product of the perpendicular magnetic field and the applied current, $R_H = E_y /B_z j_x$, which the Drude model predicts to be $R_H = 1/nq$, where n is the charge carrier density. The quantum Hall effect refers to the quantization of the Hall resistance, which is the ratio of the induced transverse voltage to the applied current. This is caused by the quantization of the energy of electron cyclotron orbits into Landau levels. The charge carrier density can only change when another Landau level crosses the Fermi energy, hence the resistance can only change by steps of h/q^2 divided by an integer, N[151]. When the Fermi energy is between two Landau levels, current in the quantum Hall regime is carried through edge states. Graphene experiences a half-integer quantum Hall effect due to the existence of both electron-like and hole-like Landau states at zero energy[96]. This implies that the lowest Landau level (N = 0) has half the degeneracy of any other N. Stated another way, the degeneracy of the N = 0 Landau level is shared equally by electrons and holes. As a result, the first Hall plateau occurs at half the normal filling. All other levels have normal degeneracy and therefore remain shifted by ½ from the standard sequence.

The final relevant property of graphene which will be discussed is its minimum conductivity. It turns out that graphene's conductivity does not disappear in the limit of vanishing carrier density, but rather exhibits a minimum value close to the conductivity quantum q^2/h per carrier type[96]. For all other known materials, such a low conductivity leads to a metal-

insulator transition at low temperature, but this has not been observed in graphene, even at liquid helium temperatures. Most theories suggest a minimum conductivity value of $4q^2/h\pi$, but experimental data overwhelmingly clusters around $\leq 4q^2/h$ for a variety of experimental conditions[20,152]. So far the origin of this disparity remains an unanswered question in physics despite a vast amount of theoretical work.

Before we delve into the details of the theory and experiment of the proximity effect in graphene, an important distinction should be made. A single atomic layer of carbon, i.e. graphene, is without a doubt a two-dimensional structure. Many studies on graphene, however, utilize what is referred to as "few layer graphene". It is obvious that at some number of layers the material will cease to be graphene-like and will transition to graphite-like, so the question is: how many layers of graphene are needed to make a three dimensional structure? It is known that the electronic structure evolves with each additional layer of graphene until reaching the 3D limit around 10 layers[153]. Additionally, graphene and bilayer graphene have simple electronic spectra, but for three and more layers the spectra become increasingly complicated and the valence and conduction bands start significantly overlapping[153]. Looking at the problem from another perspective, the screening length in graphite is approximately 5 Å, which is a thickness of less than two layers of graphene[142,154]. Based on this figure, a differentiation between surface and bulk is required for five or more layers of graphene. For the sake of clarity, this chapter will refer to the graphene thickness variations as single layer graphene (one layer), bilayer graphene (two layers), few layer graphene (3-10 layers), and thin film graphite (11+ layers).

5.2 Superconducting Proximity Effect in Graphene

5.2.1 Introduction

Any weak link between two superconductors can support a supercurrent in equilibrium, assuming the dimension of the weak link is sufficiently small[155]. The maximum current, or critical current I_c, is characteristic of the strength of the link. A measure of the coupling strength is the resistance of the junction in the normal state, R_N. The product I_cR_N increases as the separation of the superconductors decreases until it saturates at a value on the order of Δ_0/q, where Δ_0 is the superconducting energy gap of the superconductors. This is all well-established *SNS* junction physics[156] which also applies to superconductor-graphene-superconductor (*SGS*) junctions.

Because graphene's charge carriers are described by the relativistic wave equation (i.e. The Dirac equation), graphene provides a unique opportunity to explore the physics of the "relativistic Josephson Effect". Because of graphene's easily tunable Fermi level, it is interesting to ask what happens to the critical current as zero carrier concentration is approached. Titov *et al* theoretically found that the maximum supercurrent that can flow through strip of graphene with Fermi level at the Dirac point is $I_c = (W/L)q\Delta_0/\hbar$, where W and L are the graphene channel width and length, respectively[157]. Here L is small compared to W and the superconducting coherence length. As the carrier density moves away from zero, the Fermi wavelength, λ_F, replaces length in the equation, and the usual ballistic result is obtained: $I_c = (W/\lambda_F)q\Delta_0/\hbar$. Here $\lambda_F = 2\pi/k_F$, and k_F is the wave vector of the electrons at the Fermi level. This unusual length scaling of the Josephson effect at zero carrier density should be observable in graphene-superconductor experiments.

Another phenomenon which should be experimentally observable is specular Andreev reflection. As mentioned above, in typical *SN* interfaces an electron incident from the normal side is reflected as a hole while the missing $2q$ enters the superconductor as a Cooper pair. The

hole is retroreflected so that it travels along the same path as the original incident electron. Beenakker predicted that if the Fermi level is within Δ_0 of the Dirac point, Andreev reflection in graphene is specular, meaning that the hole is reflected in a mirror-like fashion[158]. These situations are shown in Figure 5.3.

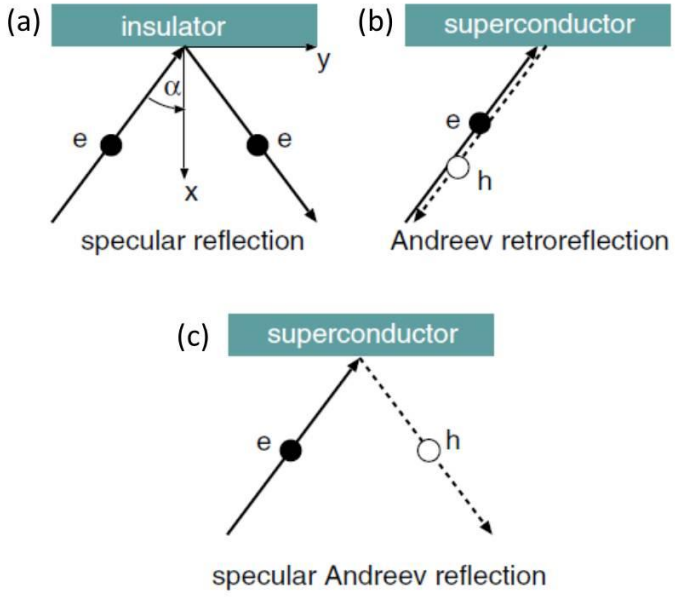

Figure 5.3: (a) Specular reflection occurring in a normal metal-insulator interface. (b) Andreev retroreflection occurring at the interface of a normal metal and a superconductor. (c) Specular Andreev reflection in a graphene-superconductor interface. The process is like Andreev reflection, but the reflection angle is inverted. Arrows indicate direction of velocity, solid lines represent electrons, and dashed lines represent holes. From reference[158].

The reason is as follows. In conventional Andreev reflection, both the electron and hole of the Andreev pair belong to the conduction band. In monolayer and bilayer graphene close to the Dirac point, an electron in the conduction band can be reflected into a hole in the valence band. This leads to specular reflection instead of retroreflection. The difference in reflection angle was predicted to have a clear experimental signature: the subgap conductance should increase with

voltage from 4/3 to twice the ballistic value in the case of retroreflection, but it should drop from twice to 4/3 the ballistic value in the case of specular reflection.

This phenomenon is of fundamental interest, as it explores the intersection of superconductivity with relativistic dynamics. In addition, one could apply a strong magnetic field to put the *SGS* junction in the quantum Hall regime, where current is carried along edge modes instead of through the graphene interior lattice. Of course, the proposed experimental observations depend critically on the ability to create high quality contacts between graphene and a superconductor. As indicated earlier in this dissertation, this is not a given.

5.2.2 Previous Reports

The first experimental report of the superconducting proximity effect in graphene came in 2007, utilizing single and few layer graphene flakes on a SiO_2/Si substrate with two closely spaced (~ 400 nm) Ti/Al bilayer (10/70 nm) electrodes[159]. According to the authors, titanium was used to ensure good electrical contact to graphene, and aluminum to ensure a sufficiently high critical temperature. No details of the electrode deposition conditions were given, although electron beam evaporation is the expected method. The critical temperature of Al is 1.2 K, and the experiment was performed in a dilution refrigeration setup at 35 – 100 mK. The authors measured 17 devices in total, ranging from one to four layers thick, and all exhibited proximity-induced supercurrents. The critical current ranged from ~ 10 nA to more than 800 nA at high gate voltage. A supercurrent was observed for both positive and negative gate bias, as well as at the Dirac point, in agreement with the above theory. This demonstrates that the supercurrent can be carried by hole Cooper pairs or electron Cooper pairs, depending on whether the Fermi level

is in the valence or conduction band, respectively. The critical current increased with increasing doping level and remained finite at the Dirac point for all samples measured.

The differential resistance, *dV/dI*, versus bias voltage curve showed a series of minima at source-drain biases of $2\Delta_0/qn$, *(n=1, 2…)* due to multiple Andreev reflections[160]. Above $Vsd = 2\Delta_0/qn$, the differential resistance returned to the normal value. This measurement enabled a calculation of the superconducting energy gap of $\Delta_0 = 125$ μV, which is consistent with previous findings for Ti/Al bilayers and carbon nanotubes. They did not determine whether these reflections were specular or retroreflections. From the suppression of *dV/dI* observed while changing the bias from above to below the superconducting energy gap, the average transparency of the superconductor-graphene interface was estimated to be ~ 0.7 – 0.8. This gives us a reference point regarding what interface transparency is needed to observe these phenomena in a graphene-superconductor junction.

Following this work, more graphene-superconductor junctions were studied, including others with Ti/Al electrodes[161–163] as well as PbIn[164,165], W[166], Pt/Ta[167], NbTiN[168], Ti/Nb[169], Pd/ReW[170], and Pd/Nb[170,171] electrodes, and graphene with tin islands and normal electrodes[172]. The two reports on Pd/Nb electrodes come from the same group. The work with tungsten electrodes[166] was conducted at the same time as the above work with Ti/Al electrodes, but was published second. They utilize tungsten electrodes grown on few layer graphene by decomposition of a metallo-organic vapor under a Ga focused ion beam with accelerating voltage of 15 kV. The primarily tungsten electrodes are amorphous and contain about 10% Ga, 10% C, and 5% O. The proximity effect appeared below 1.7 K (T_c of pure electrodes was 4.3 K) in the form of a smooth decrease of the junction resistance by a factor of two, but a zero resistance state was not reached down to the base temperature of 60 mK. This may be due to

poor electrode transparency to Cooper pairs due to non-optimal electrode deposition conditions which may damage graphene or introduce amorphous carbon residue in the junction.

The reported work with Pd/Nb electrodes is of particular interest since we also chose to utilize Pd/Nb electrodes in our work. The Pd bottom layer was stated to be 4 – 8 nm thick, but the thickness used in the device which yielded the published data was not given. Before sputtering of Pd and Nb, the samples were annealed in vacuum in the sputtering chamber at 100 °C for one hour. The authors do not comment on the reason behind this annealing step, but one can speculate that its purpose was to clean the graphene surface by desorbing loosely bound adsorbates such as water. Out of 12 samples measured, three showed a full proximity effect at 200 mK with a channel length of up to 1.2 μm. Results at liquid helium temperature were not given. In those which showed a full proximity effect, the critical current was nearly twenty times smaller than expected based upon the junction length and coherence length, $\sqrt{\hbar D/\Delta_0}$, where D is the diffusion coefficient in graphene[173]. This was attributed to the partial transmission at the graphene-superconductor interface since the critical current decay with temperature was faster than expected for a perfect interface[174]. In fact they estimate a contact resistance of roughly five times the graphene channel resistance. This provides us with another reference point regarding what measurements are possible with a given contact quality and again emphasizes the importance of high transparency contact to graphene.

Indeed, several groups reported special efforts necessary to achieve highly transparent contact to graphene. Rickhaus *et al* found that the thickness of their bottom Ti layer was critical to the transparency of the Ti/Nb electrodes[169]. Samples with less than 4 nm Ti showed exponentially increasing resistance with decreasing temperature. They did not comment on thicker Ti layers, but since they utilized 4 nm in their reported devices it can be assumed that

thicker Ti layers provided no benefit. With these contacts they were able to achieve a full proximity effect at various gate voltages. Also, due to the high critical magnetic field of the niobium, they were able to enter the quantum Hall regime of graphene in which there was a clear conductance enhancement in the plateau states of the quantum Hall effect.

Popinciuc *et al* utilized NbTiN electrodes with three different graphene contact conditions: direct sputtering of NbTiN onto graphene, utilizing a protective electron beam evaporated Ti layer under NbTiN, and utilizing a protective electron beam evaporated Ti/Au layer under NbTiN[168]. They found that sputtering NbTiN directly on graphene resulted in a very high contact resistance of several 10^5 Ω. Quite expectedly, they were unable to observe any proximity effect in these devices. The high contact resistance was attributed to damage to the graphene layer under the superconducting electrode due to exposure to the sputtering plasma and/or energetic sputtered particles. The DC voltages used in the sputtering process were on the order of 380 V. In order to avoid damage to graphene they opted to utilize electron beam evaporated contact layers which involve particles with energies on the order of only ~ 1 eV. After evaporation of Ti and transfer to the sputtering chamber through air, an Ar RF plasma cleaning was applied to the Ti in order to remove the inevitable TiO_2 on the surface. In the case of Ti/Au evaporation, there was no RF cleaning performed since oxidation of Au is not expected. The contact resistance to graphene for the Ti/Nb and Ti/Au/Nb electrodes was 400 and 700 Ω, respectively, with a contact area of approximately 1.3μm^2. Because their channel resistance was several kΩ and the as made graphene channel was heavily doped, they concluded that much of the channel resistance was due to a transition region between the edge of the electrode/graphene contact area and the graphene channel. They suggest that stress in the NbTiN film or the RF cleaning process could damage the graphene area around the superconducting electrodes creating

a defected G' region. With this non-optimized electrode configuration they were still able to observe a full proximity effect in some devices with channel lengths up to 400 nm although with a very small critical current of a few nA. Because of the poor transparency of the contacts and G' region, they were unable to investigate Andreev reflection or the quantum Hall regime.

Ojeda-Aristizabal *et al* clearly demonstrated the importance of graphene-superconductor contact by tuning the proximity effect *in situ* via current annealing[167]. Sputtered electrodes consisting of Pt/Ta/Pt were utilized on an exfoliated graphene flake. The channel length and width were 330 nm and 2.7 μm, respectively. All measurements were performed at 60 mK in a dilution refrigerator. Data is presented before current annealing and after three different current annealing steps. The first current annealing step was performed by applying a 3 mA current through the sample for 3 minutes. This corresponds to a current density of 2×10^8 A/cm^2 if the graphene thickness is taken to be 0.36 nm. The second and third current annealing steps utilized 6 and 10 mA, respectively. A full proximity effect was finally achieved after the third annealing step. They found that the annealing improved the graphene/superconductor interface, increased the mean free path of the carriers, and increased the doping. Evidence of multiple Andreev reflections was visible in the differential resistance curves for all conditions but became clearer with each annealing step. A switching current of $I_S = 480 - 720\ nA$ and a normal resistance of $R_N = 80 - 105\ \Omega$ were measured in the I-V curve after the third annealing step, depending on gate voltage. Given the ratio of the channel length to coherence length, the theoretical value of $R_N I_S = 1.3\Delta_0/q$ for a perfect interface is 6 times higher than measured, indicating that the interface is still not highly transparent.

Arguably the best proximity effect result was obtained by Jeong *et al* in PbIn-graphene-PbIn junctions[164]. They utilized a thermally deposited $Pb_{1-x}In_x$ alloy instead of pure Pb in order to

minimize the granularity of the electrodes. Because the electrodes were thermally deposited, the energy of the particles incident on the graphene should be sufficiently low to avoid causing damage to the graphene lattice. The contact resistance obtained from three probe measurements was in the range of 1 – 15 $\Omega \cdot \mu m^2$ and was insensitive to temperature change. The electrodes were 900 nm wide, and the graphene channel length was 300 nm. A switching current of 3.0 μA was measured, which is significantly higher than other reports. The incorporation of 7% indium only reduced the critical temperature by 0.2 K. The critical temperature of the electrode material was 7.0 K, and a full proximity effect existed up to 4.8 K, which is above the temperature of liquid helium and the highest reported to date. It is highly likely that the low contact resistance between graphene and PbIn is responsible for these superior results. If Nb-graphene junctions could be optimize, they may potentially be able to improve upon this system by further increasing the proximity effect's temperature range and offering a higher critical magnetic field. There is still much need for improvement if graphene is to be used in quantum information devices and gate-tunable Josephson junction devices.

So far nearly every report claims a lower than desired transparency, indicating that there is much work to do on the graphene-superconductor interface. Additionally, no one has yet been able to definitively observe specular Andreev reflection in *SGS* junctions. One possible reason is that the spatial inhomogeneities in the Fermi energy are larger than Δ_0. The Δ_0 for Al electrodes is 180 μV[159], and that for Nb electrodes is 1.4 mV[170]. While the value for Nb is much larger than Al, it is still smaller than the typical Fermi energy scale associated with spatial carrier density fluctuations around the Dirac point[175]. A combination of superconducting electrodes with a larger energy gap and clean graphene with homogeneous doping is needed to observe this phenomenon. It may be possible to observe the suppressed supercurrent due to specular Andreev

reflection in the regime where the graphene channel breaks down into electron and hole puddles since a fraction of them may have a very low carrier density corresponding to a Fermi energy less than Δ_0[171]. In this scenario, transport of Andreev pairs occurs through a series of puddles with various charge densities. If one of them satisfies the condition of an effective Fermi energy less than Δ_0, then specular Andreev reflection could occur on the boundary of that puddle.

5.3 Preliminary Studies

5.3.1 Sample fabrication

Graphene flakes were deposited onto clean, dry, heavily doped Si/SiO_2 chips with 90 nm oxide via the Scotch tape method. The heavily doped Si was used as a back gate. The tape was allowed to rest on the chip overnight to allow the graphene/tape/SiO_2 system to relax and to allow graphene to adhere well to the SiO_2. Upon peeling of the tape, the chip was immediately soaked in acetone for five minutes to remove tape residue, rinsed in isopropyl alcohol, and blown dry with dry nitrogen gas. This process produces a random graphitic debris field which contains graphene flakes of various sizes and thicknesses. Graphene flakes were identified relative to predefined, recessed alignment markers using optical microscopy. By examining the contrast[176], flakes with thickness of one to a few layers were chosen. Two closely spaced electrodes were patterned on the flakes with electron beam lithography (EBL) utilizing a bilayer resist stack of MMA-MAA and PMMA to facilitate liftoff. Each electrode split off into two contact pads. Electrodes were deposited by sputtering in a homemade sputtering chamber with base pressure of $< 5 \times 10^{-7}$ Torr and a load lock.

Electrodes either consisted of Nb only, Ti/Nb, or Pd/Nb. Some devices were capped with another 20 nm Pd in order to protect the Nb from oxidation and facilitate probing in a probe

station. This will be discussed further below. The deposition of Ti and Pd will be discussed below as well. The Nb deposition had been optimized for another project to have high critical temperature and low resistivity. Nb was deposited fairly quickly, with a rate of ~ 1.7 nm/s, using RF sputtering at 330 W (corresponding to ~ 180 V) with 14 mTorr Ar sputtering gas. Either 80 or 200 nm Nb was used. When 200 nm was used, the deposition was split into two steps. The stage was water cooled to ~ 8 °C. Following deposition the chip was allowed to sit in the sputtering chamber in flowing Ar for at least 10 minutes to cool down. The water cooling was then turned off and the sample was moved to the load lock and allowed to warm up for at least 30 minutes at ~ 10^{-5} Torr. It was found that if this was not done, the Pd film could crack and peel from the substrate.

5.3.2 Findings

The first devices fabricated for this project consisted of thin film graphite (estimated > 20 layers) with 200 nm Nb sputtered directly onto the graphite. We fabricated a large electrode pattern with a 1 mm × 400 μm window for flake deposition on the Si/SiO_2 chip with photolithography. At this early time we were unable to obtain few layer or thinner graphene flakes for two reasons. First, the small area for graphene flake deposition decreased the chances of finding very thin flakes. Second, processing the chips by photolithography inevitably left a thin polymer residue which could inhibit adhesion of very thin flakes due to reduced Van der Waals forces. The devices fabricated in this batch were characterized at room temperature and showed a small contact resistance of less than 100 Ω but no detectible field effect. The lack of a field effect should be expected due to the screening effect mentioned in Section 5.1.3. At the time not much was thought of the low contact resistance because it was the first graphene device

we had fabricated and we had no first hand comparison. As mentioned in Section 5.2.2, direct sputtering of Nb onto graphene should cause serious damage to graphene. We were initially unaware of this, but our result should also be expected. Because the flakes had so many layers, damage to the top few layers would simply result in contact to the subsurface layers. We may have even been able to contact several layers at once. These devices were not measured at low temperature because of the lack of field effect.

The second batch of devices utilized chips provided by Professor Chiu prior to her arrival at the University of Kansas. Following her instruction we were able to obtain single and few layer graphene flakes easily. Again, Nb was sputtered directly onto the graphene. These devices were found to have huge contact resistance on the order of $10^5 – 10^6$ Ω. No field effect was observable because the contact resistance was several orders of magnitude higher than the graphene channel resistance. These devices were not characterized at low temperature and will not be discussed further.

Following the observation of huge contact resistance between graphene and Nb, we decided to utilize a 10 nm titanium layer between graphene and Nb following the report of Heersche *et al*[159]. Titanium was sputtered at 90 W with 14 mTorr Ar sputtering gas. In order to obtain a reasonable contact resistance it was necessary to quickly deposit the Ti and minimize the time between Ti and Nb sputtering. Oxidation of Ti was suspected to be a problem. Two sets of devices were characterized: one with 3 nm Ti and one with 10 nm Ti. All devices had channel lengths designed to be 1 μm. The actual channel length was closer to 700 – 800 nm due to the effects of sputtering, which will be discussed in Section 5.4. The thickness and channel width varied from flake to flake. All devices were baked together at 400 K overnight in the probe station with pressure ~ 5×10^{-6} Torr in order to reduce doping due to adsorbants and allowed to

cool slowly before measurement. I-V and I-V_G curves were measured with a semiconductor analyzer using the sample stage as a global back gate.

The devices showed a wide range of behaviors. The first variation came with regard to the response to current annealing. As made, three out of four devices with 3 nm Ti had nonlinear I-V curves with resistance of $10^5 – 10^6$ Ω. This high resistance is assumed to be due to the contact, since the short graphene channel should have resistance of $10^2 – 10^3$ Ω, depending on width and number of layers. One device had a linear I-V curve and resistance of ~ 19 kΩ. Current annealing was applied to all devices. Current annealing was performed by sweeping the source-drain voltage forward and back with increasing maximum voltage until a change is observed and there is no more hysteresis. This method can be used to improve contact by generating heat to anneal the contact or breaking through a contamination or oxide barrier layer. The three devices with high initial resistance responded to current annealing and stabilized with resistance of 10^3 Ω and a linear I-V.

The devices with 10 nm Ti also displayed a range of behaviors. Two devices had resistance of 10^7 Ω (again assumed to be due to contact) and did not respond to current annealing, two devices had a linear I-V and resistance of 10^3 Ω as made, and one device had a resistance in the high 10^4 Ω range and responded to current annealing to stabilize in the low 10^4 Ω range. The four types of responses to current annealing are given in Figure 5.4. The reason for the huge variation in as-made contact condition and response to current annealing between devices on each chip is unknown at this time. All 3 nm Ti devices were fabricated on the same chip, and all 10 nm Ti devices were fabricated on a second chip. Since all devices on a given chip were fabricated and measured under the same conditions they are not expected to vary much, yet we observe a huge variation. The chip size of ~ 1 cm^2 is small compared to the

sputtering sample stage and sputtering plasma cross-sectional area, suggesting that the sputtering conditions do not vary much from one position on the chip to another. Additionally, the electron beam was focused ~ 150 μm away from each device immediately prior to pattern writing, so the amount of MMA-MAA remaining on each flake's contact interface should be similar. Monolayer and bilayer flakes were roughly evenly represented in each batch, and there was no trend related to layer number. The sample size, however, was fairly small, making such a generalization less meaningful.

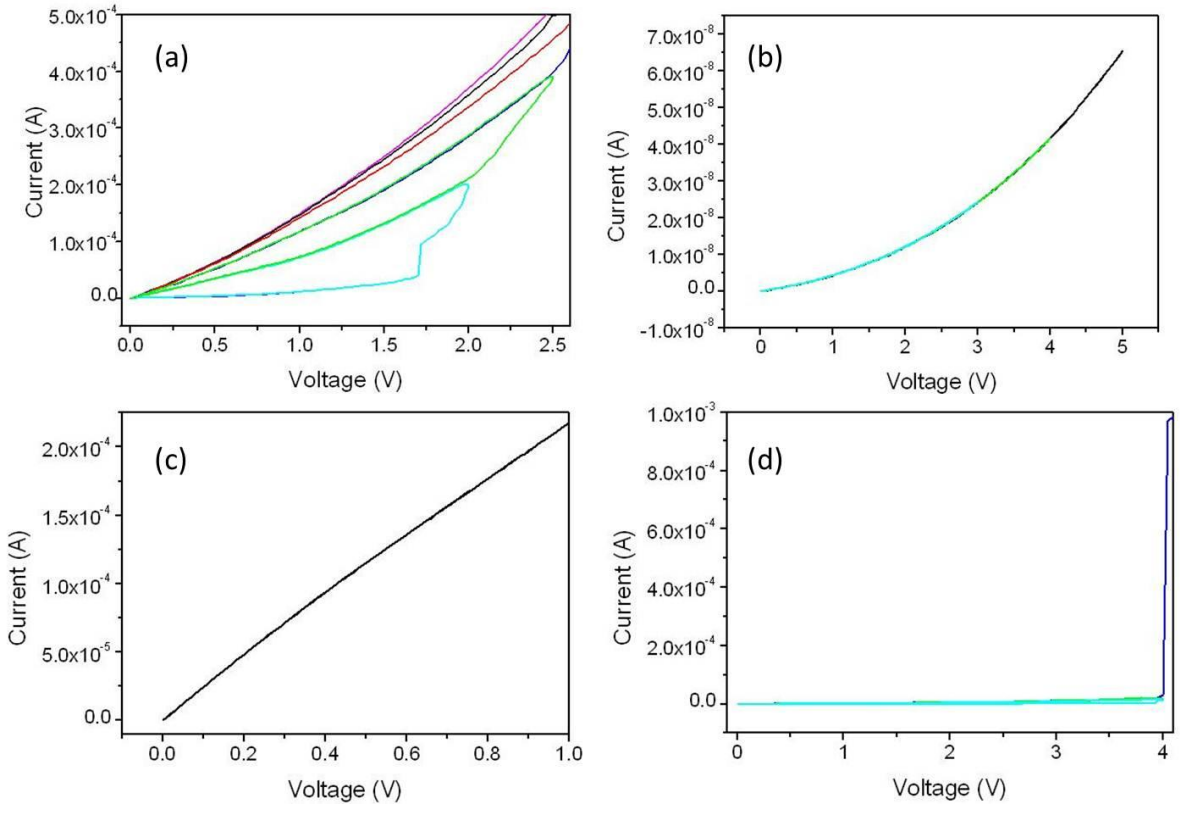

Figure 5.4: Examples of responses of graphene-Ti-Nb devices to current annealing. (a) A sequential improvement with increasing source-drain voltage until the hysteresis is eliminated. (b) Device has high resistance and a non-linear I-V curve which does not respond to current annealing. All sweeps exactly retrace each other. (c) As made device has a roughly linear I-V and low resistance. These devices did not respond to current annealing. (d) A quick, sharp decrease in resistance at high source-drain voltage.

Despite the overnight baking, all devices were doped n-type with the Dirac point, or charge neutrality point, between -10 V and – 25 V back gate voltage. Given this acceptable gate voltage range, we attempted to measure these devices at low temperature in the probe station, which can be cooled down to ~ 2 K using flowing liquid helium. The probe station was outfitted with W and BeCu probes with 10 or 25 μm probe tip widths. In order to make contact to the pads, the probes are first moved into position with XYZ micrometer driven manipulators and then slowly moved downward until the probe contacts the pad and slides slightly forward as viewed through a microscope above the stage, indicating contact has occurred. At room temperature Nb-probe contact was straightforward and introduced ~ 50 Ω per probe. In order to measure the devices at low temperature, the probes must be lifted a few millimeters above the stage during cooling to allow for thermal contraction of various components. Once base temperature was reached we ran into significant difficulties contacting the Nb pads.

At 4.2 K there was a significant barrier between the probe tip and Nb, regardless of which probe material or diameter was used. When two probes were places very close to each other in the same pad, the circuit appeared open and only fA current could be driven through. When the probes touched each other directly they were clearly shorted, suggesting that the probes and electronics were not to blame. Occasionally the current would be able to break through the Nb-probe barrier at ~ 1 V bias, albeit intermittently. The problems persisted even when the samples were warmed up to 100 K, but at room temperature the devices returned to their original state. Interestingly, when the devices were later cooled down with liquid nitrogen to 77 K, there was no problem contacting the pads. This suggests that at low temperature there could be a phase change which occurs at liquid helium temperature and persists during warming to 100 K but does

not occur when cooling from room temperature to 77 K. The reason for this observation is unknown at this time.

It was also observed that the Nb became brittle at low temperature and could easily be broken by the probes. A scanning electron microscope image of the Nb pad after measurement at room temperature and liquid helium temperature is shown below in Figure 5.5. The gentle scratch from room temperature probing is marked in the bottom half of the image. The probe produces a small indentation in the metal but does not break through. The result of the 4.2 K probing is marked in the top half of the image. The dark region is the underlying SiO_2. The difference between the room and low temperature probing is clear.

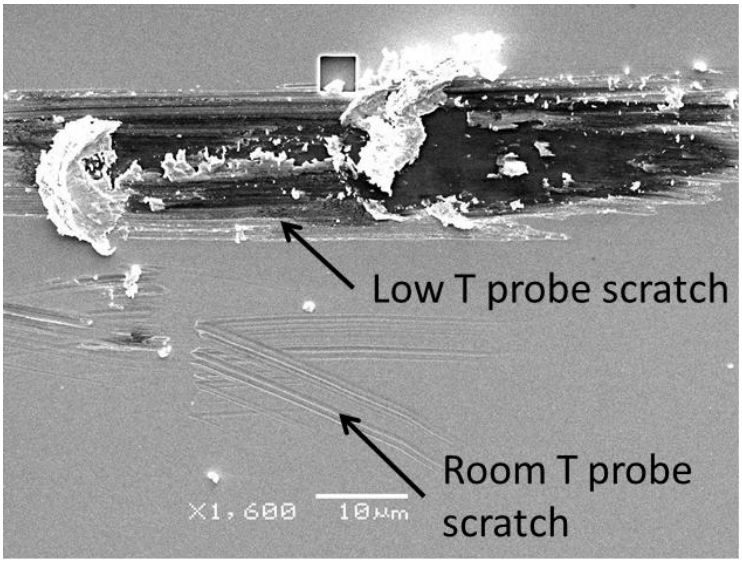

Figure 5.5: Scanning electron micrograph of Nb contact pad after probe station measurement at room temperature and 4.2 K. The resulting scratches from probing at each temperature are marked. The dark area in the upper scratch is exposed SiO_2, indicating that Nb has been completely removed from the chip.

Motivated by the poor contact between Ti and graphene as well as between Nb and the probes, we decided to try a sputtered Pd/Nb/Pd (8/80/20 nm) electrode stack. Pd has been shown to make better contact to graphene than titanium[177], and it has also been used to protect Nb films

from oxidation, indicating that Pd and Nb may not have any inherent incompatibility. The Pd was sputtered at 50 mTorr and 190 V in an attempt to reduce the energy and mean free path of the plasma ions and Pd particles with the intention of reducing damage to the graphene. Again the devices were baked overnight in vacuum at 400 K and had ~ 1 μm channel length and varying channel width and graphene layer number depending on the flake. Nine devices were fabricated with an as-made two probe resistance of 400 – 1000 Ω, including both channel and contact resistances. All devices had linear I-V curves and did not require current annealing. This represents a significant improvement over the Ti/Nb devices. Interestingly, three devices had a Dirac point near 5 – 10 V while the remaining devices were heavily doped with Dirac points > 30 V. In two cases adjacent devices fabricated on the same flake had Dirac points > 20 V apart. Again, the reason for this variation in devices on the same chip is unknown at this time. Based on two four probe devices on the chip, the contact resistance per electrode is estimated to be 200 Ω, corresponding to ~ 1400 Ω·μm^2. An example I-V_G curve is shown here in Figure 5.6. This monolayer graphene device had a channel width of 4.1 μm, channel length of 700 nm, and had a Dirac point of ~ 6 V. The p-branch appears to have a lower conductivity than the n-branch, which is typical of Pd-graphene contacts[177].

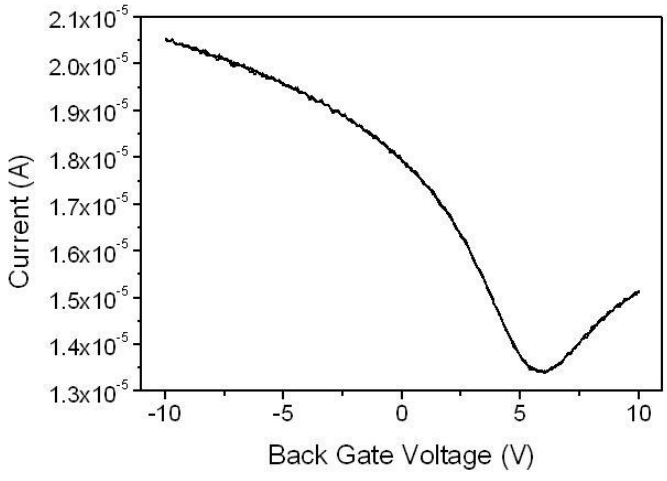

Figure 5.6: I-V_G curve of graphene device with Pd/Nb/Pd electrodes. Source-drain voltage was 10 mV, and gate voltage was applied via back gate with 90 nm SiO_2.

By comparison, our devices with the Ti adhesion layer required current annealing in 80% of cases, while devices with Pd did not require current annealing in any case. Additionally, some Ti devices could not be improved with current annealing and retained a MΩ contact resistance. The contact resistance for Pd devices was 1-2 orders of magnitude lower than that of the best Ti devices. Additionally, Ti devices were heavily n-doped while Pd devices were heavily p-doped, despite identical measurement conditions. The graphene/Pd/Nb devices presented above represent a significant improvement over the reported work on graphene – Pd/Nb devices by Komatsu *et al*[170] in which they report a contact resistance to channel resistance ratio of ~ 5. The corresponding ratio for our Pd/Nb devices is estimated to be ~ 2. The contact resistance we obtained was still 2 – 3 orders of magnitude higher than that of the best reported on graphene-superconductor devices, mentioned above to be 1 – 15 $\Omega \cdot \mu m^2$ for graphene – PbIn devices[164].

In an attempt to reduce the contact resistance by further reducing possible damage to graphene, we increased the sputtering pressure of the bottom Pd layer to 100 mTorr. This was

expected to further reduce the mean free path and energy of the sputtering ions and Pd particles, hopefully making the deposition gentler. Again, no current annealing was necessary since all as-made devices had linear I-V curves and resistances in the kΩ range. The contact resistance was found to be ~ 1 kΩ, almost an order of magnitude higher than the 50 mTorr Pd devices. Interestingly, all 6 devices had very broad I-V_G curves with Dirac points between 0 and 10 V, including the monolayer devices. A typical monolayer graphene I-V_G curve is shown below in Figure 5.7.

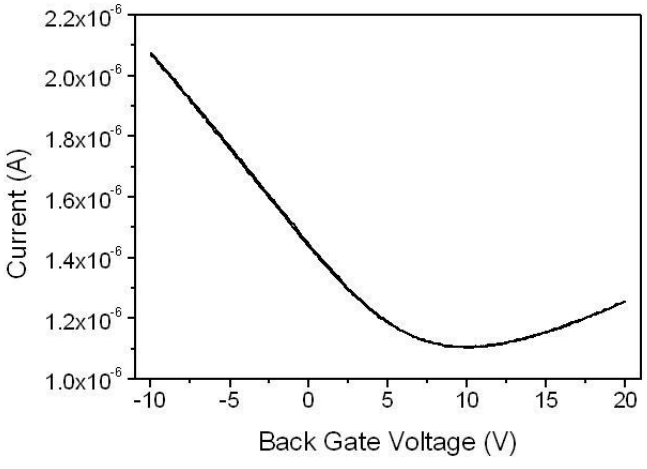

Figure 5.7: Typical I-V_G curve of a monolayer graphene device with Pd/Nb/Pd electrodes where Pd was deposited at 100 mTorr sputtering pressure.

Compared to the previous figure, this curve is much broader even though both were on monolayer graphene devices. The reason for this is not understood at this time.

In another attempt to optimize the graphene-Pd contact, we fabricated another batch of devices using an electron beam evaporated bottom Pd layer. 10 nm Pd were deposited with electron beam evaporation at 10^{-6} Torr. The chip was then transferred quickly through the air into the load lock chamber of the sputtering system. There it underwent a gentle oxygen plasma

cleaning to remove any adsorbed molecules from the Pd surface. This was followed by sputtering of Nb and Pd (80 and 20 nm) following the regular procedure. The as-made devices were heavily doped p-type, but appeared similar to the 50 mTorr sputtered Pd devices. Unfortunately the four probe device did not survive processing, so contact resistance could not be measured. Based on flake geometry and layer number, the contact resistance was estimated to be on the order of 1 kΩ. Thermal annealing in vacuum seemed to improve the contact only slightly. Further discussion on contact resistance is given in Section 5.4. Based on that discussion, it will seem unsurprising that this contact resistance was no better than that of the 50 mTorr sputtered Pd.

We attempted to measure the above devices at liquid helium temperature again in the probe station. We also mounted a Nb Josephson junction (JJ) as a standard sample to ensure that the Nb was superconducting and the electronics were working properly. Probe contact to the Nb was again an issue. We were able to contact the Nb JJ only by placing the probes on the feet of the Al bonding wires which remained from previous wire bonding to the chip. We found that the Nb Josephson junction could not be measured because the extrinsic noise in the system was too high to localize the phase difference across the junction, even after powering off all possible instruments.

We then attempted to measure the devices using a low temperature probe designed for superconductor measurements. This probe requires that the chip be wired to a holder via wire bonding or manual bonding with silver paste or indium. Manual wiring was out of the question due to the small size and proximity of the contact pads. The field of view of the scanning electron microscope used for electron beam lithography limits the contact pad size greatly. Unfortunately, wire bonding proved to be a great challenge. The wire bonder had broken in the

past year, and its repair left many parameters off from their optimal settings. The bonder tended to provide too much force and break the oxide, shorting the pads through the heavily doped silicon. This makes measuring the device extremely difficult. Even if the severity of the short could be reduced to 1 MΩ, applying a gate voltage would induce severe leakage which would ruin the measurement. We attempted to bond on 300 nm oxide coated with 200 nm Nb, but the shorts persisted. After a combined total of over a month of optimizing the wire bonder, the two precious resources of time and liquid helium both ran out. There is a plan in place now to pattern larger pads on the chip with photolithography and connect the devices to them with electron beam lithography so that the chip can be wired manually. Unfortunately there was not enough time for me to follow through on this plan.

5.4 Summary and Future Work

To summarize, this work intended to study the superconducting proximity effect in graphene-Nb junctions. We are as of yet unable to achieve this goal, yet we did make headway in troubleshooting several fabrication issues, especially the graphene-superconductor contact. We found that contact to graphene and the resulting electronic properties of the graphene device depend critically on the electrode material and deposition conditions. We also found that one to few layer graphene can in fact be easily damaged by sputtering if care is not taken to ensure the sputtering is gentle enough. The above findings are an essential step if a full proximity effect in graphene-Nb junctions at liquid helium temperature is to be achieved.

Much of the work done was with the goal of reducing the contact resistance to graphene by minimizing damage to graphene during Pd sputtering. Another possible method to further reduce contact resistance could be to improve Pd morphology by increasing the grain size[177].

Thermally annealing our devices in vacuum at 400 °C had no effect on contact resistance, however. Optimizing the Pd deposition or post deposition annealing conditions further or searching for an alloy which forms large grains could possibly help to improve the contact resistance. There is evidence, however, that if damage to graphene can be avoided then the factor most responsible for high contact resistance to graphene is contamination from resist residue. Robinson *et al* were able to achieve specific contact resistance of 10^{-1} $\Omega \cdot \mu m^2$ by gently cleaning the exposed graphene in the contact window with a low power oxygen plasma followed by a thermal anneal at 450 °C to further remove residue before depositing metal[178]. This is something that could be considered by anyone pursuing this work in the future. Data from Robinson *et al* did show that some of graphene's C-C bonds were replaced with C-O bonds, and the 2D Raman peak was degraded, indicating that the treated graphene under the electrode has been chemically altered. It is unknown whether or not this would affect the superconducting proximity effect, but it would be interesting to study.

Since the focus on this project has been on optimizing the electrode material, deposition conditions, and experimental conditions, work has not yet been done to optimize other fabrication steps. One such step is making the EBL process more suitable for sputtering, which is necessary to deposit Nb. During sputtering three major issues arise which are unique from electron beam evaporation, which is the preferred deposition method. The first is heating. The PMMA can heat up and cross-link, making it insoluble in acetone and rendering liftoff impossible. This problem has already been alleviated by using a water-cooled sample stage during sputtering. The second issue is the rounding of EBL-defined features in the PMMA due to high energy bombardment with ions in the plasma and sputtered atoms. This takes a level of control away by making all patterned features less sharp and more rounded. The third issue is a

geometrical one. Sputtering deposits atoms through a range of incident angles which causes metal to be deposited into the undercut induced by the bilayer resist structure, as shown in Figure 5.N(b), below. This gives less control over the channel length and can even connect electrodes across short channels. As can be seen, the bilayer resist is used to facilitate liftoff. If a single layer is used, metal may coat the sidewall of the EBL-defined feature and block the solvent from removing the PMMA mask, as shown in Figure 5.N(a). A trilayer resist stack, as shown in Figure 5.N(c) may alleviate this problem and reduce the severity of feature rounding.

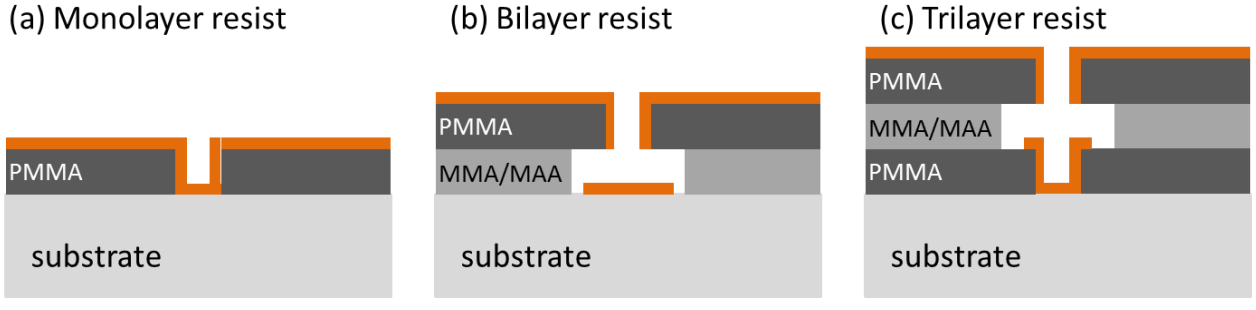

Figure 5.8: Schematic of (a) single layer, (b) bilayer, and (c) trilayer electron beam resist with undercut in the MMA/MAA and metal deposition area shown.

My recommendation for anyone continuing this project is to adopt the trilayer resist structure. This may, however, cause an increase in the amount of polymer residue left on the graphene flakes after liftoff. This will have to be addressed with a more thorough hot acetone rinse, hydrogen/argon annealing, or a longer and/or higher temperature anneal in vacuum, if feasible.

Looking forward, there are other fabrication issues which can be anticipated in future experiments. As mentioned above, it would be interesting to study the *SGS* junction in the quantum Hall regime. This is of course not as simple as it sounds. In order to study the transport properties of a *SGS* junction in the quantum Hall regime, large magnetic fields are needed. However, the necessity of superconducting leads limits the usable strength of the magnetic field.

This implies that very high mobility samples are needed so that the necessary magnetic field can be minimized. In order to achieve the highest possible mobility, suspended exfoliated graphene flakes must be utilized. As mentioned above, the typical SiO_2/Si substrate surfaces contain impurities and trapped charges which scatter charge carriers in graphene and reduce the mobility of the sample. An additional complication arises due to the fact that niobium can be etched by hydrofluoric acid, the standard etchant used to suspend graphene devices. One option is to prepare graphene flakes on a film of PMMA or another polymer, identify the desired flakes, and then remove the polymer/graphene film and position the desired flake on top of predefined trenches in another substrate. This may introduce another problem, however. When PMMA is spun on a chip with graphene flakes, it is easy for the flakes to roll up and become unusable. While it has not been tested in this project, it is reasonable to suspect that this problem could be much worse for flakes suspended over trenches due to reduced adhesive forces between the flake and substrate.

Another fabrication hurdle is the possible need to avoid heat treatments of the device. It is clear from the previous sections that highly transparent electrodes are necessary for the proposed experiments. As mentioned above, one method to improve contact is through current annealing. This may heat up the graphene as well as the contact interface. Additionally, it may be desired to heat the device with a heater in order to remove adsorbed molecules and polymer residue from the surface, improving the mobility and reducing the doping level. Bao *et al* found that heating suspended graphene flakes, however, induces significant rippling which can scatter charges and reduce mobility[119].This rippling may be responsible for the disappearance of quantum Hall features in suspended graphene flakes which underwent annealing[179].

Chapter 6

Summary and Outlook

This dissertation focuses on the correlation of microstructure in carbon-based nanostructures with optoelectronic properties. Carbon-based nanostructures, namely graphene and the various forms of carbon nanotubes, are especially interesting to study due to their exceptional electronic, optical, thermal, and structural properties. These unique properties have led to intense investigation of graphene and carbon nanotubes for both the benefit of fundamental physics and technological applications such as solar cells, sensors, and electronic components. Despite great theoretical predictions, many devices fabricated from carbon nanotubes and graphene have performed poorly or been unable to compete with their conventional counterparts. In most cases, the reason for this is a lack of understanding or control over the microstructure of the material or device.

Here, the term *microstructure* refers generally to the details of the construction of a material or device relevant to nanoscience. That is, for example, how the atoms or grains are arranged, the nature of the surfaces and interfaces, how the material interacts with the environment, the presence of defect structures, and the geometry of a nanoscale device, to name a few. Given this working definition, correlating microstructure with device-relevant optical or electronic properties is of utmost importance to nanotechnology due to the nature of nanoscale materials and devices. In nanoscale materials and devices, critical processes such as charge transport, metal contact, and photon absorption are extremely sensitive to microstructure. Compounding this issue are the facts that as-grown nanostructures are very rarely as perfect as is

desired, and nanofabrication techniques can introduce complicating factors to the device. Because of this, correlating microstructure and optoelectronic properties is the only way to fully exploit the unique properties available to us in carbon-based nanostructures such as graphene and carbon nanotubes.

The work presented above in this dissertation provided four examples of this way of thinking. The first project dealt with core-shell carbon nanofiber/TiO_2 nanowires which were developed for use in a novel dye-sensitized solar cell design. The carbon nanofiber provided a conductive, ordered route for electrons to the anode while the nanoneedle structured TiO_2 provided a high surface area for dye adsorption, accepted photo-excited electrons from the dye, and transferred them to the carbon nanofiber. A dye-sensitized solar cell constructed from the as-grown nanowires yielded a low short circuit current leading to an efficiency one order of magnitude lower than the original nanoparticle-based solar cell. By studying the optoelectronic properties of the nanowires and correlating it with microstructure as determined by transmission electron microscopy and annealing studies, we were able to determine the reason for the poor performance and a method for improvement. It was observed that as-grown nanowires were nanocrystalline with a significant amorphous TiO_2 presence and a high density of oxygen vacancies, leading to sub-bandgap photon absorption by the TiO_2, a surface unsuitable for dye adsorption, significant charge trapping, and instability in the electrolyte. By improving the TiO_2 microstructure by thermal annealing in air, we were able to improve all of the above problems. Our collaborators have not yet fabricated a solar cell out of the annealed nanowires, so we do not yet know the effect of these improvements on the solar cell figures of merit. A proposed future project is to fabricate a single nanowire dye-sensitized solar cell from as-grown and annealed nanowires to probe this directly.

The second project in this dissertation is an individual multiwall carbon nanotube infrared sensor. A series of publications by Rongtao Lu *et al* on carbon nanotube film IR sensors led to the understanding that thermal link between the nanotube and the substrate as well as intertube junctions were the primary limiting factors of the performance of the film-based sensors. This provided the motivation to study an individual multiwall carbon nanotube IR sensor. The inner shells of MWNTs are naturally suspended due to poor electrical and thermal conduction in the radial direction compared to the axial direction, and an individual MWNT device does contain any intertube junctions. Individual MWNT device studies found that electrode material and geometry was absolutely critical to obtaining a measurable photoresponse. The optimized configuration is a Ti/Au Schottky contact with one electrode on the sidewall and one electrode over the end of the MWNT. The Schottky contact provides a poorer thermal link than an Ohmic contact as well as a barrier to limit the current in the absence of IR photons. The electrode on the sidewall electrically contacts only the outer one to few shells, but the electrode on the end contacts all shells. This means that the photocurrent generated at each Schottky contact does not cancel. The photodetection mechanism of the individual MWNT with asymmetric Schottky contacts differs greatly from the bolometric response of the large area MWNT and SWNT film sensors in which photon absorption produces excitons which relax before they can be separated and give their energy as heat to the lattice, reducing the resistance of the film. The proposed mechanism in the individual MWNT is a non-cancelling thermally assisted exciton dissociation at the Schottky contacts which is enhanced by the poor thermal link to the environment. The resulting device has low noise and is extremely sensitive. The specific detectivity is greater than conventional vanadium oxide IR sensors, making CNT competitive for IR detection for the first time.

The third project aimed to correlate defect structure with carrier diffusion in graphene grown by chemical vapor deposition. Large area graphene films are needed if graphene is to become viable in commercial electronic devices such as touch screens and solar cells. Growth of graphene by CVD on copper is especially promising, but the resulting films suffer from grain boundaries due to the coalescence of grains during growth, wrinkles due to the difference in thermal expansion coefficients of graphene and copper, and creases due to transfer of the films to the desired substrate. All three of these defect structures affect the electronic properties and must be better understood. The structure and properties of wrinkles and creases was studied with Raman spectroscopy, a very powerful tool for characterizing graphene. It was found that the wrinkles may have an unexpected doping profile compared to the surrounding graphene, and the creases have a complex, spatially varying structure. The effect of wrinkles and creases on carrier diffusion was then studied using optical techniques in order to avoid the complications inevitably arising from nanofabrication of electrodes and etching the film. It was found that wrinkles and creases both affect diffusion of carriers by reducing the diffusion coefficient by as much as 50%. They do this by increasing carrier scattering and decreasing the mean free path. They also appear to have comparable effects, despite their difference in size and origin. A slower diffusion was observed for longer times at all studied positions on the film. The origin of this slow diffusion is not well understood at this point, but may be due to extrinsic factors such as contamination on the film based on previous studies which found that it could be removed with laser heating. Further studies are proposed to examine this effect and determine if it is in fact extrinsic to graphene or if it represents some as yet unknown physics.

The fourth project presented in this dissertation dealt with obtaining a suitable contact to graphene with Nb in order to eventually study the superconducting proximity effect in graphene.

Nb-graphene is an interesting system to study because the critical temperature of Nb is well above liquid helium temperature, which leads to a higher I_cR product and makes experimental work more convenient. Additionally, Nb has a high critical field, which may enable the investigation of a supercurrent in graphene in the quantum Hall regime. This project was not able to reach the point of measuring the proximity effect in graphene-Nb junctions. We did, however, make some progress in optimizing the graphene-superconductor interface. This interface is absolutely critical for studying the proximity effect and its associated phenomena in graphene, as evidenced by the limitations of the previously reported work which was almost unanimously attributed to contact quality. We found that depositing Nb directly onto graphene resulted in 10^5 – 10^6 $\Omega \cdot \mu m^2$ specific contact resistance due to damage to graphene by the high energy sputtering process necessary to obtain acceptable Nb films. Contact resistance can be improved to 10^2 Ω by a relatively high pressure sputtering of ~ 8 nm Pd before Nb sputtering. The higher pressure sputtering reduces the energy and mean free path of the ions and Pd particles, reducing damage to graphene. The finally obtained contact resistance is near the middle of the reported values for graphene-superconductor systems, suggesting that a full superconducting proximity effect should be attainable, but it is still ~ 2 orders of magnitude higher than desired.

All four projects described in this dissertation demonstrate the critical importance of correlating microstructure with optical and electronic properties as a means to advance nanoscience. This approach and mindset are necessary if one is to fabricate devices utilizing carbon-based nanostructures which fully exploit the unique properties of the nanostructures instead of mask them. Ideally this process would be part of a feedback loop in which adjustments to growth and device fabrication are motivated by this correlation, and the process repeats until the device or material is fully optimized.

References

1. Krueger, P. D. A. *Carbon Materials and Nanotechnology*. (Wiley-VCH: 2010).
2. Kroto, H. W., Heath, J. R., O'Brien, S. C., Curl, R. F. & Smalley, R. E. C60: Buckminsterfullerene. *Nature* **318**, 162–163 (1985).
3. Iijima, S. Helical microtubules of graphitic carbon. *Nature* **354**, 56–58 (1991).
4. Pop, E., Mann, D., Wang, Q., Goodson, K. & Dai, H. Thermal Conductance of an Individual Single-Wall Carbon Nanotube above Room Temperature. *Nano Lett.* **6**, 96–100 (2005).
5. Sinha, S., Barjami, S., Iannacchione, G., Schwab, A. & Muench, G. Off-axis Thermal Properties of Carbon Nanotube Films. *Journal of Nanoparticle Research* **7**, 651–657 (2005).
6. Yu, M.-F. *et al.* Strength and Breaking Mechanism of Multiwalled Carbon Nanotubes Under Tensile Load. *Science* **287**, 637–640 (2000).
7. Treacy, M. M. J., Ebbesen, T. W. & Gibson, J. M. Exceptionally high Young's modulus observed for individual carbon nanotubes. *Nature* **381**, 678–680 (1996).
8. Novoselov, K. S. *et al.* Electric Field Effect in Atomically Thin Carbon Films. *Science* **306**, 666–669 (2004).
9. Lee, C., Wei, X., Kysar, J. W. & Hone, J. Measurement of the Elastic Properties and Intrinsic Strength of Monolayer Graphene. *Science* **321**, 385–388 (2008).
10. Murali, R., Yang, Y., Brenner, K., Beck, T. & Meindl, J. D. Breakdown current density of graphene nanoribbons. *Applied Physics Letters* **94**, 243114–243114–3 (2009).

11. Chen, J.-H., Jang, C., Xiao, S., Ishigami, M. & Fuhrer, M. S. Intrinsic and extrinsic performance limits of graphene devices on SiO2. *Nature Nanotechnology* **3**, 206–209 (2008).

12. Bunch, J. S. *et al.* Impermeable Atomic Membranes from Graphene Sheets. *Nano Lett.* **8**, 2458–2462 (2008).

13. The 2010 Nobel Prize in Physics - Press Release.

14. Zhu, H., Wei, J., Wang, K. & Wu, D. Applications of carbon materials in photovoltaic solar cells. *Sol. Energy Mater. Sol. Cells* **93**, 1461–1470 (2009).

15. Ratier, B., Nunzi, J.-M., Aldissi, M., Kraft, T. M. & Buncel, E. Organic solar cell materials and active layer designs-improvements with carbon nanotubes: a review. *Polym. Int.* **61**, 342–354 (2012).

16. Wang, Y. & Yeow, J. T. W. A Review of Carbon Nanotubes-Based Gas Sensors. *Journal of Sensors* **2009**, 1–24 (2009).

17. Liu, L. & Zhang, Y. Multi-wall carbon nanotube as a new infrared detected material. *Sensors and Actuators A: Physical* **116**, 394–397 (2004).

18. Xia, F., Mueller, T., Lin, Y., Valdes-Garcia, A. & Avouris, P. Ultrafast graphene photodetector. *Nature Nanotechnology* **4**, 839–843 (2009).

19. Schwierz, F. Graphene transistors. *Nature Nanotechnology* **5**, 487–496 (2010).

20. Geim, A. K. & Novoselov, K. S. The rise of graphene. *Nature Materials* **6**, 183–191 (2007).

21. Benjamin, C. & Pachos, J. K. π junction qubit in monolayer graphene. *Phys. Rev. B* **79**, 155431 (2009).

22. N. S. Lewis, George Crabtree, Arthur J. Nozik, Michael R. Wasielewski & Paul Alivisatos Basic Research Needs for Solar Energy Utilization. *Report of the Basic Energy Science Workshop on Solar Energy Utilization* (2005).

23. Luque, A. & Hegedus, S. *Handbook of Photovoltaic Science and Engineering*. (Wiley: 2003).

24. Shockley, W. & Read, W. T. Statistics of the Recombinations of Holes and Electrons. *Phys. Rev.* **87**, 835–842 (1952).

25. Shockley, W. & Queisser, H. J. Detailed Balance Limit of Efficiency of p-n Junction Solar Cells. *Journal of Applied Physics* **32**, 510–519 (1961).

26. Green, M. A. Third generation photovoltaics: Ultra-high conversion efficiency at low cost. *Progress in Photovoltaics: Research and Applications* **9**, 123–135 (2001).

27. Gregg, B. A. & Hanna, M. C. Comparing organic to inorganic photovoltaic cells: Theory, experiment, and simulation. *Journal of Applied Physics* **93**, 3605–3614 (2003).

28. Huynh, W. U., Dittmer, J. J. & Alivisatos, A. P. Hybrid Nanorod-Polymer Solar Cells. *Science* **295**, 2425–2427 (2002).

29. Li, G. *et al.* High-efficiency solution processable polymer photovoltaic cells by self-organization of polymer blends. *Nature Materials* **4**, 864–868 (2005).

30. O'Regan, B. & Grätzel, M. A low-cost, high-efficiency solar cell based on dye-sensitized colloidal TiO2 films. *Nature* **353**, 737–740 (1991).

31. Yella, A. *et al.* Porphyrin-Sensitized Solar Cells with Cobalt (II/III)-Based Redox Electrolyte Exceed 12 Percent Efficiency. *Science* **334**, 629–634 (2011).

32. Grätzel, M. Photoelectrochemical cells. *Nature* **414**, 338–344 (2001).

33. Benkstein, K. D., Kopidakis, N., van de Lagemaat, J. & Frank, A. J. Influence of the Percolation Network Geometry on Electron Transport in Dye-Sensitized Titanium Dioxide Solar Cells. *J. Phys. Chem. B* **107**, 7759–7767 (2003).

34. Law, M., Greene, L. E., Johnson, J. C., Saykally, R. & Yang, P. Nanowire dye-sensitized solar cells. *Nature Materials* **4**, 455–459 (2005).

35. Liu, J. *et al.* Novel dye-sensitized solar cell architecture using TiO2-coated vertically aligned carbon nanofiber arrays. *ACS Appl Mater Interfaces* **1**, 1645–1649 (2009).

36. Li, J. *et al.* Bottom-up approach for carbon nanotube interconnects. *Applied Physics Letters* **82**, 2491–2493 (2003).

37. Zhang, L. *et al.* Four-probe charge transport measurements on individual vertically aligned carbon nanofibers. *Applied Physics Letters* **84**, 3972–3974 (2004).

38. Bryllert, T., Wernersson, L.-E., Froberg, L. E. & Samuelson, L. Vertical high-mobility wrap-gated InAs nanowire transistor. *Electron Device Letters, IEEE* **27**, 323 – 325 (2006).

39. Liu, J., Li, J., Sedhain, A., Lin, J. & Jiang, H. Structure and Photoluminescence Study of TiO2 Nanoneedle Texture along Vertically Aligned Carbon Nanofiber Arrays. *J. Phys. Chem. C* **112**, 17127–17132 (2008).

40. M. Sheinkman & A.Y. Shik*Sov. Phys. Semicon.* **10**, 128 (1976).

41. Hirose, F. *et al.* UV Treatment Effect on TiO_2 Electrodes in Dye-Sensitized Solar Cells with N719 Sensitizer Investigated by Infrared Absorption Spectroscopy. *Electrochemical and Solid-State Letters* **11**, A109 (2008).

42. Göpel, W., Rocker, G. & Feierabend, R. Intrinsic defects of TiO_2 (110): Interaction with chemisorbed O_2, H_2, CO, and CO_2. *Phys. Rev. B* **28**, 3427–3438 (1983).

43. Nelson, J., Eppler, A. M. & Ballard, I. M. Photoconductivity and charge trapping in porous nanocrystalline titanium dioxide. *Journal of Photochemistry and Photobiology A: Chemistry* **148**, 25–31 (2002).

44. Pomoni, K., Vomvas, A. & Trapalis, C. Transient photoconductivity of nanocrystalline TiO2 sol–gel thin films. *Thin Solid Films* **479**, 160–165 (2005).

45. Könenkamp, R., Wahi, A. & Hoyer, P. Photoelectric properties of colloidal semiconductor films. *Thin Solid Films* **246**, 13–16 (1994).

46. Miyata, T., Tsukada, S. & Minami, T. Preparation of anatase TiO_2 thin films by vacuum arc plasma evaporation. *Thin Solid Films* **496**, 136–140 (2006).

47. Appenzeller, J., Radosavljević, M., Knoch, J. & Avouris, P. Tunneling Versus Thermionic Emission in One-Dimensional Semiconductors. *Phys. Rev. Lett.* **92**, 048301 (2004).

48. Zhou, J. *et al*. Gigantic enhancement in response and reset time of ZnO UV nanosensor by utilizing Schottky contact and surface functionalization. *Applied Physics Letters* **94**, 191103–191103–3 (2009).

49. Comedi, D., Heluani, S. P., Villafuerte, M., Arce, R. D. & Koropecki, R. R. Power-law photoconductivity time decay in nanocrystalline TiO_2 thin films. *Journal of Physics: Condensed Matter* **19**, 486205 (2007).

50. Szczepankiewicz, S. H., Colussi, A. J. & Hoffmann, M. R. Infrared Spectra of Photoinduced Species on Hydroxylated Titania Surfaces. *J. Phys. Chem. B* **104**, 9842–9850 (2000).

51. Studenikin, S. A., Golego, N. & Cocivera, M. Carrier mobility and density contributions to photoconductivity transients in polycrystalline ZnO films. *Journal of Applied Physics* **87**, 2413–2421 (2000).

52. Kern, P., Widmer, R., Gasser, P. & Michler, J. Local Tuning of Conductivity in Amorphous Titanium Oxide Films by Selective Electron Beam Irradiation. *J. Phys. Chem. C* **111**, 13972–13980 (2007).

53. Pan, J.-M., Maschhoff, B. L., Diebold, U. & Madey, T. E. Interaction of water, oxygen, and hydrogen with TiO_2 (110) surfaces having different defect densities. *38th National Symposium of the American Vacuum Society* **10**, 2470–2476 (1992).

54. Kim, Y. *et al*. Low-temperature oxygen plasma treatment of TiO_2 film for enhanced performance of dye-sensitized solar cells. *Journal of Power Sources* **175**, 914–919 (2008).

55. Saleh, B. E. A. & Teich, M. C. *Fundamentals of Photonics*. (Wiley-Interscience: 2007).

56. Schneider, H. & Liu, H. C. *Quantum well infrared photodetectors: physics and applications*. (Springer: 2007).

57. Rogalski, A., Antoszewski, J. & Faraone, L. Third-generation infrared photodetector arrays. *Journal of Applied Physics* **105**, 091101–091101–44 (2009).

58. Dereniak, E. L. & Boreman, G. D. *Infrared detectors and systems*. (Wiley: 1996).

59. Richards, P. L. Bolometers for infrared and millimeter waves. *Journal of Applied Physics* **76**, 1–24 (1994).

60. Efros, A. L. & Shklovskii, B. I. Coulomb gap and low temperature conductivity of disordered systems. *Journal of Physics C: Solid State Physics* **8**, L49–L51 (1975).

61. Pedersen, T. G. Variational approach to excitons in carbon nanotubes. *Phys. Rev. B* **67**, 073401 (2003).

62. Fujiwara, A. *et al.* Photoconductivity in Semiconducting Single-Walled Carbon Nanotubes. *Jpn. J. Appl. Phys.* **40**, L1229–L1231 (2001).

63. Xu, J. M. Highly ordered carbon nanotube arrays and IR detection. *Infrared Physics & Technology* **42**, 485–491 (2001).

64. Levitsky, I. A. & Euler, W. B. Photoconductivity of single-wall carbon nanotubes under continuous-wave near-infrared illumination. *Applied Physics Letters* **83**, 1857–1859 (2003).

65. Freitag, M., Martin, Y., Misewich, J. A., Martel, R. & Avouris, P. Photoconductivity of Single Carbon Nanotubes. *Nano Lett.* **3**, 1067–1071 (2003).

66. Itkis, M. E., Borondics, F., Yu, A. & Haddon, R. C. Bolometric Infrared Photoresponse of Suspended Single-Walled Carbon Nanotube Films. *Science* **312**, 413–416 (2006).

67. Pradhan, B., Setyowati, K., Liu, H., Waldeck, D. H. & Chen, J. Carbon nanotube-polymer nanocomposite infrared sensor. *Nano Lett.* **8**, 1142–1146 (2008).

68. Aliev, A. E. Bolometric detector on the basis of single-wall carbon nanotube/polymer composite. *Infrared Physics & Technology* **51**, 541–545 (2008).

69. Zhang, J. *et al.* Photovoltaic effect in single carbon nanotube-based Schottky diodes. *International Journal of Nanoparticles* **1**, 108 – 118 (2008).

70. Zhang, J. *et al.* Design, Manufacturing, and Testing of Single-Carbon-Nanotube-Based Infrared Sensors. *Nanotechnology, IEEE Transactions on* **8**, 245 –251 (2009).

71. Chen, H., Xi, N., Lai, K. W. C., Fung, C. K. M. & Yang, R. Development of Infrared Detectors Using Single Carbon-Nanotube-Based Field-Effect Transistors. *Nanotechnology, IEEE Transactions on* **9**, 582 –589 (2010).

72. Lu, R., Li, Z., Xu, G. & Wu, J. Z. Suspending single-wall carbon nanotube thin film infrared bolometers on microchannels. *Applied Physics Letters* **94**, 163110–163110–3 (2009).

73. Lu, R., Shi, J. J., Baca, F. J. & Wu, J. Z. High performance multiwall carbon nanotube bolometers. *Journal of Applied Physics* **108**, 084305 –084305–5 (2010).

74. Chen, C., Yi, X., Zhao, X. & Xiong, B. Characterizations of VO2-based uncooled microbolometer linear array. *Sensors and Actuators A: Physical* **90**, 212–214 (2001).

75. Han, Y.-H., Kim, K.-T., Shin, H.-J., Moon, S. & Choi, I.-H. Enhanced characteristics of an uncooled microbolometer using vanadium–tungsten oxide as a thermometric material. *Applied Physics Letters* **86**, 254101–254101–3 (2005).

76. Lu, R., Xu, G. & Wu, J. Z. Effects of thermal annealing on noise property and temperature coefficient of resistance of single-walled carbon nanotube films. *Applied Physics Letters* **93**, 213101–213101–3 (2008).

77. Lu, R., Kamal, R. & Wu, J. Z. A comparative study of 1/f noise and temperature coefficient of resistance in multiwall and single-wall carbon nanotube bolometers. *Nanotechnology* **22**, 265503 (2011).

78. Bourlon, B., Miko, C., Forró, L., Glattli, D. C. & Bachtold, A. Determination of the Intershell Conductance in Multiwalled Carbon Nanotubes. *Phys. Rev. Lett.* **93**, 176806 (2004).

79. Fujii, M. *et al.* Measuring the Thermal Conductivity of a Single Carbon Nanotube. *Phys. Rev. Lett.* **95**, 065502 (2005).

80. Capaz, R. B., Spataru, C. D., Ismail-Beigi, S. & Louie, S. G. Diameter and chirality dependence of exciton properties in carbon nanotubes. *Phys. Rev. B* **74**, 121401 (2006).

81. Kasumov, A. Y. *et al.* Conductivity and atomic structure of isolated multiwalled carbon nanotubes. *Europhysics Letters (EPL)* **43**, 89–94 (1998).

82. Itkis, M. E. *et al.* Spectroscopic Study of the Fermi Level Electronic Structure of Single-Walled Carbon Nanotubes. *Nano Lett.* **2**, 155–159 (2001).

83. Ouacha, H. *et al.* Noise properties of an individual and two crossing multiwalled carbon nanotubes. *Applied Physics Letters* **80**, 1055–1057 (2002).

84. Kim, K. *et al.* Influence of electrical contacts on the 1/f noise in individual multi-walled carbon nanotubes. *Nanotechnology* **21**, 335702 (2010).

85. Tarasov, M., Svensson, J., Kuzmin, L. & Campbell, E. E. B. Carbon nanotube bolometers. *Applied Physics Letters* **90**, 163503–163503–3 (2007).

86. Wallace, P. R. The Band Theory of Graphite. *Phys. Rev.* **71**, 622–634 (1947).

87. Slonczewski, J. C. & Weiss, P. R. Band Structure of Graphite. *Phys. Rev.* **109**, 272–279 (1958).

88. H. P. Boehm, A. Clauss, G. O. Fischer & U. Z. Hofmann *Anorg. Allg. Chem.* **316**, 119–127 (1962).

89. Van Bommel, A. J., Crombeen, J. E. & Van Tooren, A. LEED and Auger electron observations of the SiC(0001) surface. *Surface Science* **48**, 463–472 (1975).

90. Eizenberg, M. & Blakely, J. M. Carbon monolayer phase condensation on Ni(111). *Surface Science* **82**, 228–236 (1979).

91. Abergel, D. S. L., Apalkov, V., Berashevich, J., Ziegler, K. & Chakraborty, T. Properties of graphene: a theoretical perspective. *Advances in Physics* **59**, 261–482 (2010).

92. R.E. Peierls *Ann. I. H. Poincare* **5**, 177–222 (1935).

93. L. D.Landau *Phys. Z. Sowjetunion* **11**, 26–35 (1937).

94. Meyer, J. C. *et al.* The structure of suspended graphene sheets. *Nature* **446**, 60–63 (2007).

95. Novoselov, K. S. *et al.* Two-Dimensional Atomic Crystals. *PNAS* **102**, 10451–10453 (2005).

96. Novoselov, K. S. *et al.* Two-dimensional gas of massless Dirac fermions in graphene. *Nature* **438**, 197–200 (2005).

97. Du, X., Skachko, I., Barker, A. & Andrei, E. Y. Approaching ballistic transport in suspended graphene. *Nature Nanotechnology* **3**, 491–495 (2008).

98. Novoselov, K. S. *et al.* Room-Temperature Quantum Hall Effect in Graphene. *Science* **315**, 1379–1379 (2007).

99. Du, X., Skachko, I., Duerr, F., Luican, A. & Andrei, E. Y. Fractional quantum Hall effect and insulating phase of Dirac electrons in graphene. *Nature* **462**, 192–195 (2009).

100. Katsnelson, M. I., Novoselov, K. S. & Geim, A. K. Chiral tunnelling and the Klein paradox in graphene. *Nature Physics* **2**, 620–625 (2006).

101. Pisana, S. *et al.* Breakdown of the adiabatic Born-Oppenheimer approximation in graphene. *Nature Materials* **6**, 198–201 (2007).

102. Nair, R. R. *et al.* Fine Structure Constant Defines Visual Transparency of Graphene. *Science* **320**, 1308–1308 (2008).

103. Wu, J. *et al.* Organic Light-Emitting Diodes on Solution-Processed Graphene Transparent Electrodes. *ACS Nano* **4**, 43–48 (2009).

104. Gilje, S., Han, S., Wang, M., Wang, K. L. & Kaner, R. B. A Chemical Route to Graphene for Device Applications. *Nano Lett.* **7**, 3394–3398 (2007).

105. Mattevi, C. *et al.* Evolution of Electrical, Chemical, and Structural Properties of Transparent and Conducting Chemically Derived Graphene Thin Films. *Advanced Functional Materials* **19**, 2577–2583 (2009).

106. Blake, P. *et al.* Graphene-Based Liquid Crystal Device. *Nano Lett.* **8**, 1704–1708 (2008).

107. Hass, J. *et al.* Highly ordered graphene for two dimensional electronics. *Applied Physics Letters* **89**, 143106–143106–3 (2006).

108. Emtsev, K. V. *et al.* Towards wafer-size graphene layers by atmospheric pressure graphitization of silicon carbide. *Nature Materials* **8**, 203–207 (2009).

109. Reina, A. *et al.* Large Area, Few-Layer Graphene Films on Arbitrary Substrates by Chemical Vapor Deposition. *Nano Lett.* **9**, 30–35 (2008).

110. Kim, K. S. *et al.* Large-scale pattern growth of graphene films for stretchable transparent electrodes. *Nature* **457**, 706–710 (2009).

111. Li, X. *et al.* Large-Area Synthesis of High-Quality and Uniform Graphene Films on Copper Foils. *Science* **324**, 1312–1314 (2009).

112. Bae, S. *et al.* Roll-to-roll production of 30-inch graphene films for transparent electrodes. *Nature Nanotechnology* **5**, 574–578 (2010).

113. Ago, H. *et al.* Epitaxial Chemical Vapor Deposition Growth of Single-Layer Graphene over Cobalt Film Crystallized on Sapphire. *ACS Nano* **4**, 7407–7414 (2010).

114. Coraux, J., N`Diaye, A. T., Busse, C. & Michely, T. Structural Coherency of Graphene on Ir(111). *Nano Lett.* **8**, 565–570 (2008).

115. Li, X. *et al.* Transfer of Large-Area Graphene Films for High-Performance Transparent Conductive Electrodes. *Nano Lett.* **9**, 4359–4363 (2009).

116. Li, X. *et al.* Large-Area Graphene Single Crystals Grown by Low-Pressure Chemical Vapor Deposition of Methane on Copper. *J. Am. Chem. Soc.* **133**, 2816–2819 (2011).

117. Li, X., Cai, W., Colombo, L. & Ruoff, R. S. Evolution of Graphene Growth on Ni and Cu by Carbon Isotope Labeling. *Nano Lett.* **9**, 4268–4272 (2009).

118. Mattevi, C., Kim, H. & Chhowalla, M. A review of chemical vapour deposition of graphene on copper. *J. Mater. Chem.* **21**, 3324–3334 (2011).

119. Bao, W. *et al.* Controlled ripple texturing of suspended graphene and ultrathin graphite membranes. *Nature Nanotechnology* **4**, 562–566 (2009).

120. Ogawa, Y. *et al.* Domain Structure and Boundary in Single-Layer Graphene Grown on Cu(111) and Cu(100) Films. *J. Phys. Chem. Lett.* **3**, 219–226 (2011).

121. Jauregui, L. A., Cao, H., Wu, W., Yu, Q. & Chen, Y. P. Electronic properties of grains and grain boundaries in graphene grown by chemical vapor deposition. *Solid State Communications* **151**, 1100–1104 (2011).

122. Yu, Q. *et al.* Control and characterization of individual grains and grain boundaries in graphene grown by chemical vapour deposition. *Nature Materials* **10**, 443–449 (2011).

123. Liu, J. *et al.* Doped graphene nanohole arrays for flexible transparent conductors. *Applied Physics Letters* **99**, 023111–023111–3 (2011).

124. Ferrari, A. C. & Robertson, J. Interpretation of Raman spectra of disordered and amorphous carbon. *Phys. Rev. B* **61**, 14095–14107 (2000).

125. Ferrari, A. C. *et al.* Raman Spectrum of Graphene and Graphene Layers. *Phys. Rev. Lett.* **97**, 187401 (2006).

126. Wei, D. *et al.* Synthesis of N-Doped Graphene by Chemical Vapor Deposition and Its Electrical Properties. *Nano Lett.* **9**, 1752–1758 (2009).

127. Ni, Z. H. *et al.* Probing Charged Impurities in Suspended Graphene Using Raman Spectroscopy. *ACS Nano* **3**, 569–574 (2009).

128. Wang, Y. Y., Ni, Z. H., Shen, Z. X., Wang, H. M. & Wu, Y. H. Interference enhancement of Raman signal of graphene. *Applied Physics Letters* **92**, 043121–043121–3 (2008).

129. Das, A. *et al.* Monitoring dopants by Raman scattering in an electrochemically top-gated graphene transistor. *Nature Nanotechnology* **3**, 210–215 (2008).

130. Yan, J., Zhang, Y., Kim, P. & Pinczuk, A. Electric Field Effect Tuning of Electron-Phonon Coupling in Graphene. *Phys. Rev. Lett.* **98**, 166802 (2007).

131. Song, H. S. *et al.* Origin of the relatively low transport mobility of graphene grown through chemical vapor deposition. *Scientific Reports* **2**, (2012).

132. Pimenta, M. A. *et al.* Studying disorder in graphite-based systems by Raman spectroscopy. *Phys. Chem. Chem. Phys.* **9**, 1276–1290 (2007).

133. Guermoune, A. *et al.* Chemical vapor deposition synthesis of graphene on copper with methanol, ethanol, and propanol precursors. *Carbon* **49**, 4204–4210 (2011).

134. Podila, R. *et al.* Effects of disorder on the optical properties of CVD grown polycrystalline graphene. *Nanoscale* **4**, 1770 (2012).

135. Newson, R. W., Dean, J., Schmidt, B. & van Driel, H. M. Ultrafast carrier kinetics in exfoliated graphene and thin graphite films. *Opt. Express* **17**, 2326–2333 (2009).

136. Ruzicka, B. A. *et al.* Hot carrier diffusion in graphene. *Phys. Rev. B* **82**, 195414 (2010).

137. Dawlaty, J. M., Shivaraman, S., Chandrashekhar, M., Rana, F. & Spencer, M. G. Measurement of ultrafast carrier dynamics in epitaxial graphene. *Applied Physics Letters* **92**, 042116–042116–3 (2008).

138. George, P. A. *et al.* Ultrafast Optical-Pump Terahertz-Probe Spectroscopy of the Carrier Relaxation and Recombination Dynamics in Epitaxial Graphene. *Nano Lett.* **8**, 4248–4251 (2008).

139. Ruzicka, B. A. *et al.* Spatially resolved pump-probe study of single-layer graphene produced by chemical vapor deposition [Invited]. *Opt. Mater. Express* **2**, 708–716 (2012).

140. R. Holm & W. Meissner Kontaktwiderstand Zwischen Supraleitern und Nichtsupraleitern. *Z. Physik* **74**, 715 (1932).

141. JOSEPHSON, B. D. Coupled Superconductors. *Rev. Mod. Phys.* **36**, 216–220 (1964).

142. Sui, Y. & Appenzeller, J. Screening and Interlayer Coupling in Multilayer Graphene Field-Effect Transistors. *Nano Lett.* **9**, 2973–2977 (2009).

143. Schedin, F. *et al.* Detection of individual gas molecules adsorbed on graphene. *Nature Materials* **6**, 652–655 (2007).

144. Wang, X. *et al.* N-Doping of Graphene Through Electrothermal Reactions with Ammonia. *Science* **324**, 768–771 (2009).

145. Ishigami, M., Chen, J. H., Cullen, W. G., Fuhrer, M. S. & Williams, E. D. Atomic Structure of Graphene on SiO2. *Nano Lett.* **7**, 1643–1648 (2007).

146. Adam, S., Hwang, E. H., Galitski, V. M. & Das Sarma, S. A Self-Consistent Theory for Graphene Transport. *PNAS* **104**, 18392–18397 (2007).

147. Chen, J.-H. *et al.* Charged-impurity scattering in graphene. *Nature Physics* **4**, 377–381 (2008).

148. Ando, T., Fowler, A. B. & Stern, F. Electronic properties of two-dimensional systems. *Rev. Mod. Phys.* **54**, 437–672 (1982).

149. Fratini, S. & Guinea, F. Substrate-limited electron dynamics in graphene. *Phys. Rev. B* **77**, 195415 (2008).

150. Bolotin, K. I. *et al.* Ultrahigh electron mobility in suspended graphene. *Solid State Communications* **146**, 351–355 (2008).

151. Yoshioka, D. *The Quantum Hall Effect*. (Springer: 2002).

152. Palacios, J. J. Origin of the quasiuniversality of the minimal conductivity of graphene. *Phys. Rev. B* **82**, 165439 (2010).

153. Partoens, B. & Peeters, F. M. From graphene to graphite: Electronic structure around the K point. *Phys. Rev. B* **74**, 075404 (2006).

154. Morozov, S. V. *et al.* Two-dimensional electron and hole gases at the surface of graphite. *Phys. Rev. B* **72**, 201401 (2005).

155. Likharev, K. K. Superconducting weak links. *Rev. Mod. Phys.* **51**, 101–159 (1979).

156. Tinkham, M. *Introduction to Superconductivity*. (Courier Dover Publications: 2004).

157. Titov, M. & Beenakker, C. W. J. Josephson effect in ballistic graphene. *Phys. Rev. B* **74**, 041401 (2006).

158. Beenakker, C. W. J. Specular Andreev Reflection in Graphene. *Phys. Rev. Lett.* **97**, 067007 (2006).

159. Heersche, H. B., Jarillo-Herrero, P., Oostinga, J. B., Vandersypen, L. M. K. & Morpurgo, A. F. Bipolar supercurrent in graphene. *Nature* **446**, 56–59 (2007).

160. Octavio, M., Tinkham, M., Blonder, G. E. & Klapwijk, T. M. Subharmonic energy-gap structure in superconducting constrictions. *Phys. Rev. B* **27**, 6739–6746 (1983).

161. Trbovic, J., Minder, N., Freitag, F. & Schönenberger, C. Superconductivity enhanced conductance fluctuations in few layer graphene nanoribbons. *arXiv:0912.0389* (2009).

162. Kanda, A. *et al.* Dependence of proximity-induced supercurrent on junction length in multilayer-graphene Josephson junctions. *Physica C: Superconductivity* **470**, 1477–1480 (2010).

163. Du, X., Skachko, I. & Andrei, E. Y. Josephson current and multiple Andreev reflections in graphene SNS junctions. *Phys. Rev. B* **77**, 184507 (2008).

164. Jeong, D. *et al.* Observation of supercurrent in PbIn-graphene-PbIn Josephson junction. *Phys. Rev. B* **83**, 094503 (2011).

165. Lee, G.-H., Jeong, D., Choi, J.-H., Doh, Y.-J. & Lee, H.-J. Electrically Tunable Macroscopic Quantum Tunneling in a Graphene-Based Josephson Junction. *Phys. Rev. Lett.* **107**, 146605 (2011).

166. Shailos, A. *et al.* Proximity effect and multiple Andreev reflections in few-layer graphene. *Europhysics Letters (EPL)* **79**, 57008 (2007).

167. Ojeda-Aristizabal, C., Ferrier, M., Guéron, S. & Bouchiat, H. Tuning the proximity effect in a superconductor-graphene-superconductor junction. *Phys. Rev. B* **79**, 165436 (2009).

168. Popinciuc, M. *et al.* Zero-bias conductance peak and Josephson effect in graphene-NbTiN junctions. *arXiv:1202.4774* (2012).

169. Rickhaus, P., Weiss, M., Marot, L. & Schönenberger, C. Quantum Hall Effect in Graphene with Superconducting Electrodes. *Nano Lett.* **12**, 1942–1945 (2012).

170. Komatsu, K., Li, C., Autier-Laurent, S., Bouchiat, H. & Gueron, S. Superconducting proximity effect through graphene from zero field to the Quantum Hall regime. *arXiv:1202.1690* (2012).

171. Monteverde, M. *et al.* What Are the Relevant Disorder Scales for Quantum Transport in Graphene *Journal of Low Temperature Physics* **167**, 1–14 (2012).

172. Kessler, B. M., Girit, Ç. Ö., Zettl, A. & Bouchiat, V. Tunable Superconducting Phase Transition in Metal-Decorated Graphene Sheets. *Phys. Rev. Lett.* **104**, 047001 (2010).

173. Dubos, P., Courtois, H., Buisson, O. & Pannetier, B. Coherent Low-Energy Charge Transport in a Diffusive S-N-S Junction. *Phys. Rev. Lett.* **87**, 206801 (2001).

174. Hammer, J. C., Cuevas, J. C., Bergeret, F. S. & Belzig, W. Density of states and supercurrent in diffusive SNS junctions: Roles of nonideal interfaces and spin-flip scattering. *Phys. Rev. B* **76**, 064514 (2007).

175. Martin, J. *et al.* Observation of electron|[ndash]|hole puddles in graphene using a scanning single-electron transistor. *Nature Physics* **4**, 144–148 (2007).

176. Blake, P. *et al.* Making graphene visible. *Applied Physics Letters* **91**, 063124–063124–3 (2007).

177. Xia, F., Perebeinos, V., Lin, Y., Wu, Y. & Avouris, P. The origins and limits of metal-graphene junction resistance. *Nature Nanotechnology* **6**, 179–184 (2011).

178. Robinson, J. A. *et al.* Contacting graphene. *Applied Physics Letters* **98**, 053103–053103–3 (2011).

179. Bolotin, K. I., Sikes, K. J., Hone, J., Stormer, H. L. & Kim, P. Temperature-Dependent Transport in Suspended Graphene. *Phys. Rev. Lett.* **101**, 096802 (2008).